TOWARDS RATIONAL DESIGN OF SOLID OXIDE FUEL CELL ELECTRODES THROUGH SURFACE MODIFICATION

A Dissertation
Presented to
The Academic Faculty

by

Brian Thomas Doyle

In Partial Fulfillment
of the Requirements for the Degree
Doctor of Philosophy in the
School of Materials Science and Engineering

Georgia Institute of Technology
December 2017

TOWARDS RATIONAL DESIGN OF SOLID OXIDE FUEL CELL ELECTRODES THROUGH SURFACE MODIFICATION

Approved by:

Dr. Meilin Liu, Advisor
School of Materials Science and Engineering
Georgia Institute of Technology

Dr. Mark Losego
School of Materials Science and Engineering
Georgia Institute of Technology

Dr. Faisal Alamgir
School of Materials Science and Engineering
Georgia Institute of Technology

Dr. Lawrence Bottomley
School of Chemistry and Biochemistry
Georgia Institute of Technology

Dr. Matthew McDowell
School of Materials Science and Engineering
School of Mechanical Engineering
Georgia Institute of Technology

Date Approved: November 10, 2017

Life is like riding a bicycle. To keep your balance you must keep moving.

- *Albert Einstein*

ACKNOWLEDGEMENTS

I would like to first thank my advisor, Dr Meilin Liu, who gave me the opportunity to explore solid-state electrochemistry in solid oxide fuel cell research. You provided the resources and expertise to let me explore many different areas, which helped me develop as a scientist. You also gave me the encouragement to pursue opportunities outside of research that has prepared me for life after graduate school.

I would also like to thank the individuals throughout Georgia Tech who have been a part of my graduate school experience. Thanks to David Tavakoli, Walter Henderson, Yolande Berta and Eric Woods for training and support for the characterization equipment in the Institute for Electronics and Nanotechnology. Also, thank you to Dr Yong Ding for the TEM work in this dissertation. gtIn the School of Materials Science, I must thank Susan Bowman for her ability to make me feel at home from day one at Georgia Tech. I would also like to thank Teresa, La Juana, James, Sarah, Mechelle, Frank and Roosevelt for all the help on various things to do with the school and the Liu group over that last five years.

Without a doubt, I have had the opportunity to work with some great individuals. I didn't realize how lucky I was to have colleagues with such expertise in a wide array of fields. Dr Dong Ding and Dr Mingfei Liu were great examples of scientists as I began my graduate career. Dr Bote Zhao, Dr Yu Chen and Dr Seoungyoung Yoo have been a great help not only as research colleagues but also as friends and supporters. You have given me friendship and conversations about cultures different than my own.

To my fellow graduate students in the Liu group, thank you for the comradery that made my time in lab enjoyable. Dr Dongchang Chen, for showing me unbelievable work ethic and an easy smile. Dr Ben Rainwater and Dr Gordon Waller for endless discussions about life and research and for setting an example of what it takes to get a PhD. Dr Philip Brooke and Ben Deglee for making my time in Atlanta much more interesting both in and out of lab. To Nikolay and Ryan for what seems like endless engineering of things around lab and discussions about everything from gas piping to barbecuing.

To my fellow classmates who came in as optimistic graduate students in the fall of 2012: Graham, Judy, Alex, Stefany and Dan. I was lucky enough to find a group of people who have shaped my entire graduate school experience in ways I could not have imagined. Whether talking politics or science or breweries or the mean meaning of life, I would not have had the same experience without you. You were there for the ups and downs of graduate school and all aspects of life.

As I reflect back on my time in graduate school, I can't help but to think of all the opportunities Georgia Tech has provided me, all of which has shaped me into the person I am today. I was able to delve into the world of energy through the Energy Club and the ARPA-E Summit Student Program and met so many people passionate about the future of our society. I've been able to host workshops and professional development through my time with the Graduate Student Advisory Group for MSE and the Graduate Student Government Association. I've worked with others on management consulting case competitions and learned about fixed income investing through the GT Student Investments Committee. I have had the opportunity to communicate science through the Energy Frontier Research Center newsletter and advocate for materials science to Georgia

Congressmen. I've explored different career opportunities through the Sam Nunn Security Fellows Program and have been exposed to the international world of energy research through the Joint US-Africa Materials Institute in Tanzania.

I couldn't finish acknowledgements without recognizing the triathlon team at Georgia Tech I've been a part of over the years. The growth and cohesiveness of the team has been tremendous and has given me the chance to meet some unbelieve undergraduate and graduate students at Georgia Tech. Thank you for training camps and being both a competitive and social outlet during graduate school.

To my friends I have known for years who continued to stay in touch: Anthony, Tyler, Shawn and Ian. Even as I moved away, you were never further than a phone call or text away. I value your friendship and belief in me after all these years.

To my family, thank you for your constant support from near and far. My parents have given me every opportunity to succeed and provided an example of how to work hard and succeed in life. I would not be the person I am today without your guidance, support and wisdom. To my sister, Jen, who has allowed me to be the annoying little brother for nearly three decades, even from 2,000 miles away. My time in Atlanta would not have been the same without phone calls and endless laughs you have brought. And to Kelly, who somehow stumbled upon me in a dark room and found some way to be around me as I finished by dissertation. Thank you for your positivity and endless quest to be as obnoxious as I am.

I look forward to the next chapter of life and could not have done it without the support of so many people around me. Thank you.

TABLE OF CONTENTS

ACKNOWLEDGEMENTS **iv**

LIST OF TABLES **ix**

LIST OF FIGURES **x**

LIST OF SYMBOLS AND ABBREVIATIONS **xviii**

SUMMARY **xix**

CHAPTER 1. Introduction **1**
1.1 Motivation **1**
1.2 Research Objectives **5**
1.3 Dissertation Structure **5**

CHAPTER 2. Background **7**
2.1 Solid Oxide Fuel Cells **7**
2.2 Thermodynamics **8**
2.2.1 Thermodynamic Foundation and Nernst Equation 8
2.2.2 Equilibrium Defect Reactions 13
2.3 Kinetics **15**
2.4 Increasing Cathode Performance **19**
2.4.1 Ionically Conductive Infiltrates 25
2.4.2 Electrically Conductive Infiltrates 29
2.4.3 Applications of Conformal Coatings 33
2.5 Technical Approaches **36**
2.5.1 Electrochemical Impedance Spectroscopy 36
2.5.2 X-ray Photoelectron Spectroscopy (XPS) 39

CHAPTER 3. Asymmetric Cell testing Platform **42**
3.1 Electrolyte Supported Cell Fabrication **42**
3.2 RF Sputtering **47**
3.3 Morphology Upon Deposition and Post-Testing **54**
3.4 Electrochemical Characterization **58**

CHAPTER 4. Ceria Coatings on LSCF Cathodes **67**
4.1 Overview of Chapter **67**
4.2 Fabrication **67**
4.3 Infiltration of Undoped Ceria Coatings on LSCF **70**
4.4 Thin Films of Undoped Ceria **73**
4.4.1 Sputtering Deposition 73
4.4.2 Conformal Thin Film 74
4.5 Infiltration of Samarium Doped Ceria **85**
4.6 Conformal Thin Films **89**
4.7 Discussion **92**

CHAPTER 5. Surface Modification with Praseodymium Doped Ceria 102
5.1 Fabrication 103
5.2 X-ray Diffraction of Ceria and Doped Ceria 108
5.3 Varying Molarity 110
5.4 Infiltrated PDC 112
5.5 Ionic/Electronic Conductivity of PDC 114
5.6 XPS of Prasedoymium doped Ceria 116
5.6.1 Ceria 116
5.6.2 Praseodymium 122
5.6.3 Valence band 127
5.7 TGA of PDC 131
5.8 Discussion 137

CHAPTER 6. Conclusions and recommendations for Future Work 141
6.1 Summary and Conclusions 141
6.2 Recommendations for Future Work 142

APPENDIX A. Transition Metal Carbides for SOFC ANodes 145
6.3 Patterned Anode 149
6.4 Carburization of Mo_2C 153
6.5 Raman 160

REFERENCES 161

LIST OF TABLES

Table 1.	Table 1. Firing Conditions for SDC Electrolyte	43
Table 2.	Polishing protocol for electrolyte supports used in the pattern anode full cells.	44
Table 3.	Protocol for making the tape cast slurry for the LSCF cathodes.	45
Table 4.	Peaks associated with the cerium 3d spectra characterized through X-ray photoelectron spectroscopy.	119
Table 5	Peaks associated with Pr 3d spectra	125
Table 6	Comparison of oxygen loss normalized per mol of praseodymium for 30, 50 and 70 PDC.	136

LIST OF FIGURES

Figure 1. Projections of a) world energy consumption[1] and b) U.S. energy production through 2040[2]. 2

Figure 2. A summary of trade-offs related to operating temperature of solid oxide fuel cells[11]..... 4

Figure 3. Schematic showing the electrolytes that define the different fuel cell technologies[13]..... 8

Figure 4. A Brouwer diagram for acceptor-doped ceria[16]. 15

Figure 5. a) A typical IV curve showing the fuel cell polarization losses and b) the relative contributions for the anode, cathode and electrolyte[14]..... 17

Figure 6. Two models where a) shows the impedance spectra if the ORR overall reaction is limited by surface adsorption and b) the ORR reaction is limited by diffusion of the oxygen anion through the mixed conducting film[17]..... 24

Figure 7. The a) impedance spectra and b) the plot of interfacial resistance versus inverse temperature[26]..... 26

Figure 8. a) Comparison of conductivity between SDC and LCC and b) a comparison of interfacial resistance between LSCF, a physical mixture of LSCF-LCC and a physical mixture of LSCF-SDC [35] 28

Figure 9. The a) volcano relationship between reducibility and the surface exchange coefficient and b) the increase in surface strontium for varying infiltrated cations[36]..... 29

Figure 10. Above, (a) shows a cross section of a 48nm coating of LSM on a dense LSCF asymmetric cell; (b) a TEM micrograph of a porous LSCF cathode with a conformal coating of LSM; and (c) current density over time measurements for the blank and LSM-coated cathode [39] 31

Figure 11. Examples of an impedances spectra and the accompanying RC circuit model.[60] 36

Figure 12. a) shows the small voltage perturbation and the resulting gain and phase shift, b) an example of an Nyquist plot with imaginary and real impedance as the y and x-axis respectively, and c) the corresponding Bode plot of impedance as a function of frequency [60]. 37

Figure 13. Several representative graphs for deriving Gerischer impedance response where a) shows a semi-infinite plane with a given equilibrium surface coverage, b) is the concentration profile about the origin, c) is the surface fulx as a function of time with the utilization length parameter, and d) the impedance spectra for surface flux species [61] 39

Figure 14. A schematic representing the major features of an XPS chamber including, photon source, hemispherical analyzer and an inset of example XPS spectra[63]... 41

Figure 15. A cross section showing the dense electrolyte support and the porous LSCF cathode. 47

Figure 16 The sputtering system used in this dissertation showing the stainless-steel chamber, the interior of the chamber with heating stage installed, and the argon gas inlets on the top. 49

Figure 17. Cracking of LSCF targets during RF sputtering..... 52

Figure 18. Two target holding set ups where a) the clamping ring pressed against the copper backing plate and b) the clamping ring pressed against the lip of a copper target holder. The copper holder with the small lip was the optimal set up to avoid cracking of the LSCF target. 53
Figure 19. The as-deposited LSCF film shown as a) cross section, b) top-down view before testing. Compare those images to the PLD films by Simrick with c) top-down view as-deposited and d) a top-down view after EIS testing[66]. 56
Figure 20. A top-down SEM image taken of the LSCF film after a) annealing to 800°C for two hours and b) zoomed in further after cell testing. 57
Figure 21. The top and bottom view of the asymmetric cathode with a) silver paste and silver connecting wires and with b) silver mesh on the polished LSCF with silver paste on the porous LSCF electrode. 58
Figure 22. Compression testing setup for asymmetric and symmetric cells..... 59
Figure 23. Comparison of the impedance spectra for the LSCF dense film and a symmetric cell with two porous LSCF cathodes at 750°C. The inset graph is an enlarged view of the impedance of the symmetric cell, which is hardly visible on the scale of the dense film impedance. 60
Figure 24. EIS spectra taken on two samples fabricated under the same conditions with the only change being the type of current collector used..... 61
Figure 25. Impedance spectra collected at varying oxygen partial pressures showing the defining characteristic of the spectra is due to the oxygen reduction reaction activity. 62

Figure 26. Polarization resistance values for LSCF film ranging in thickness from 321-750 nm. 65
Figure 27. The effect of chelating agents on the polarization resistance of undoped ceria infiltrated on an LSCF backbone. The error bars indicated one standard deviation. 69
Figure 28. SEM micrograph of the undoped ceria infiltration on the LSCF cathode backbone. The coatings are faint because of the small amount of material deposited and the excellent surface coverage. 69
Figure 29. Polarization resistance for infiltrated undoped ceria of varying molarities. ... 71
Figure 30. SEM images of a) 0.03M UDC, b) 0.10M UDC, c) 0.5M UDC and d) 1.0M UDC. Note the morpohology changes from 0.5M to 1.0M. Each row is the same sample at two different regions. Note the scale bars are either 500 nm or 1000 nm. 72
Figure 31. SEM of the cross-section of the ceria film deposited on a silicon wafer. The film thickness is approximately 340 nm. 75
Figure 32. TEM cross-section of the asymmetric cell a) showing the dense SDC support, the LSCF cathode and the ceria coating, b) zooming in on the LSCF and the ceria coating on top, c) showing contrast between the ceria and LSCF, d) zooming in on the columnar structure of the ceria film and e) diffraction pattern of the ceria coated LSCF. 76
Figure 33. The variation in electrochemical impedance as a function of ceria film thickness. 77
Figure 34. Plot of polarization resistance as a function of ceria film thickness. 78
Figure 35. Impedance response of reference LSCF film a) under varying bias and b) under OCV after biased test. 81

Figure 36. Impedance of asymmetric cell with 80 nm ceria coating a) under varying bias and b) the relaxation behavior after the biased measurement. 82
Figure 37. Impedance of asymmetric cell with 160 nm ceria coating a) under varying bias and b) the relaxation behavior after the biased measurement. 84
Figure 38. Impedance of asymmetric cell with 320 nm ceria coating a) under varying bias and b) the relaxation behavior after the biased measurement. 85
Figure 39. Polarization resistance changes as a function of the molarity of 10SDC. The lowest polarization resistance is found with 0.3M solution. 87
Figure 40. Polarization resistance changes as a function of molarity of 20SDC. 87
Figure 41. Polarization resistance of 30SDC infiltrated into LSCF symmetric cell. 89
Figure 42. Nyquist plot showing the relationship between impedance and thickness of 20SDC film. 90
Figure 43. Nyquist plot of a) the 80 nm SDC-coated LSCF and b) the 160 nm SDC-coated LSCF under varying bias 92
Figure 44. Schematic showing a possible mechanism for enhancement of the doped ceria surface modification on an LSCF backbone 94
Figure 45. Comparison of the change in polarization resistance as a function of cathodic bias 96
Figure 46. The change in oxidation state of a) a 50 nm ceria film under different applied biases and b) the relative % Ce3+ change under bias for varying film thicknesses. Figure taken from [78]. 98
Figure 47. The enthalpy of formation for an oxygen vacancy in undoped ceria and 20GDC [79] 100

Figure 48. Images of a) 30PDC fired to 1500°C for 5 hours taken in SEM and b) praseodymium oxide fired under reducing conditions to 1400°C. 106
Figure 49. The a) conductivity as a function of doping concentration and temperature and b) the ionic transference number as a function of dopant concentration and temperature[82]. 107
Figure 50. XRD patterns of praseodymium doped ceria a) over the whole 2θ range and b) zoomed in on the first two major peaks. 109
Figure 51. SEM images of a) LSCF backbone without infiltration b) backbone with 0.1M praseodymium nitrate c) backbone with 1.0 M praseodymium nitrate and d) backbone with 2.0M praseodymium nitrate..... 111
Figure 52. The variation in polarization resistance for varying concentrations of praseodymium nitrate infiltrated solutions. The error bars represent one standard deviation..... 112
Figure 53. The variation in polarization resistance as a function of praseodymium doping concentration from 550 to 750°C..... 113
Figure 54. Polarization resistance as a function of ionic conductivity for 30, 50 and 70 PDC. Each composition has several points which indicate different operating temperatures. 115
Figure 55. Polarization resistance as a function of electronic conductivity for 30, 50 and 70 PDC. Each composition has several points which indicate different operating temperatures. 115
Figure 56. Reference XPS spectra for Ce 4+ and Ce 3+ taken from data files in the Thermo Avantage XPS software used to acquire the data..... 120

Figure 57. The Ce 3d XPS spectra for praseodymium doped ceria at varying dopant levels taken from the infiltrated samples. 121

Figure 58. The fitted XPS Ce 3d spectra for 50 mol% praseodymium-doped ceria. Note the spectra is nearly 100% Ce^{4+}. 122

Figure 59. Two reference Pr 3d XPS spectra taken from literature that identify the relevant praseodymium peaks. Note that the x-axis is binding energy, but one is descending and the other ascending. Also note the naming convention is not the same between the two [98], [99]. 124

Figure 60. Fitting the Pr 3d spectra for the 10PDC composition. 126

Figure 61. The variation in the Pr 3+/4+ ratio as a function of praseodymium content in the ceria host. 126

Figure 62. The valence band spectra for praseodymium doped ceria 127

Figure 63. The valence band a) peaks and b) binding energy as a function of mol % praseodymium 130

Figure 64. The a) nonstoichiometry of praseodymium-doped ceria powders as a function of temperature measured in air by TGA and b) the same plot showing the praseodymium oxide baseline used in the calculations. The dotted box shows the temperature range of the electrochemical testing (550-750°C). 134

Figure 65. Excess enthalpy as a function of nonstiochiometry in the 20PDC system [102] 139

Figure 66. The calculated oxygen reduction energy based on nearest neighbor being Ce4+ or Ce3+. 140

Figure 67. The (A) Langmuir-Hinshelwood mechanism, (B) Eley-Rideal mechanism, and the (C) Mars-Van Krevelen mechanism [126]..... 147
Figure 68. The processing flow of the electrolyte-supported patterned anode full cells from polishing to cathode attachment to sputtering to full cell ready for testing. The final cell shows the cathode aligned with the pattern but not overlapping the electrical contact pad..... 152
Figure 69. Reference XPS spectra for Mo 3d and the accompanying crystal structure of each phase [122] 154
Figure 70. Pellets cracking after carburization process. 156
Figure 71. Weight change as measured by TGA of MoO_2 in a CO atmosphere at different temperatures. Taken from reference cited in text. 157
Figure 72. Different morphologies of Mo_2C derived from different carburization conditions [125] 158
Figure 73. SEM micrograph of a) as deposited molybdenum b) carburized in $20CH_4/80H_2$ at 700°C for 10 hours c) carburized in $20CH_4/80H_2$ at 800°C for 10 hours, d) carburized at $50CH_4/50H_2$ at 700°C for 10 hours and e) the pattern after carburization. 159
Figure 74. Raman spectra of commercial Mo_2C and MoO_3 powder. 160

LIST OF SYMBOLS AND ABBREVIATIONS

ALD	Atomic Layer Deposition
AP-XPS	Ambient Pressure X-ray Photoelectron Spectroscopy
ECR	Electrical Conductivity Relaxation
GDC	Gadolinium Doped Ceria
LCC	$La_{0.4875}Ca_{0.0125}Ce_{0.5}O_{2-\delta}$
LSCF	$La_{0.6}Sr_{0.4}Co_{0.2}Fe_{0.8}O_{3-\delta}$
ORR	Oxygen Reduction Reaction
SEM	Scanning Electron Microscopy
SOFC	Solid Oxide Fuel Cell
SDC	Samarium Doped Ceria
TEM	Transmission Electron Microscopy
TGA	Thermogravimetric Analysis
TPB	Triple Phase Boundary
YSZ	Yttria-Stabilized Zirconia

SUMMARY

Solid oxide fuel cells represent a scalable energy generation technology capable of operating at high efficiencies on multiple fuel sources. However, wide-spread implementation of SOFCs has been limited by the high degradation rate at current operating temperatures of 800-1000°C. Lowering the operating temperature to an intermediate range of 500-700°C will decrease the degradation phenomena, but will also decrease the catalytic activity of the electrodes. Modifying the surface of the electrodes is one method to increase the catalytic activity at these relatively low operating temperatures. This dissertation seeks to understand the role of surface modification on solid oxide fuel cell electrodes through conformal and non-conformal coatings.

An SOFC has three main components: the anode where the fuel is oxidized, the electrolyte which provides a conduction path for ions, and the cathode where the oxygen reduction occurs. As operating temperatures decrease, the cathode dominates the total cell resistance. Thus, it is important to focus efforts on improving the catalytic activity of the cathode. There are two strategies to improving performance of the cathode. The first is to rely on a single material to provide sufficient bulk and surface properties. However, this often results in a compromise of bulk conductivity and surface performance. The second strategy is to take a material with excellent bulk properties and modify the surface with another species to enhance catalytic activity. The surface modification route also allows for thin films and intricate morphologies on the surface that can provide unique effects only observed on a small length scale.

The state of the art cathode material is a strontium and cobalt doped lanthanum ferrite known as LSCF. It has demonstrated ideal bulk characteristics of mixed ionic and electronic conductivity that give high performance for the oxygen reduction reaction. Since LSCF has vast literature regarding behavior in different operating conditions, it was used as the backbone material. In order to investigate the important surface properties, it is necessary for the modifying material to have controllable properties like ionic and electronic conductivity. For this work, the properties of ceria were varied using samarium and praseodymium to investigate a range of conditions for conformal and nonconformal coatings.

The first part of this dissertation demonstrates an asymmetric cell testing platform that is used to better understand the effects of conformal film deposition. Depositing a conformal thin film into a porous cathode is nontrivial and requires exhaustive optimization of either solution or gas phase deposition techniques. Even then, if the backbone material and the coating material aren't very similar (in crystal structure, thermal expansion, etc), then the film will no longer be conformal after reaching SOFC operating temperatures. The asymmetric testing platform in this work was designed to focus on the effect of the thin film modification, which was accomplished by depositing a dense LSCF cathode on one side of an SDC electrolyte support with an accompanying porous LSCF counter electrode. Because of the high surface area of the counter electrode, the polarization resistances measured were dominated by the dense LSCF thin film. The planar dense film allows for precise control over the modification with conformal thin films via RF sputtering. The first part of the dissertation describes the fabrication and electrochemical characterization of

this testing platform, which demonstrated the ORR activity was the dominant feature in the impedance spectra.

The second part of the dissertation describes the surface modification with undoped ceria and samarium doped ceria. First, infiltration was used to modify the surface and it was seen that a change in morphology influenced the ORR activity. More specifically, for the undoped ceria, a more conformal morphology as opposed to a more dispersed, nano-island morpohology lead to lower impedance for the ORR. Using the asymmetric testing platform and sputtered ceria, it was found that the thickness of the conformal ceria influenced the ORR. Thinner films showed an increase polarization resistance, while thicker films showed a decreased polarization resistance. The increase in polarization resistance for the thinner films was explained by an increase in vacancy concentration as demonstrated through comparison of the impedance behavior under bias to a doped ceria thin film. Second, it was found infiltration with samarium doped ceria decreased the polarization resistance. Interestingly, the performance increase was independent of the mol% of the samarium doped into ceria. This goes against the conventional thinking that increasing ionic conductivity (by increasing samarium mol %) will lead to increasing surface exchange properties. Thin film conformal deposition of 20SDC demonstrated an overall increase in polarization resistance with increasing resistance correlating to film thickness. These last two results suggest that the ionically conducting surface modification reduces the oxygen through a surface mediated process that requires high surface nanoparticles.

The third part of the dissertation describes the work using praseodymium doped ceria as the modification material to better understand the role of ionic and electronic

conductivity in the ORR catalytic activity. Doping praseodymium into ceria increases both the ionic and electronic conductivity. Through infiltration, it was found that the optimal performance occurs at 50 mol% praseodymium in ceria even though 70 mol % exhibits higher electronic and ionic conductivities. Through XPS and TGA, it was found that amount of Ce^{3+} (i.e. reduced ceria) changes non-linearly with praseodymium dopant concentration. The 50 mol% doped ceria showed more Ce^{4+} available relative to the 30 and 70 mol% praseodymium concentration. Thus, it was found that oxygen ion vacancy concentration and electronic conductivity are not the only material properties relevant to increasing ORR activity. Instead, the results indicate a more nuanced view of oxygen reduction reaction and the correlation to bulk material properties.

In the end, this work describes a platform for the characterization of conformal thin film surface modification and demonstrates the potential to increase material performance beyond bulk material properties. Importantly, this work has shown the nuanced performance enhancement beyond traditional correlations to ionic and electronic conductivity.

CHAPTER 1. INTRODUCTION

1.1 Motivation

The modern world is defined by the insatiable demand for energy as standards of living increase throughout the world. The Energy Information Administration projects that global energy consumption will increase by 48% to 815 quadrillion BTU by 2040 driven in major part by growth in developing countries[1]. Meeting that demand requires technological advancements that accommodate a range of national priorities including economic and environmental constraints. The traditional forms of energy generation have relied on energy-intensive extraction of hydrocarbon fuels in the forms of oil and coal. This has literally fuelled the economic boom of the United States throughout the 19th and 20th centuries and resulted in a large infrastructure for energy transmission for residential, commercial, industrial and transportation applications. However, the long-term future of energy production will likely be driven by environmental and economic opportunities in renewable energy sources, as evidenced by recent trends in cost-competitive solar and wind resources and global agreements on sustainability efforts like the ratification of the Paris Agreement. Thus, it is important to explore technologies that can balance the many constraints for energy generation technology of the future.

Solid oxide fuel cells represent an attractive technology to meet these demands. SOFCs operate through the electrochemical oxidation of a fuel gas and thus are not constrained by the Carnot efficiencies of internal combustion engines. That allows SOFC systems to attain electrical efficiencies of >60%. Because they operate at relatively high temperatures of 600-1000°C, there is no requirement for expensive precious metal

catalysts. Additionally, these higher operating temperatures allow for greater fuel flexibility than traditional energy sources ranging from hydrogen to more energy dense hydrocarbons. For example, SOFCs can take advantage of the existing natural gas infrastructure and the recent boom in domestic natural gas supply. Figure 1 shows the energy consumption projections and the expected energy production from different resources[2]. The higher temperatures also allow for combined heat and power

a)

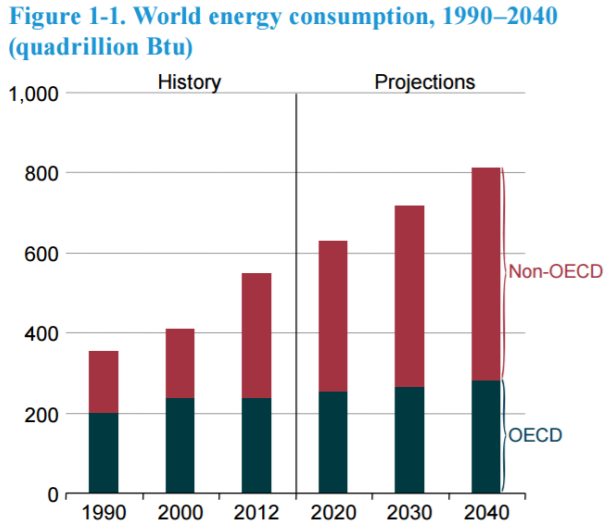

b)

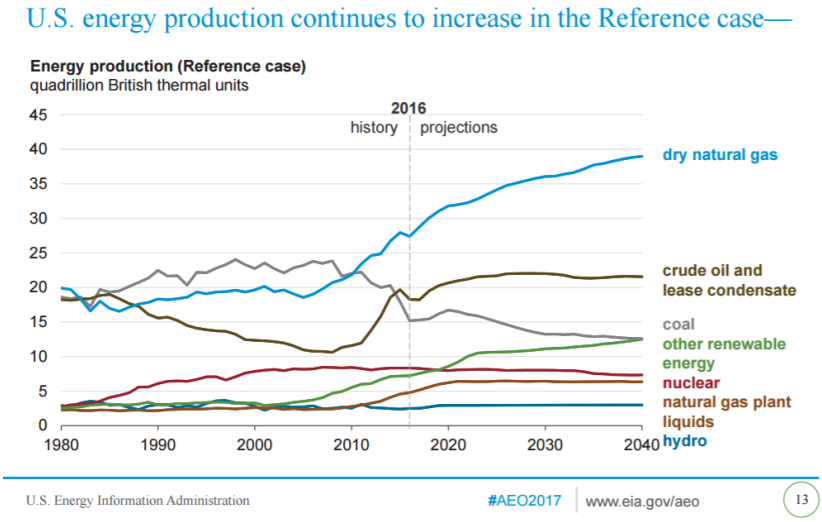

Figure 1. Projections of a) world energy consumption[1] and b) U.S. energy production through 2040[2].

applications, which can lead to overall system efficiencies approaching 80-90%[3], [4]. Another advantage is the ability to scale these systems to handle energy applications ranging from 1kW single home distributed energy sources to MW-scale base load power and heat. Applications range from large-scale stationary, high efficiency energy generation to fuel flexible transportation related to the electrification of commercial and non-commercial vehicles[5]. SOFCs also offer an opportunity for energy storage in what is called a Solid Oxide Electrolysis Cell (SOEC), which switches between electrolysis mode, when excess energy is generated from solar and wind installations, and fuel cell mode, when the hydrogen and oxygen can be used as the fuel and oxidant when electricity is in high demand[6], [7].

However, there are several constraints that limit the wide-spread commercialization of SOFCs. Because of the high operating temperatures, the active materials degrade over time. SOFCs in real world applications must maintain continuous performance for lifetimes on the order of 40,000 hours, but often degrade on the order of a few percent per hundred hours rather than the Department of Energy target of 0.2% per 1,000 hours[8]. The degradation often occurs through precipitation of secondary phases from the bulk or adverse reactions between components like the sealing material and the cathode[9]. One way to decrease the degradation is to operate at lower temperatures. However, there are trade-offs that come with changing the operating temperature as highlighted in Figure 2. For example, as temperatures decrease carbon deposition from CO/CO_2 mixtures become more favourable but carbon deposition from hydrocarbon fuels becomes less favourable[10]. Lower temperatures also allow for more economical support materials such as stainless steels instead of high temperature nickel-based alloys. Unfortunately, as

temperature decreases, the resistances for the electrochemical reactions increase. The intermediate temperature range of 500-800°C has been identified as a compromise between decreasing reaction rates and increasing material durability[11], [12]. Thus, it is important to engineer materials in SOFCs to enhance catalytic activity at these intermediate temperatures. The purpose of this dissertation is to explore routes to increase performance of the SOFC electrodes through surface modification to increase performance at these intermediate operating temperatures and identify principles that will guide rational design of the next generation of SOFC technology.

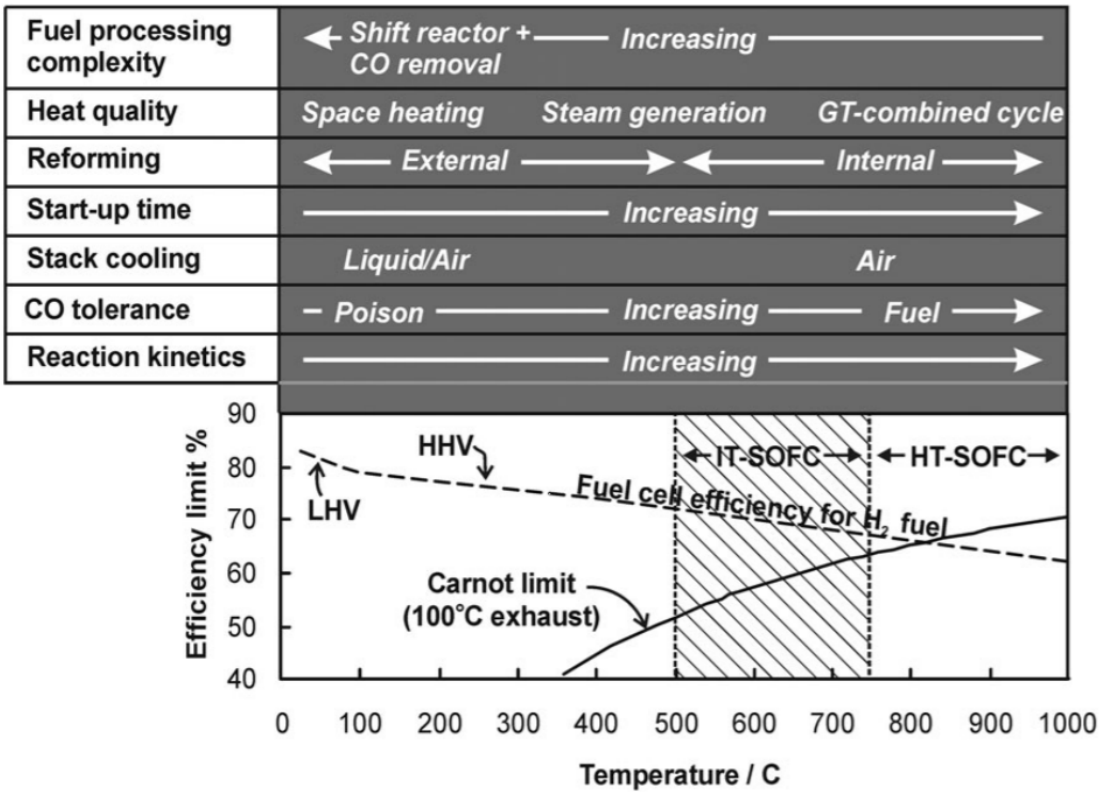

Figure 2. A summary of trade-offs related to operating temperature of solid oxide fuel cells[11].

1.2 Research Objectives

The research in this dissertation focuses developing a better understanding of surface modification to enhance catalytic activity of the cathode, which leads to future rationale design of cathode materials. The objectives are as follows:

- Develop an asymmetric cell testing platform that enables comparison and fundamental insight into surface modification of SOFC cathodes
- Vary the ionic and electronic properties of the surface modification to understand the important factors influencing the oxygen reduction reaction and characterize under realistic operating conditions.
- Understand the role of conformal films and film thickness on performance for the oxygen reduction reaction and the fuel oxidation by characterizing with the impedance spectroscopy

1.3 Dissertation Structure

After a background on fundamental operating principles of solid oxide fuel cells, the relevant literature on cathode materials and thin film experiments will be reviewed. From there the technical approaches will be described. Chapter 2 will show the development of an asymmetric cell testing set up that was designed to test thin film coatings. Chapter 3 will use that platform to better understand the role of doped and undoped ceria coatings on the LSCF backbone. Chapter 4 will examine the praseodymium-doped ceria system to identify the role of oxygen ion conductivity on ORR performance. The final part of the dissertation will be a summary and recommendations for future work. An appendix

discusses some of the work in anode catalysts specifically with respect to molybdenum carbide as a hydrocarbon catalyst for enhanced activity and increased coking tolerance.

CHAPTER 2. BACKGROUND

2.1 Solid Oxide Fuel Cells

Fuel cells are electrochemical devices that create energy through the oxidation of a fuel source. The cell consists of three main components: the anode, electrolyte, and cathode. The porous anode is where the fuel is oxidized and must support ionic and electronic conductivity. This is often achieved through a ceramic-metal composite, where nickel is the metal and the ceramic is the same as the electrolyte used. The electrolyte must be dense and only ionically conductive so that electrons are forced through an external circuit. The porous cathode must also support electronic and ionic conductivity, and is the electrode where the oxygen is reduced.

The different fuel cell technologies are defined by their electrolyte as seen in Figure 3, which show five different fuel cell technologies[13]. Solid oxide fuel cells, as the name indicates, conducts either oxygen anions or protons through an oxide electrolyte. Because it is an all solid-state system, high operating temperatures are needed to overcome the activation barrier of ion diffusion through the lattice. However, it is capable of internally reforming hydrocarbon fuels. Also, the higher operating temperatures do not require the expensive precious metal catalysts that are used in proton exchange membrane fuel cells. Molten carbonate and phosphoric acid fuel cells operate in the low to intermediate temperature range, but utilize a liquid electrolyte that introduces sealing challenges and limits applications to stationary power generation.

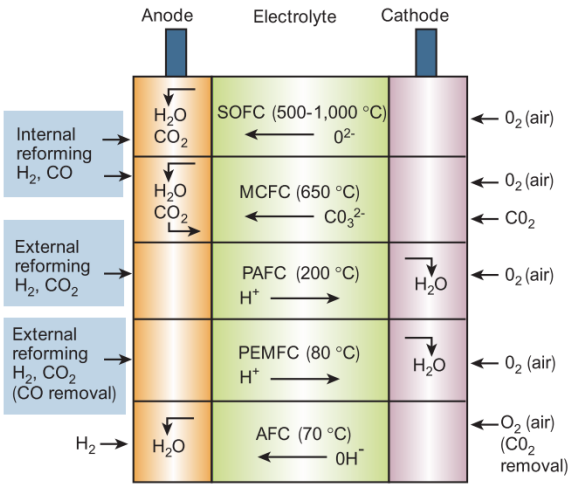

Figure 3. Schematic showing the electrolytes that define the different fuel cell technologies[13].

2.2 Thermodynamics

2.2.1 Thermodynamic Foundation and Nernst Equation

The fundamental reaction in a fuel cell reaction is the production of water from hydrogen and oxygen, which can be separated into two half reactions as indicated in Eq 1.

Anode	$H_2 \rightarrow 2H^+ + 2e^-$	
Cathode	$\frac{1}{2}O_2 + 2e^- \rightarrow 2O^{2-}$	
Overall	$H_2 + \frac{1}{2}O_2 \rightarrow H_2O$	**Eq 1**

The electrochemical potential is given by the Gibbs free energy change presented in Eq 2, where G is the Gibbs free energy, U is the internal energy, T is temperature in Kelvin, S is entropy, p is pressure and V is volume.

$$G = U - TS + pV \qquad \textbf{Eq 2}$$

Differentiating Eq 3 and assuming constant temperature and constant pressure shows that the maximum electrical work a system can perform is the negative of the Gibbs free energy difference.

$$dG = dU - TdS - SdT + pdV + Vdp$$

$$dG = (TdS - dW) - TdS - SdT + pdV + Vdp$$

$$dG = (TdS - pdV - dW_{elec}) - TdS - SdT + pdV + Vdp$$

$$dG = -dW_{elec} \quad \text{OR} \quad \Delta G = -W_{elec} \qquad \textbf{Eq 3}$$

The electrical work a system can also be calculated from the energy required to move a charge (Q) through an electrical potential difference (E), where n is the number of mols of electrons transferred and F is Faraday's constant.

$$W_{elec} = EQ$$

$$W_{elec} = E(nF) \qquad \textbf{Eq 4}$$

Relating Eq 3and Eq 4 demonstrates that the electrical potential is given by the molar Gibbs free energy change of the reaction resulting in Eq 5. This electrical potential is known as the reversible cell voltage.

$$\Delta G_{molar} = -nFE \qquad \textbf{Eq 5}$$

The Gibbs free energy change for the fuel cell reaction in Eq 1 and water in the liquid phase is -229kJ/mol, which gives a reversible voltage of +1.229V according to Eq 5[14]. Including the latent heat of vaporization for gaseous water instead of liquid water, the reversible voltage is 1.18V. This is the maximum possible potential that can come from the system using hydrogen as the fuel and oxygen as the oxidant. Remember that the Gibbs free energy is a function of temperature.

Eq 6 shows that the temperature dependent reversible cell voltage (E_T) is a function of the molar entropy change. For the H_2-O_2 fuel cell with a $\Delta S_{molar} = -44.34\, J/mol \cdot K$, this translates into approximately 23 mV decrease in reversible voltage for every 100 degrees increase in temperature. Conversely, lowering the operating temperature increase the reversible cell potential, which is another positive attribute of intermediate operating temperatures.

$$dG = -SdT + Vdp$$

$$\left.\frac{dG}{dT}\right|_p = -S$$

$$\left.\frac{d\Delta G_{molar}}{dT}\right|_p = -\Delta S_{molar}$$

$$\frac{d(-nFE)}{dT} = -\Delta S_{molar}$$

$$E_T = E^0 + \frac{\Delta S_{molar}}{nF}(T - T_0) \qquad \textbf{Eq 6}$$

The Gibbs free energy of a reaction also varies with the concentration of the products and reactants. This variation in Gibbs free energy with concentration is defined by the chemical potential (μ_i^α) of a given species (i) in a given phase (α) as illustrated in Eq 7, where the right-hand side of the equation represents how much the Gibbs free energy changes for an infinitesimal increase in species i.

$$\mu_i^\alpha = \left(\frac{\delta G}{\delta n_i}\right)_{T,p,n_{j\neq 1}} \qquad \textbf{Eq 7}$$

The chemical potential is related to concentration through the term activity (a) as shown in Eq 8. The logarithmic dependence arises from the relative impact of adding atoms; in other words, adding a few particles to a small system is expected to have a large effect on the chemical potential[15]. On the other hand, adding a few particles to a large system will most likely have little effect on the chemical potential.

$$\mu_i = \mu_i^0 + RT \ln a_i \qquad \textbf{Eq 8}$$

Combining Eq 7 and Eq 8 gives the change in Gibbs free energy for a system of i chemical species for a small change in amount of that species (n_i):

$$dG = \sum_i \mu_i \, dn_i = \sum_i (\mu_i^0 + RT \ln a_i) dn_i \qquad \textbf{Eq 9}$$

For an arbitrary chemical reaction, the molar Gibbs free energy of a reaction is given by Eq 10.

$$xA + yB = wM + zN$$

$$\Delta G_{molar} = (w\mu_M^0 + n\mu_N^0) - (x\mu_A^0 + y\mu_B^0) + RT \ln \frac{a_M^w a_N^z}{a_A^x a_B^y}$$

$$\Delta G_{molar} = \Delta G_{molar}{}^0 + RT \ln \frac{a_M^w a_N^z}{a_A^x a_B^y} \qquad \textbf{Eq 10}$$

Combining Eq 5 and Eq 10 yields the Nernst equation which takes into account the electrical and chemical contributions to the reversible cell voltage. The equation for calculating this Nernst potential is shown in Eq 11 where *a* is the activity of the species and v_i is the stoichiometric coefficient.

$$E = E^0 - \frac{RT}{nF} \ln \frac{\prod a_{products}^{v_i}}{\prod a_{reactants}^{v_i}} \qquad \textbf{Eq 11}$$

For the H_2-O_2 fuel cell reaction in Eq 1, the Nernst equation is:

$$E = E^0 - \frac{RT}{nF} \ln \frac{a_{H_2O}}{a_{H_2} a_{O_2}^{1/2}} \qquad \textbf{Eq 12}$$

The Nernst equation can also be derived when the electrochemical potential of a species is the same at both electrodes. In that case, the chemical potential is exactly balanced out by the electrical potential[15].

For an ideal gas, which is the most likely case in a solid oxide fuel cell, the activity can be approximated by the partial pressure of the gas. For a nonideal gas, an activity coefficient is used to describe the deviation from ideal behaviour.

2.2.2 Equilibrium Defect Reactions

The performance of SOFC materials is based on the dominant mobile electrochemical species, which varies with doping concentration, partial pressure of oxygen and temperature. Identifying the conductivity determining species requires a point defect model which consists of writing mass action laws for every case that can satisfy electroneutrality in the bulk of the material. For example, ceria can have intrinsic conductivity due to the reduction of Ce^{4+} to Ce^{3+} (Eq 13), from an anti-Frenkel defect (Eq 14) or from the generation of an electron/hole pair (Eq 15). Ceria can also be doped with an aliovalent species like samarium that introduces a vacancy to balance the 3+ dopant on the 4+ lattice site (Eq 16).

$$O_O^x \leftrightarrow V_O^{\cdot\cdot} + 2e' + \frac{1}{2}O_2 \qquad \textbf{Eq 13}$$

$$nil \leftrightarrow V_O^{\cdot\cdot} + O_i'' \qquad \textbf{Eq 14}$$

$$nil \leftrightarrow e' + h^{\cdot} \qquad \textbf{Eq 15}$$

$$Sm_2O_3 + Ce_{Ce}^x + 2O_O^x \leftrightarrow 2Sm_{Ce}' + V_O^{\cdot\cdot} + 4O_O^x \qquad \textbf{Eq 16}$$

Each equation can be represented by a mass action law with an Arrhenius form such as:

$$[V_O^{\cdot\cdot}]n^2 P_{O_2}^{1/2} = K_R(T) = k_R \exp\left(\frac{-E_R}{kT}\right) \quad \textbf{Eq 17}$$

Where $[V_O^{\cdot\cdot}]$ is the concentration of oxygen ion vacancies, n is the concentration of electrons, $P_{O_2}^{1/2}$ is the partial pressure of oxygen, $K_R(T)$ is the mass action coefficient, k_R is the reaction constant, E_R is the oxygen vacancy formation energy, *k* is Boltzmann's constant and *T* is temperature. After all the possible equations governing conductivity have been written, a charge neutrality equation can be developed that balances the charges of the possible positive and negative species:

$$n + [O_i''] + [Sm_{Ce}'] = p + 2[V_O^{\cdot\cdot}] \quad \textbf{Eq 18}$$

By using a Brouwer approximation, an isothermal defect diagram can be presented under varying P_{O_2}atmospheres as shown in Figure 4[16]. The approximation is based off the assumption that there is a single dominant defect mechanism for a given region. Using this Brouwer diagram, it is possible to understand the contributions to conductivity in different regions based on the slope of the carrier concentration. For example, in Region II, the conductivity is dominated by oxygen ion vacancies created through the aliovalent doping mechanism and thus you would expect no change in ionic conductivity because the concentration of oxygen ion vacancies is fixed by the dopant concentration within that range of oxygen partial pressures.

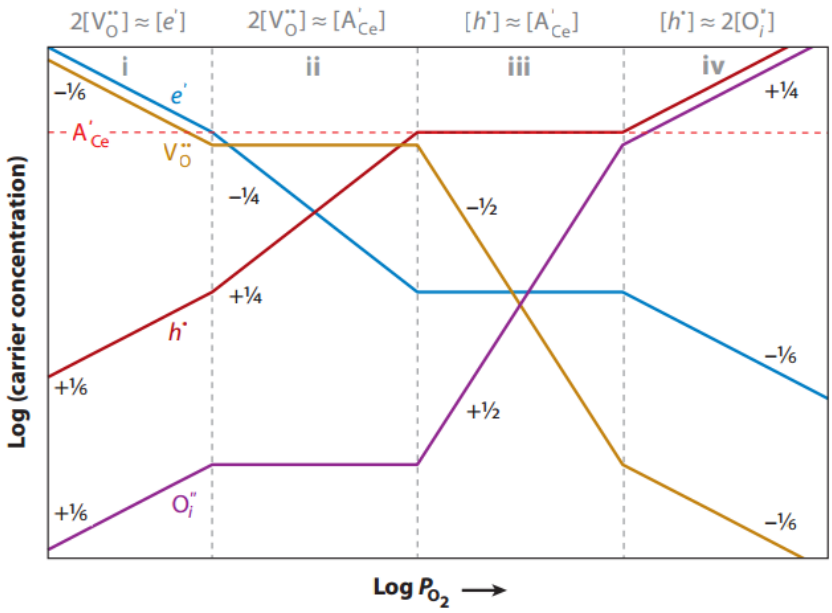

Figure 4. A Brouwer diagram for acceptor-doped ceria[16].

2.3 Kinetics

The thermodynamic values provide a foundation for understanding the electrochemical kinetics in SOFCs. For a given electrochemical reaction, there exists an activation barrier that must be overcome before the reaction can take place. The probability of a reactant species being in an activated state is defined through statistical mechanics arguments as:

$$P_{activated} = e^{-\Delta G/RT} \qquad \textbf{Eq 19}$$

where $P_{activated}$ is the probability of finding the reactant species in the activated state, ΔG is the energy barrier between the reactants and the activated species, R is the universal gas constant and T in temperature in Kelvin. In order to determine

While the thermodynamic efficiency is dictated by the Nernst equation, there are several polarization losses that reduce cell efficiency as shown in Figure 5. Activation polarization is the energy loss due to the activation barrier encountered for the reaction to proceed at the electrode. In response to an asymmetric activation barrier, which occurs when the final state is at a lower energy then the initial state, an electric potential difference is generated across the electrode known as the Galvani potential. Adding these potentials together gives the observed reversible open circuit voltage. In order to have current flow, the system needs to be biased toward the forward reaction. The Butler-Vollmer equation describes the relationship between the activation overvoltage and the current density observed:

$$j = j_0^0 \left(\frac{c_R^*}{c_R^{0*}} e^{\alpha n F \eta/(RT)} - \frac{c_P^*}{c_P^{0*}} e^{-(1-\alpha) n F \eta/(RT)} \right) \qquad \textbf{Eq 20}$$

Where j is the exchange current density, j_0^0 is the exchange current density at standard concentrations, $c_R^{0*}$is the initial reactant (or product) concentration at the surface, c_R^* is the actual surface concentration of the reactant (or product), α is term to describe the symmetry of the activation barrier, η is the activation overvoltage, and n, F, R and T have their usual meanings. These activation losses can be mitigated by new catalysts on both the anode and cathode side that can affect the gas adsorption, dissociation and other intermediate species involved in the multiple-step oxidation or reduction process. Note in

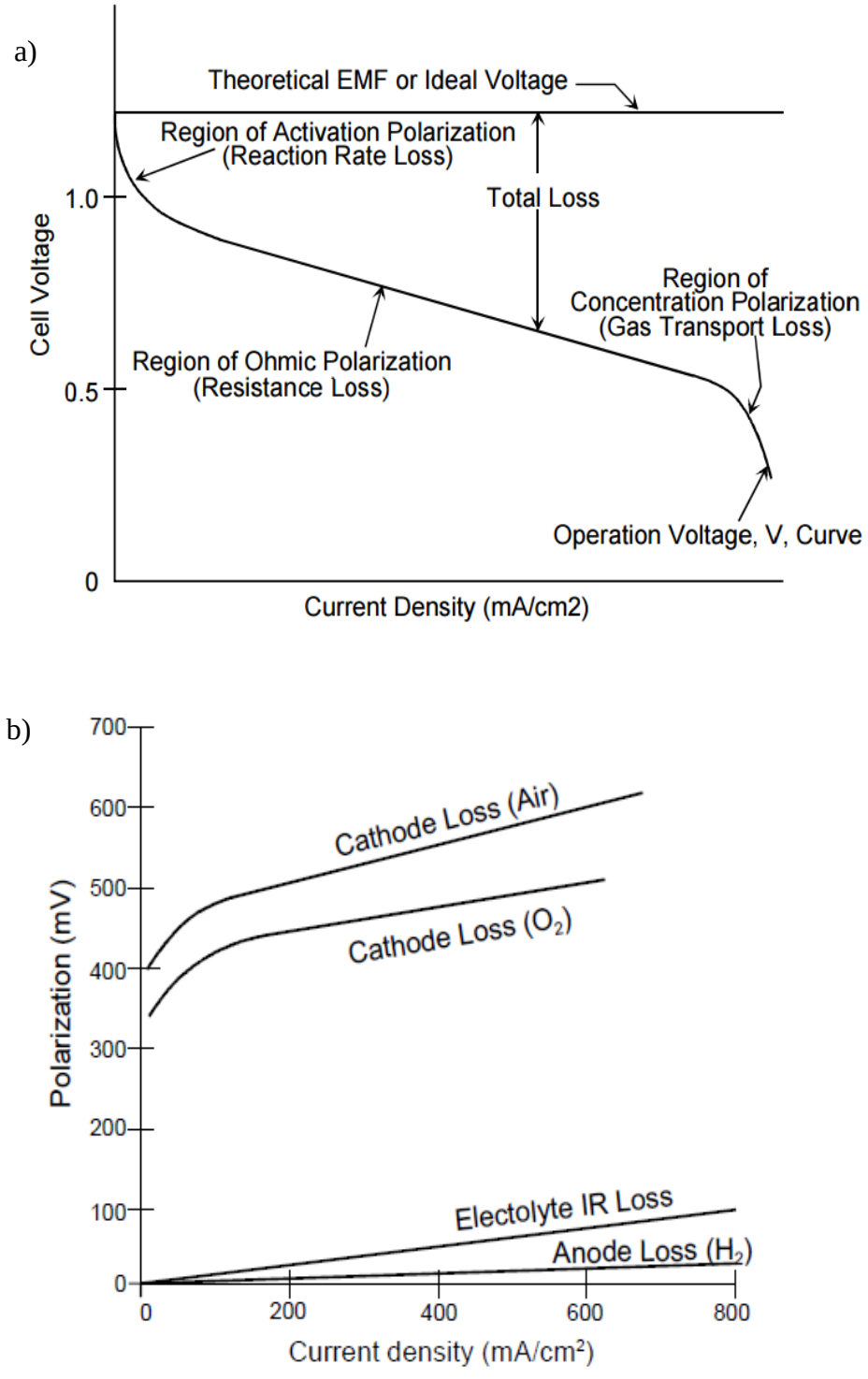

Figure 5. a) A typical IV curve showing the fuel cell polarization losses and b) the relative contributions for the anode, cathode and electrolyte[14].

Figure 5 b) the relative magnitude of losses associated with the anode, electrolyte and cathode. The middle region of Figure 5 a) exhibits a linear decrease with increasing current density due to ohmic losses in the electrolyte, electrodes, interconnects and current collectors as shown in the following equation:

$$\eta_{ohm} = iR \quad \text{where} \quad R = R_{electronic} + R_{ionic} + R_{contact} \qquad \textbf{Eq 21}$$

Ohmic losses from ionic conduction in the electrolyte become larger as temperature decreases and thickness increases. To minimize ionic resistance, the electrolytes of planar SOFCs are thin films (on the order of 20 μm) deposited on a porous anode support. To compare cells of different sizes and with different materials, the ohmic resistance is usually normalized by area (Area Specific Resistance) which is measured in Ωcm^2. The slope of the linear portion of this IV curve is approximately the resistance of the electrolyte, but really incorporates all ohmic resistances in the cell. Another way to determine the ASR is through impedance spectroscopy, where the ohmic resistance is the real value of the resistance for which the imaginary impedance is zero.

At high current densities, mass-transport and reaction rates cannot keep up with the demanded current, which result in concentration polarization losses. The loss can be quantified using Fick's first law and the Nernst equation:

$$J = \frac{i_{lim}}{nF} = \frac{-D(C_{bulk} - C_{surface})}{\delta x} \text{ when rearranged } \frac{C_s}{C_B} = 1 - \frac{i}{i_{lim}}$$

$$E_{i=0} = E^o + \frac{RT}{nF} \ln C_B \text{ and } E_{i \neq 0} = E^o + \frac{RT}{nF} \ln C_S$$

$$\Delta E = \eta_{conc} = \frac{RT}{nF}\ln\frac{C_S}{C_B} = \frac{RT}{nF}\ln\left(1 - \frac{i}{i_{lim}}\right) \qquad \textbf{Eq 22}$$

Where i_{lim} is the limiting current and R, T, n, F have their typical definitions. This assumes that the concentration polarization is much larger than the activation polarization, which is appropriate for the relatively high operating temperatures of solid oxide fuel cells. The difference in surface concentration also affects the symmetry of the activation barrier as previously described in the Butler-Vollmer equation.

2.4 Increasing Cathode Performance

Increasing performance of the entire solid oxide fuel cell relies on improvements in each component: anode, electrolyte and cathode. On the anode, the hydrogen oxidation reaction has been shown to relatively more efficient with much of the effort on establishing oxidation tolerance and identifying hydrocarbon catalysts to take advantage of more energy dense fuels. Advances in thin film fabrication and discovery of materials with higher ionic conductivity have greatly enhanced performance of electrolytes. Thus there is significant motivation to focus efforts on improving the oxygen reduction reaction. As previously shown, the cathode overpotential is the largest contribution of the overall resistances in an operating fuel cell and will only increase as a fraction of the total contribution at lower temperatures due to a higher activation energy. The following overview of the current status of SOFC cathodes draws from extensive reviews in the literature[17]–[19].

The cathode can take two forms: a composite of ionic and electronical conducting phases or a single mixed conducting phase. In the traditional composite form, an ionic

conductor (usually the same material as the electrolyte) and an electronic conductor like (La,Sr)MnO_3 (LSM) are physically mixed and then fired as a cathode. This strategy mimics the approach of the anode. Contrary to the anode, there is a large oxide material set that is stable in the oxidizing environment of the cathode. The more common approach with materials is to use a single mixed conducting phase like $La_xSr_{1-x}Co_yFe_{1-y}O_3$ (LSCF) which has a sufficient oxygen ion and electronic conduction. The key morphological difference between the two strategies comes from the active area for the reaction. For a composite, the oxygen reduction reaction will occur where electrons, gaseous oxygen and ions are all present. The interface between the gas the electron conducting phase and the ion conducting phase is known as the triple phase boundary. The advantage for a mixed conductor lies in the increase of the surface area available for the reaction to occur. Instead of being confined to the linear geometry of intersecting phases, the ORR on a mixed conductor can take place across the entire exposed surface area. Additionally, the composite cathode must maintain percolation of the electronic phase or some of the triple phase boundaries will not be active. Thus, there may be a sacrificed in active surface area to maintain continuity in the electrically conducting phase.

A large amount of research has shown that overall cell performance scales with the triple phase boundary length. However, the exact progression of ORR at the triple phase boundaries is not completely understood[17]. In general, it is thought that oxygen molecules absorb on to the surface where they are catalytical or electrocatalytically reduced to form an electroactive species. Either before or after this reduction, the species must be transported along the surface or triple phase boundary of materials and then transfer into the bulk of the ionic conductor. Traditional electrochemical kinetics, which traditionally

focuses on the surface of a metal electrode with a liquid electrolyte, does not perfectly apply because gas-diffusion electrodes are often limited by multiple rate-determining steps[17].

In order to better understand the ORR process, it is helpful to simplify the materials used. For example, using platinum or silver as the cathode has been the prototypical way to study behaviour of the triple phase boundary. These experiments have yielded important insight in the challenges in applying traditional electrochemical methods to gas diffusion electrodes. For example, calculating the Tafel slope to predict limiting kinetics is often used in liquid-based electrochemistry, but can create misleading conclusions for a gas-diffusion electrode. Adler pointed out through Mizusaki's derivation that a Nernstian relationship exists between the applied potential and activity of electroactive oxygen on a platinum surface[17]. That means the surface concentration at the triple phase boundary would vary logarithmically with potential. If the rate of adsorption/diffusion depends on concentration of the species, then the current will vary with logarithmically with overpotential and appear to exhibit Tafel behavior. That being said, a large body of literature correlates performance with the geometric length of the triple phase boundary. In an attempt to correlate structure to performance, early researchers studied platinum on YSZ and took lessons from gas diffusion electrodes in hydrogen oxidation[17]. One of the big take-aways from comparison to fuel electrodes in solution and polymer gas diffusion electrodes is the possibility that diffusion processes can co-limit performance below the limiting current density[20]. Before delving into the foundational literature on the ORR reaction, it is important to note that processing, microstructure, temperature, polarization, partial pressure of oxygen and many other factors influence overall cell performance. Thus,

even in the ideal platinum on YSZ experiments, there can be variation due to the actual testing and fabrication conditions that could impact the data and subsequent interpretation. Thus, there can be a large spread in data for relatively simple systems with minimal components.

There are few lessons to draw from early work of platinum and silver on YSZ. Kleitz and collaborators studied silver microelectrodes on YSZ[21]. Their impedance data showed two major arcs with the larger one at lower frequencies ascribed to the adsorption and diffusion of atomic oxygen inside the silver microelectrode due to the variation of the resistance and capacitance for impedance data fit with conventional circuit elements. The mechanism they describe is that atomic oxygen dissolved in the silver where it is reduced to an anion and then enters the electrolyte at the triple phase boundary. This would explain why the capacitance varies nearly to the cubic of the partial pressure of oxygen because the volume of the silver is involved in the capacitive effect. A chemical potential gradient of oxygen is then generated in steady state that causes more oxygen to adsorb and dissociate on the surface and then diffuse to the triple phase boundary. Verkerk and Burgraff also described a mechanism limited by both diffusion and adsorption in platinum on YSZ [22]. After subtracting the double-layer capacitance of the metal/electrolyte interface and the resistance due to the electrolyte, the impedance spectra showed a 45° line in a Nyquist plot, which indicates that a diffusion limitation in the process[23]. However, a 45° line in a Nyquist plot does not necessarily indicate finite-length diffusion. The same spectra would result from an system that is reduced to semi-infinite diffusion including if the system is limited by kinetic processes in the steady-state[24]. The concept of a co-limited process is exemplified in Adler's review[17]. The process can be thought of as two distinct processes

that involves the adsorption of gas molecules on the surface and then an electrochemical reaction that occurs at the triple phase boundary that depletes the adsorbed species. As the surface species is reacted at the interface and pulled into the electrolyte, a gradient of adsorbed species near the interface will begin to develop. Thus, the adsorbed species will move under a surface concentration gradient into an equilibrium at which the increase in surface sites available is balanced by the decreasing rate of diffusion due to a longer transport path. That translates into a compromise between exchange coefficient (k) and diffusivity (D) where the utilization length (l_δ) is defined as:

$$l_\delta \sim \sqrt{\frac{D}{k}} \qquad \textbf{Eq 23}$$

This utilization length brings together the co-limited terminology because both values are important in determining the rate of the ORR by determining the active region, which can vary with microstructure, grain size and dopant level among many other factors. The dependence on these multiple factors makes it difficult to ascribe better overall performance to either value especially among materials that have similar performance but different diffusivity and surface exchange coefficients. The resulting impedance spectra will vary depending on those diffusivity and surface exchange values as seen in Figure 6. The tear drop shape of the impedance arc is due to the Warburg impedance (45^o line) that is associated with diffusion controlled reactions.

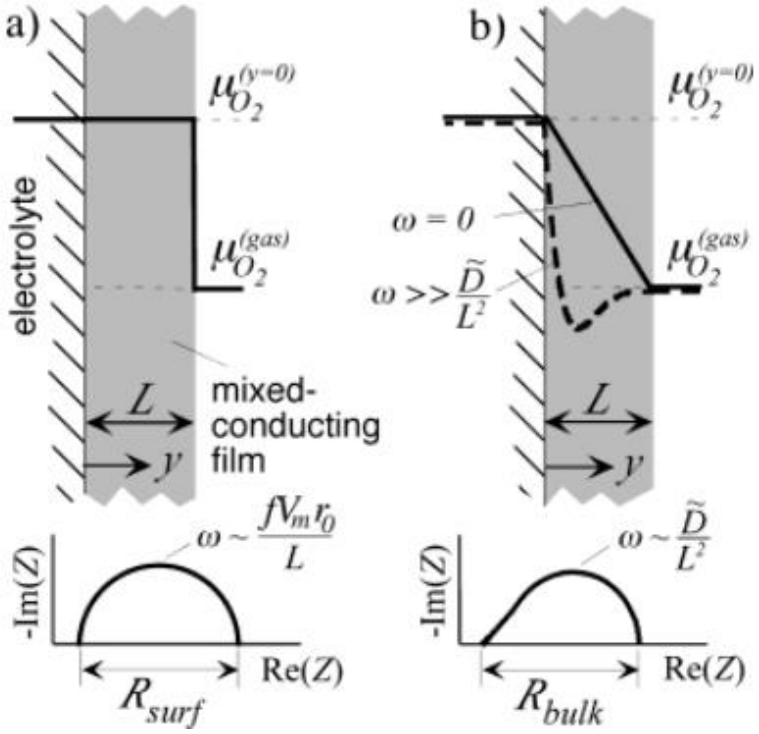

Figure 6. Two models where a) shows the impedance spectra if the ORR overall reaction is limited by surface adsorption and b) the ORR reaction is limited by diffusion of the oxygen anion through the mixed conducting film[17].

While the extreme cases are better understood, models to describe the actual behaviour lies somewhere in between without a well-defined breakdown of which processes are limiting, which brings up the idea of co-limiting reactions occurring in SOFC cathodes.

Increasing performance of the cathode for oxygen reduction reaction has been characterized by two effective rate constants k (oxygen surface exchange) and D (oxygen bulk diffusivity). With that in mind, it has been generally understood that both oxygen vacancy concentration and electronic conductivity play a role in enhancing surface exchange coefficient and the ORR. Because the contribution from each component is not well-developed, it is helpful to consider recent literature to see how performance after

surface medication correlates with both vacancy concentration and electronic conductivity. There are two main surface modification strategies for SOFC cathodes using solution infiltration. The first involves infiltrating a new material on a cathode backbone. The second introduces the infiltration solution on a porous electrolyte support to create a thin film of the cathode on the electrolyte backbone. Obviously, any material infiltrated on a porous electrolyte backbone would need to reach a percolation threshold on the surface to conduct electrons through the external circuit. The major focus for this review is surface modification using a homogenous cathode as the backbone.

2.4.1 Ionically Conductive Infiltrates

Infiltration of the ionically conducting infiltrates is believed to increase the surface exchange due to the oxygen vacancies and oxygen storage ability[25]. For example, infiltrating 20SDC into an LSCF backbone demonstrated a reduction in polarization resistance until a critical loading after which the performance decreases[26]. Figure 7 shows the impedance spectra and the calculated interfacial resistance varies with loading. Other groups have also shown an increase in performance with doped ceria infiltration including YDC[27]. Xia and coworkers demonstrated through a theoretical model using a sphere-packed framework that the infiltrated electrodes increased the triple phase boundary length, which is responsible for the enhancement[28]. Leng showed experimentally that the infiltration of GDC was able to reduce LSM sintering and also attributed the increase in performance to increase in triple phase boundary[29]. It is very common for authors to attribute enhancement after infiltration to an increase in surface area. However, very few authors perform BET measurements on the porous cathodes to normalize the polarization resistance by the surface area. Instead, it is generally accepted to normalize by the top down

surface area. This makes comparisons between different research groups slightly more complicated. For example, two cells could exhibit the same polarization resistance when normalized by top down area, but could have very different surface areas due to differences in cathode thickness, porosity, etc. If normalized by actual surface areas, there would be significant differences. That being said, the overwhelming majority of polarization data is normalized by top down area. Other examples of doped ceria on LSM can be found in the review by Ding et al [30].

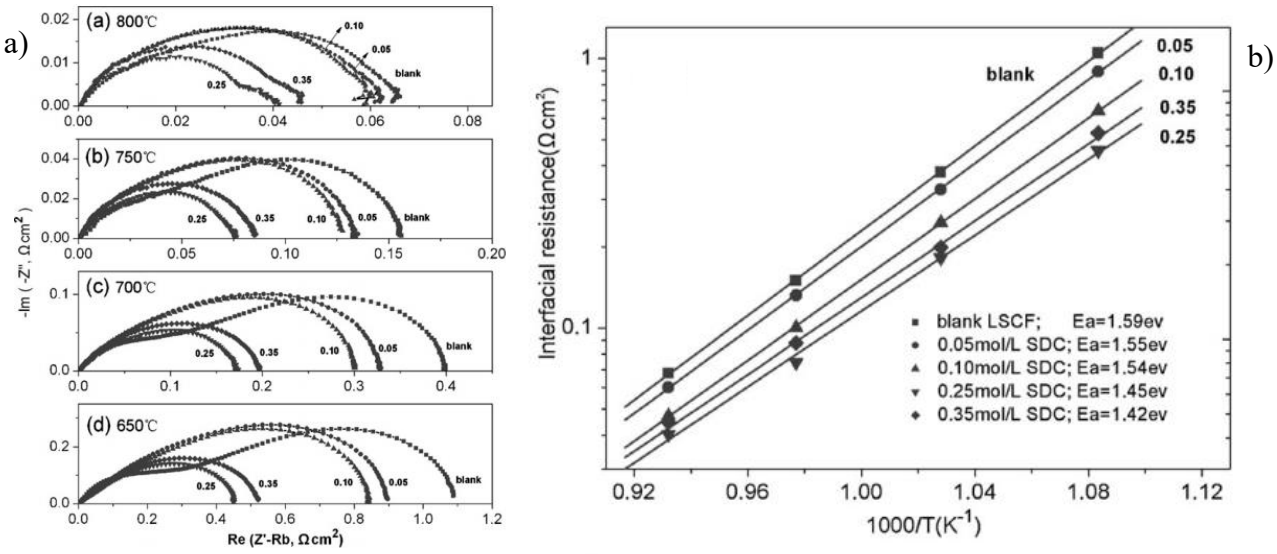

Figure 7. The a) impedance spectra and b) the plot of interfacial resistance versus inverse temperature[26].

The performance of the cathode has also been shown to scale with increasing ionic conductivity of the infiltrated compound. When yttrium stabilized bismuth oxide (YSB) was infiltrated into an LSM backbone, the polarization resistance was lower than an SDC infiltrated LSM cell as fabricated in the same experiment[31]. In that case YSB has higher ionic conductivity than SDC. While the performance trended with ionic conductivity, it's difficult to draw a direct correlation because of the change in material from a bismuth oxide

to a cerium oxide host material. Hong et al examined the oxygen surface exchange properties of $Sm_xCe_{1-x}O_{2-\delta}$ (SDC) infiltrated on an $La_{0.6}Sr_{0.4}Co_{0.8}Fe_{0.2}O_{3-\delta}$ backbone[32]. The authors found that the surface exchange coefficient as measured through ECR followed the trend of conductivity in Sm-doped ceria, i.e increasing with increasing samarium dopant with a peak at 0.2 and then a decrease with subsequent increase in samarium mol fraction. They also found that with the same dopant concentration, the performance varied with loading with a maximum at 0.86mg/cm^2. Above that loading, the deposited film had less cracks and became a more dense film. It is important to note that the deposition technique was a slurry coating, which resulted in film thicknesses on the order of 3-5μm as opposed to traditional infiltration of nitrates which operates on a length scale an order of magnitude or two smaller. Their conclusion was that the oxygen vacancies are critical to the surface exchange reaction, but the length scale of the coating may be a significant aspect of that explanation.

The interesting aspect to the doped ceria surface modification is that the surface exchange coefficient of GDC as calculated through isothermal isotope exchange method by Armstrong et al and Lane et al was shown to be orders of magnitude below the LSCF surface exchange coefficient[33], [34]. However, infiltrating doped ceria on LSCF increases the surface exchange coefficient of the cathode. Saher et al explored the influence of ionic conductivity of infiltrates on an LSCF backbone using ECR and isotope exchange to better understand the reason for the increase. They showed that Gd_2O_3 and CeO_2 infiltration decreased the surface exchange coefficient while GDC enhanced the surface exchange coefficient. The isotope exchange measurements suggested that the surface exchange is limited by the dissociative absorption, which in their view excluded the

possibility of the spill over mechanism as the reason for improvement. However, they were not able to describe an alternative mechanism.

The ionic conductivity may not be the only indicator for performance of a given material. Liu et al explored modifying an LSCF backbone with $La_{0.4875}Ca_{0.0125}Ce_{0.5}O_{2-\delta}$ (LCC)[35]. LCC has a much lower ionic conductivity as compared to SDC and GDC, but supports a large amount of oxygen ion vacancies. The authors compared two composites, one where LCC was physically mixed with LSCF and one where the LCC was deposited on the surface. The LCC/LSCF physical mixture showed an increase in polarization, which makes sense due to the low ionic conductivity of the bulk phase. However, when the LCC was infiltrated, the polarization resistance decreased significantly thus highlighting the role of oxygen ion vacancies in the ORR.

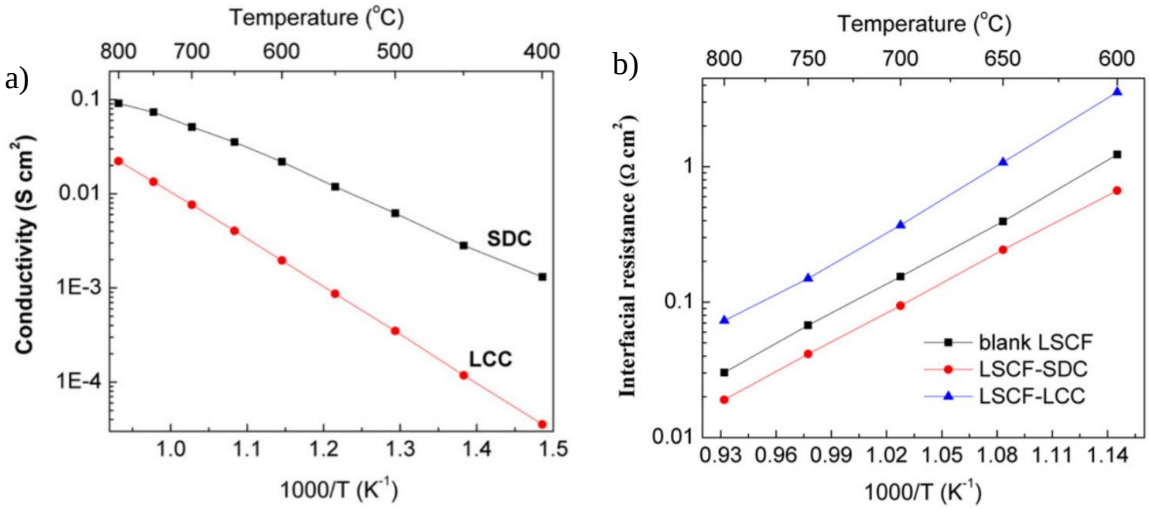

Figure 8. a) Comparison of conductivity between SDC and LCC and b) a comparison of interfacial resistance between LSCF, a physical mixture of LSCF-LCC and a physical mixture of LSCF-SDC [35]

While it may be tempting to try and increase the oxygen ion vacancy concentration as much as possible, there are important degradation considerations to be aware of. Tsvetkov et al modified the surface of LSC with cations whose binary oxides had either lower or higher enthalpies of oxygen vacancy formation[36]. They found that the less reducible cations improved the oxygen exchange coefficient and decreased strontium segregation. It is understood that the accumulation of positively charged oxygen vacancies on the surface create a driving force for the effective negatively charged strontium dopants to segregate to the surface and turn in to an inert strontium oxide that degrades performance. Thus, they found a volcano relationship between the reducibility of the infiltrated material and the surface exchange coefficient as shown in Figure 9.

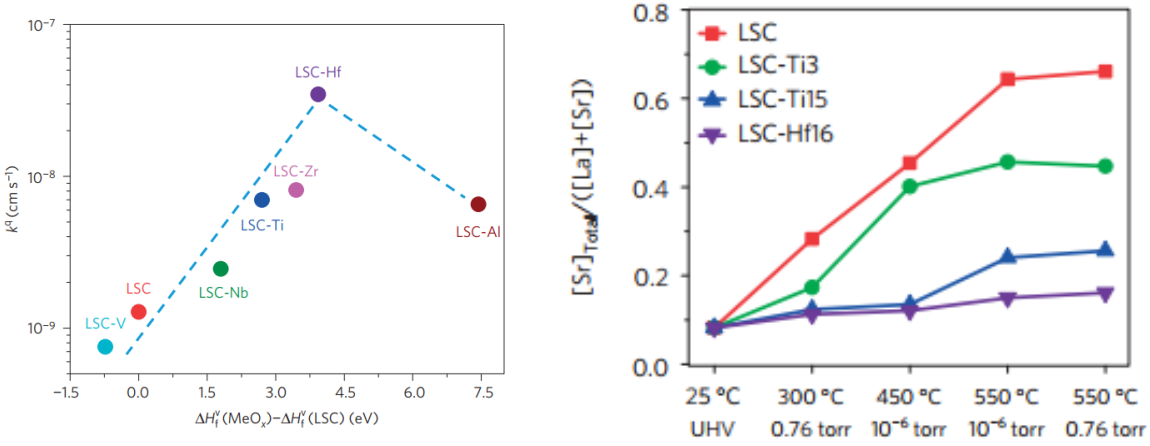

Figure 9. The a) volcano relationship between reducibility and the surface exchange coefficient and b) the increase in surface strontium for varying infiltrated cations[36].

2.4.2 Electrically Conductive Infiltrates

There are two main material groups under the auspices of electrically conductive infiltration. The first is infiltration of mixed ionic electronic conductors that have high

electronic conductivity relative to the ionic conductivity, such as $Sm_{0.5}Sr_{0.5}CoO_{3-\delta}$ (SSC). The second modification strategy is through infiltration of noble metals.

Along the first direction, Lou et al infiltrated SSC on an LSCF backbone and showed decreasing polarization resistance with increasing concentration of the solution[37]. From the impedance spectra they determined that the infiltration enhanced the rate of oxygen reduction (high frequency arc) while the mass transfer (low frequency arc) stayed the same. Thus, only the surface properties were modified and not the bulk LSCF.

A thin film coating of LSM on LSCF is the prototypical example of nonintuitive properties of conformal surface coatings. LSM has more sluggish oxygen surface exchange kinetics due to lower concentration of oxygen vacancies and thus lower ionic conductivity, but possesses higher electronic conductivity as compared to LSCF[38]. Despite these poor surface exchange properties, Lynch et al found the polarization resistance of the cathode decreases when a thin film of LSM is deposited on LSCF as seen in Figure 10[39]. An important aspect of this experiment is that the initial resistance of the LSM-coated LSCF is slightly higher than the reference LSCF, but under bias, the polarization resistance is lower. When tested as a full cell, the performance continues to increase rather than degrade like the LSCF reference. Thus there are two benefits from the surface modification: a decrease in polarization resistance and a dramatic decrease in degradation rate. The authors ascribed the increasing performance over time to a consistent increase in vacancy concentration with increasing cathodic bias for LSM. Others have also reported on the enhanced performance of LSM thin films under bias and attributed the increased performance to atom rearrangement on the surface[40].

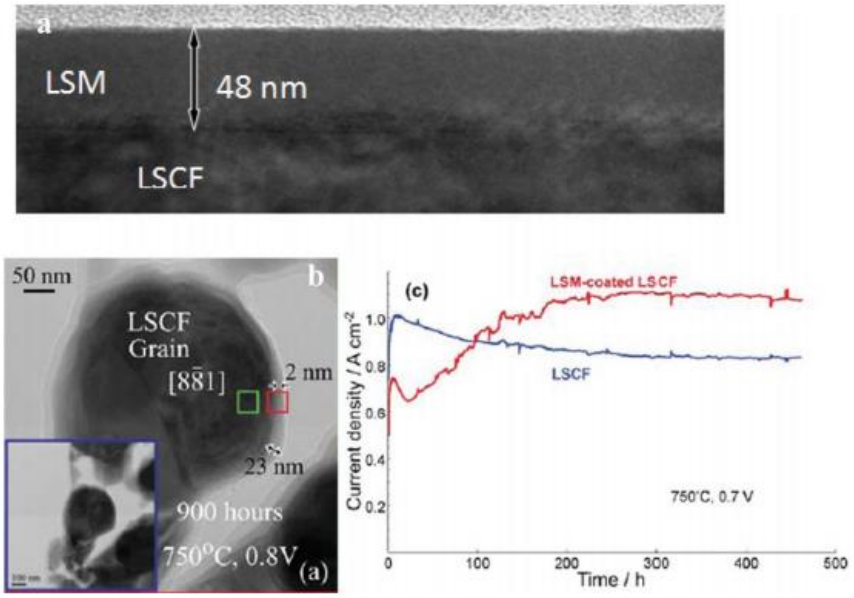

Figure 10. Above, (a) shows a cross section of a 48nm coating of LSM on a dense LSCF asymmetric cell; (b) a TEM micrograph of a porous LSCF cathode with a conformal coating of LSM; and (c) current density over time measurements for the blank and LSM-coated cathode [39]

Giuliano et al highlighted the importance of the cathode bone on the performance under bias[41]. The authors infiltrated LSM into LSCF and BSCF and performance EIS under OCV and a cathodic bias. Like Lynch, the authors found that LSM on LSCF resulted in a lower polarization resistance under a cathodic bias. However, for the BSCF, which exhibits higher ionic conductivity and bulk cathode performance, the polarization resistance increased under bias with the LSM infiltration. Using EIS to calculate chemical capacitance, they determined that the vacancy concentration in BSCF decrease under the bias, which is contrary to expectations based on LSCF literature.

Lee et al also showed that a thin partial layer of LSM on LSC can increase the surface exchange coefficient[42]. They postulated that the enhanced performance of the partial coverage film was due to the manganese substitution in the underlying LSC that

stabilized higher Sr concentration near the surface. The ideal film thickness was 0.9nm with decreasing performance for films thicker than 3nm. It demonstrates that even small modifications to the surface can yield large changes to performance and that interdiffusion between the backbone and coating can occur under operating conditions.

The second strategy for surface modification with electrically conductivity material is through infiltration of noble metals. Platinum and palladium are often infiltrated into sub-10 nm particles on the surface of the cathode. Uchida et al infiltrated platinum on an LSC-SDC composite cathode and saw a reduction in cathodic overpotential[43]. However, Simner et al incorporated platinum via several different ways into an LSF-SDC composite cathode and found no change in performance[44]. The null result for that work indicates that size is important for the platinum particles. The particles in Simner's work were presumably larger than Uchida based on the fabrication methods. Simner also looked into palladium dopants and found the larger particles were capable of decreasing polarization resistance by 50%, but also noticed some possible dissolution of the palladium nanoparticle into the host lattice that corresponded with a significant degradation rate. Others have also identified palladium entering the later of LSCF and $BaCeO_3$[45], [46]. In addition to doping into the lattice, which may or may not improve performance, it is also important to consider long term degradation beyond any initial performance enhancement because of coarsening at higher operating temperatures.

Precious metal surface decoration is a very common strategy in the broader chemical catalysis community. In purely chemical catalysis experiments, the increase in performance is ascribed to a metal support interaction and a change in local electronic structure. Therefore, in terms of infiltration with electronically conductive material,

precious metal catalysts influence the ORR activity not purely by the electrical activity, but by the change in local electronic structure.

2.4.3 Applications of Conformal Coatings

Advances in thin film deposition have allowed for unique thin film properties to be characterized in electrochemical applications. Surface modification with conformal thins have been demonstrated throughout the fuel cell components. In general, there are several major areas where ALD has been used: thin electrolyte layers, interfacial layers between electrode and electrolyte, protective layer for interconnects, and as anode and cathode catalysts[47]. The Prinz group has developed an ALD process for thin film SOFCs aimed at reducing the thickness of the electrolyte to 10's of nanometers. They have deposited electrolytes of yttria-stablized zirconia (YSZ) to create high performance cells with operating temperatures as low as 200-300°C. The free-standing Pt/YSZ/Pt fuel cells are on the order of 150 nm in total thickness with a peak power density of around 0.25 W/cm^2, which is significantly higher than sputtered YSZ films[48]. They have further increased performance to 677 mW/cm^2, 861 mW/cm^2 and 1.34 W/cm^2 at 400°C, 450°C and 500°C respectively for an ALD thin film SOFC with a high surface area corrugated electrolyte membrane [49], [50]. Besides limiting ohmic resistance by employing thin films, intrinsic ionic conductivity has been enhanced by an order of magnitude when the layer thickness is reduced from 70 to 17 nm[51]. At these small length scales, nanoionic effects may factor in to performance. However, it is important understand there are many confounding factors that can lead to inaccurate data such as the purity of testing set up materials, especially when testing thin films that may have high resistances[52], [53].

Brahim et al tried to enhance the electrochemical activity of the electrolyte-electrode interface by creating a gradual ionic to electronic composition using a ZrO_2 system doped with In_2O_3 to increase conductivity[54]. While no full cell tests were performed, impedance on the half cells showed an increase up to 65.2 mol% $InO_{1.5}$ and then a decrease up to 91.5 mol% indicating the ability to tune electrochemical behaviour using ALD and manipulate the doping concentration of the thin films. Chao et al tried to modify the surface in similar manner by depositing a 1 nm thick layer of 14-19 mol % YSZ on a YSZ pellet[55]. The 50% increase in performance was attributed to the higher oxygen vacancy concentration at the surface, which enhanced oxide ion incorporation. It also demonstrated the possible importance of vacancy concentration over ionic conductivity since 8 mol% YSZ has the highest ionic conductivity.

ALD has been used to apply thin coatings to active materials to enhance stability. Biener et al stabilized nanoporous gold with a 1 nm film of alumina and titania. The alumina coating stabilized the nanoporous gold up to 1000°C and the titania coating (which consisted of highly dispersed nanoparticles after annealing) showed a 3x catalytic enhancement of CO oxidation[56]. Gong, et al also used ALD to stabilize nanostructured $La_{0.6}Sr_{0.4}CoO_{3-d}$ in an SOFC cathode[57]. The conformal ZrO_2 films reduced the polarization area-specific resistance by a factor of 19 after 4,000 hours of testing. They claimed that the ZrO_2 coating had enough porosity for O_2 to access the LSC, but confined the growth of the LSC nanoparticles and suppressed surface Sr segregation, which is a known cause for LSC degradation. Also looking at the cathode, Kungas et al demonstrated that ALD of Al_2O_3 on an LSF-YSZ cathode causes an increase in electrode impedance that correlated to blocking of the active surface area[58]. Yu et al explored other surface

coatings by depositing ceria and strontium oxide on composite cathodes of YSZ-$La_{0.6}Sr_{0.4}CoO_{3-\delta}$ (LSC), YSZ-$La_{0.8}Sr_{0.2}FeO_{3-\delta}$ (LSF) and YSZ-$Ba_{0.5}Sr_{0.5}Co_{0.8}Fe_{0.2}O_{3-\delta}$ (BSCF)[59]. In this experiment, YSZ was used as the scaffold and the composite material was infiltrated after which the surfaces were coated via ALD. While the strontium oxide showed increasing polarization with increasing surface coverage (consistent with blocking of active sites), the ceria coating showed most of its increase in impedance after two ALD cycles. They suggest that the ceria interacts with the surface vacancies in the LSF and diminishes the O_2 adsorption process, which likely occurs at vacancy sites. They claimed that the higher electrode resistance for LSF when compared to the BSCF was due to the lower vacancy concentration in LSF relative to BSCF. These findings indicate the importance of surface functionalization on SOFC cathodes.

ALD also allows access to unique thin film properties. Crumlin et al found via in situ AP-XPS that thin films of $La_{1-x}Sr_xCoO_{3-\delta}$ showed strontium enrichment and decreased formation of secondary phases as compared to bulk pellets of LSC, especially at high temperatures[57]. The strontium enrichment was cited as the source of the enhanced catalytic activity. Chen et al found that praseodymium-doped ceria thin films (~150nm) had a greater deviation from stoichiometry as compared to the bulk due to a decrease in the enthalpy of reduction of ceria[58]. In another example, Chueh et al used ambient pressure XPS to determine a high concentration and stability of Ce^{3+} on the surface over a range of temperatures and oxygen partial pressures, which differs from the bulk behaviour[59]. The Ce^{3+} concentration also varied with temperature. At low temperatures, (~250°C), the surface and bulk concentrations were approximately equal. At higher temperatures (~650°C), there was as much as a two orders of magnitude increase in Ce^{3+} concentration,

which correlates to increased electrical conductivity and vacancy concentration, which is important in the gas-solid electrochemical interface[60]. Jose la O et al found a similar increase in vacancy concentration in LSC films as compared to bulk which contributed to dramatically enhanced ORR, but wasn't able to determine a cause for the increased vacancy concentration[61]. Gadre et al have shown an increase in ORR activity when $La_{0.2}Sr_{0.2}CoO_{3-\delta}$ and $(La_{0.5}Sr_{0.5})_2CoO_{4-\delta}$ are put in a heterostructure arrangement, there is a Sr enrichment in one phase driven by a chemical potential that increases vacancy concentration[62]. Han and Yildiz pointed to an interfacial strain that also facilitated the oxygen incorporation[63]. Even without a coating, the surface of the cathode can change during operation as evidenced by work showing change in surface segregation with cathodic bias[42], [43].

2.5 Technical Approaches

2.5.1 Electrochemical Impedance Spectroscopy

Electrochemical impedance spectroscopy is a widely-used technique in solid state electrochemistry to determine important features of the system. The electrochemical system responds to an applied sinusoidal current or voltage that results in a phase shift as

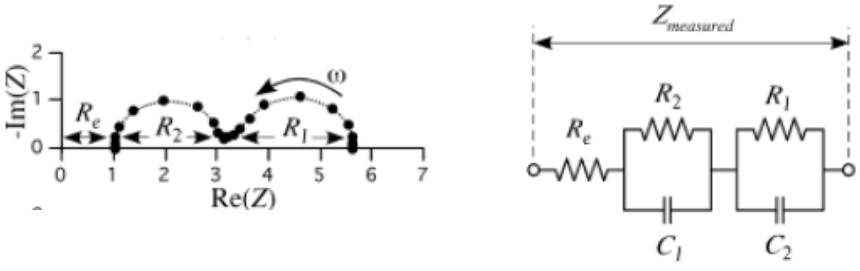

Figure 11. Examples of an impedances spectra and the accompanying RC circuit model.[60]

a function of frequency. The resulting spectra forms one or more distinct arcs that can be approximated by series and parallel circuit elements as demonstrated in Figure 11. The ohmic resistance is the first x-intercept and the polarization resistance is the difference between the first x-intercept and the final x-intercept at low frequencies. The major advantage of this technique is the ability to differentiate electrochemical steps based on characteristic time constants. In relatively straightforward cases, the recorded response is analyzed using equivalent circuits where charge transfer steps are modelled as resistors and charge polarization as capacitors. The data collected is typically reported in a Nyquist or Bode plot, which gives information about the resistance of that step as seen in Figure 12. A Nyquist plot does not explicitly show frequency information, but frequency decreases from left to right. In other words, high frequencies are to the left and low frequencies towards the right.

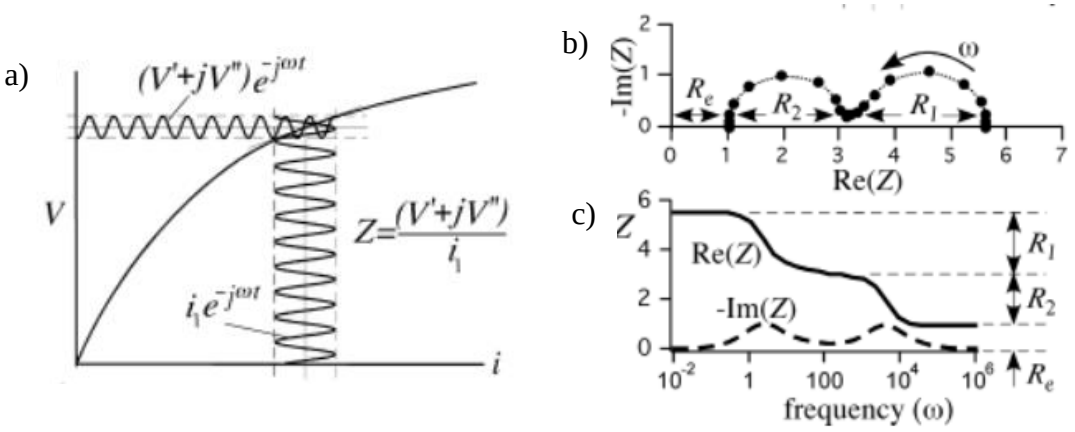

Figure 12. a) shows the small voltage perturbation and the resulting gain and phase shift, b) an example of an Nyquist plot with imaginary and real impedance as the y and x-axis respectively, and c) the corresponding Bode plot of impedance as a function of frequency [60].

In cases of mixed conductors, such as cathode materials like LSCF, both the surface activity and ambipolar diffusion through the bulk can co-limit the behavior resulting in

deviations from the ideal capacitive behavior. In this case, the perfect semicircle that is indicative of capacitive behavior becomes distorted at high frequencies due to diffusion limitations. Alder presents a review of the papers describing this behavior and describes the diffusion process as taking place on the surface as opposed to any dependence on diffusion through the film into the electrolyte[60]. In that same review, Alder describes the simple model derivation of the impedance for the co-limited case, which has been described in the cathode literature review and is shown in Figure 13[61]. Briefly, the model assumes a semi-infinite surface that has uniform surface coverage of the gas species that occurs via gas adsorption/desorption and surface diffusion. Then the surface equilibrium is perturbed at the origin by an electrochemical reaction by which the adsorbed species is consumed and there is a driving for species to move toward the vacated space. At steady-state, the increasing rate of adsorption due to the newly available surface area is balanced by the decreasing rate of diffusion due to the longer distanced that need to be covered. The resulting impedance shows a characteristic tear shape known as the Gerischer impedance as indicated in Figure 13 d). The spectra is reminiscent of a Warburg impedance, which is due to strictly diffusion, but varies from the Warburg's 45° behavior at high frequencies. For the Gerischer impedance, the characteristic time constant is proportional to $1/k$ (where k is the surface exchange coefficient) and the characteristic resistance is proportion to $1/\sqrt{kD}$ (where D is the diffusion coefficient). Fitting the impedance is often non-trivial as many circuit elements can be fit to a given spectra making any mechanistic determination

unclear. For further information about Gerischer impedance in the SOFC literature see several additional papers [24], [62].

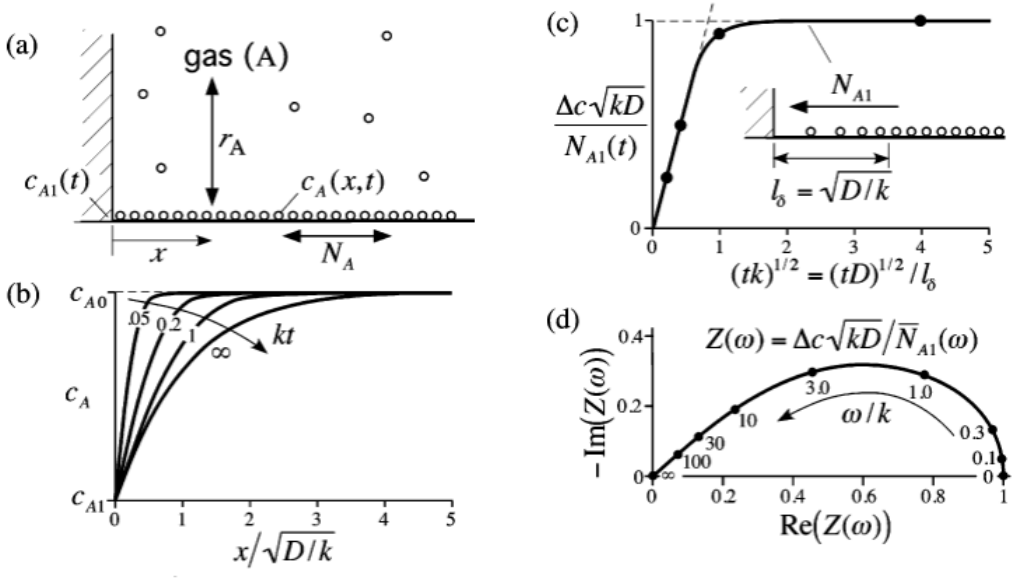

Figure 13. Several representative graphs for deriving Gerischer impedance response where a) shows a semi-infinite plane with a given equilibrium surface coverage, b) is the concentration profile about the origin, c) is the surface fulx as a function of time with the utilization length parameter, and d) the impedance spectra for surface flux species [61]

2.5.2 X-ray Photoelectron Spectroscopy (XPS)

X-ray photoelectron spectroscopy is a surface sensitive, S-ray absorption technology that aids in identifying oxidation state of materials. The penetration depth is typically 5-10 nm, which allows isolation of the top surface that is often most important in electrochemical reactions involving a gas phase. X-rays probe the electronic features of the surface species by ionizing core-level electrons. These core level electrons are then ejected

from the sample and the kinetic energy is measured using a hemispherical detector according to:

$$E_{binding} = E_{photon} - (E_{kinetic} + \emptyset) \qquad \textbf{Eq 24}$$

Where $E_{binding}$ is the binding energy of the electron, E_{photon} is the energy of the X-ray, $E_{kinetic}$ is the measured kinetic energy of the photoelectron and $\emptyset$ is work function, which a combination of the device and material work functions. For a given system, the work function is assumed to be constant. The X-rays in a lab scale unit are typically a single wavelength and generated by striking an aluminium target. The Thermo Scientific K-Alpha uses an Al Kα monochrometer with a 400 μm spot size. An example of the apparatus set up and XPS spectra are shown in Figure 14[63]. Interpretation of the XPS spectra can be challenging especially for cerium-based materials due to many closely space peaks. Further details relating to the fitting of cerium and praseodymium are discussed in later chapters.

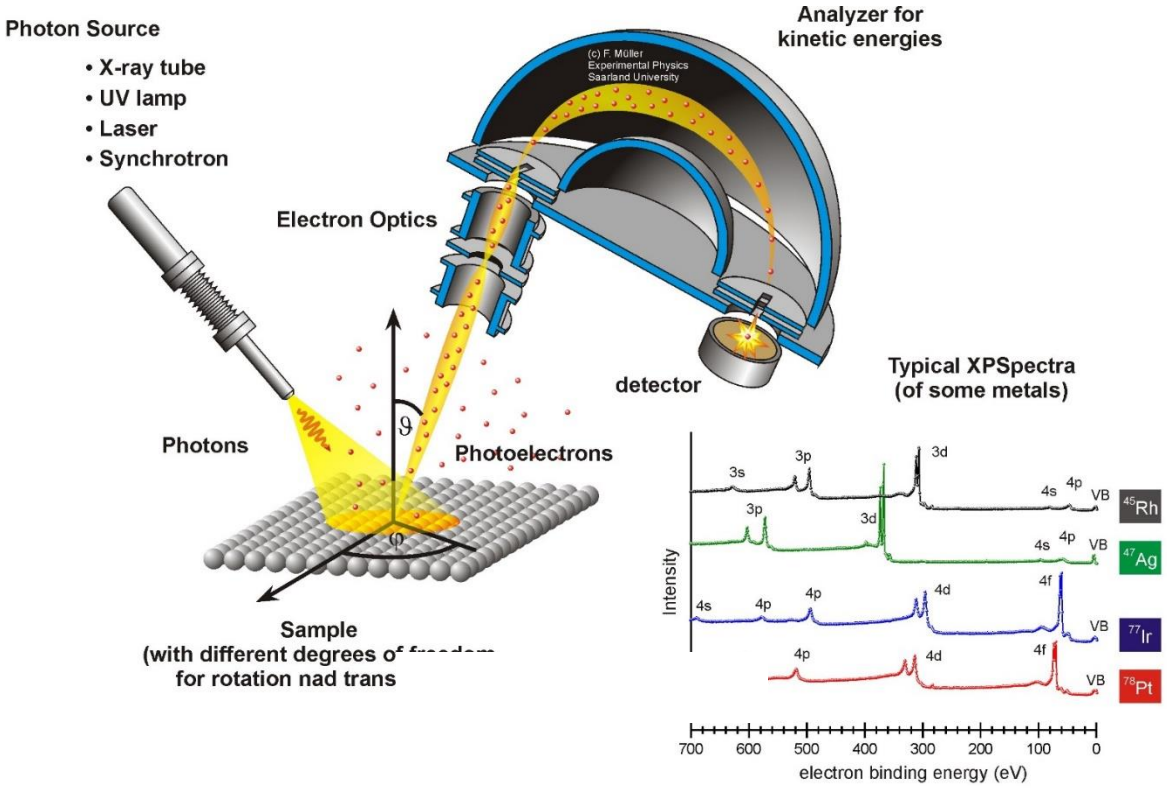

Figure 14. A schematic representing the major features of an XPS chamber including, photon source, hemispherical analyzer and an inset of example XPS spectra[63]**.**

CHAPTER 3. ASYMMETRIC CELL TESTING PLATFORM

The purpose of an asymmetric cell is to isolate the performance of the cathode with respect to the surface modification. It is difficult to conformally coat the tortuous porosity of a typical cathode. Since the impedance scales with surface area, asymmetric cells with a porous cathode on one side and a dense thin film of the same material on the other side will be limited by the impedance of the dense film. Thus, any increase or decrease in performance can be directly related to the surface modification of the film. The advantage in using an asymmetric cell testing set up is control of film thickness and morphology. For example, there may be multiple microstructural features of an infiltrated coating film that can be observed after testing. However, it is difficult to correlate a single feature from the range of microstructures to the performance increase. Analysis of the improvement relies on experience and representative morphological elements. With the asymmetric cell testing set up the film thickness can be accurately controlled as well as the surface area to triple phase boundary ratio. Additionally, physical deposition technique like sputtering allow for a larger range of films to be tested as compared to gas phase conformal coating techniques like ALD, which rely on a limited number of available precursors, or solution based techniques, which are more difficult to control in terms of thickness and conformality.

3.1 Electrolyte Supported Cell Fabrication

The electrolyte supports for the asymmetric cells were fabricated by dry pressing 0.35g of 20 mol% samarium doped ceria (SDC) purchased from Fuel Cell Materials. The powders were ball-milled in ethanol for 24 hours with 1 wt% polyvinylbutyral (PVB) binder. After drying, the powders were pressed in a 13 mm die to 5 tons. It was often

difficult to press complete pellets without cracking at the beginning. Several difference lubricants were tried including steric acid in acetone, graphite suspended in acetone and WD-40. All of these worked at varying levels of success, but without providing consistent uncracked pellets after pressing. The most important factor in prevent the cracking pellets was to avoid any powder from gathering between the inner die and the die wall. Sometimes putting scotch tape on the surface of the pellet combined with one of the lubricants would prevent the powder from accumulating between the inner die and the wall. However, it was found that powder would constantly fit around the die after pressing several pellets. The remedy was to press the pellets one time to 3-5 tons and then immediately grind up the pellets in a mortar and pestle until the small particles were reduced to powder again. After the re-pressing, there was very little powder evident between the inner die and die wall. It is important to clean two inner die pieces with a cotton swab and ethanol after each press to remove any powder remaining. It is likely the particle size of the powder was small enough to fit between the die and die wall. After pressing one time, the particles are larger aggregates that cannot fit as easily. The pellets were then fired according to the following furnace schedule:

Table 1. Firing Conditions for SDC Electrolyte

25°C to 500°C at 1°C/min	1 hour dwell
500°C to 800°C at 2°C/min	1 hour dwell
800°C to 1425°C at 3°C/min	5 hour dwell
1425°C to 25°C at 3°C/min	End

The electrolyte supports were greater than 95% dense according to Archimedes method. After firing, the pellets were polished using a MetPrep3 (Allied High Tech)

automatic polisher. They were mounted with Crystalbond to an aluminium puck heated to 240°C on a hot plate. The protocol in Table 2 was followed to polish the pellets.

Table 2. **Polishing protocol for electrolyte supports used in the pattern anode full cells.**

Polishing Compound	Force	Polishing Cloth	Platen RPM - Sample RPM – Direction - Time
Green Lube	9 N	Diamond Grid	350-150-contra-15secs
6 µm	9 N	Diamat	350-150-contra-1min
3 µm	9 N	Gold Label	350-150-contra-2min
3 µm	9 N	Gold Label	350-150-comp-2min
1 µm	4 N	White Label	350-150-contra-1min
1 µm	4 N	White Label	350-150-comp-1min
0.1 µm	4 N	Final A	350-150-contra-1min
0.1 µm	4 N	Final A	350-150-comp-1min

After polishing, the pucks were reheated and the cells were removed and rinsed with acetone to get rid of any residue from the Crystalbond. The cathode was then attached to the non-polished side of the electrolyte pellet. The LSCF cathodes were tape cast according to the protocol in Table 3. After mixing the first five ingredients, the slurry was ball milled for 12+ hours. Then the plasticizers were added and the slurry was ball milled again for 12+ hours. The final preparation step was adding the binder after which the slurry was ball milled again for 12+ hours.

Table 3. Protocol for making the tape cast slurry for the LSCF cathodes.

Adding Sequence		Mass/Vol	Component	Description
1		0.36g	Menhaden Fish Oil	Dispersant
2		10.00g	LSCF (Fuel Cell Material)	Powder
3		1.00g	Graphite	Pore Former
4		4 mL	Xylene	Solvent
5		4 mL	Ethanol	Solvent
After 12 hours of ball milling	6	0.66g	Polyalkylene Glycol	Plasticizer
	7	0.34g	Butyl Benzyl Phthalate	Plasticizer
After 12 additional hours of ball milling	8	0.62g	Polyvinyl Butyral	Binder

Right before casting, the slurries were degassed in a vacuum oven for 5-10 minutes to avoid formation of bubbles in the final tape and then immediately cast with a blade height of 50 μm. The tape was then let dry overnight and then the circular electrodes were cut out with a 6.35 mm punch. The LSCF tape-cast electrodes were adhered to the SDC electrolyte support using an SDC slurry. This buffer layer slurry was composed of SDC, V006 and acetone in a 1:4:20 ratio, respectively. The SDC used in this slurry was fabricated from the carbonate coprecipitation method to yield very small particle size. A smaller

particle size provides a larger driving force for sintering, which allows for dense interlayer between the SDC and the LSCF at 1100°C instead of a more typical 1400°C. The coprecipitated SDC was prepared from a 0.1 M solution of cerium and samarium nitrates in a 4:1 cation ratio. Briefly, 100mL of 0.1 M solution (16mL of 0.5M cerium nitrate + 8 mL of 0.25 samarium nitrate + 76 mL of deionized water) was added dropwise using a peristaltic pump into a 200-mL solution of 1.5812g of NH_4HCO_3 in deionized water to maintain a ratio of 2 mols of carbonate to 1 mol of cations. The resulting precipitate was centrifuged at 6000 RPM for 3 minutes and then centrifuged again with deionized water and two round of ethanol. After drying at 70°C for 12 hours, the powder was calcined at 650°C for 2 hours. The powder was then ball milled in acetone with V006 for 24 hours. It was found that adding an additional 2 wt% of Triton X-100 to the buffer solution yielded more uniform buffer layers and kept the SDC particles suspended for longer periods of time. Once the slurry was well mixed, 30 μL of the buffer solution was dropped onto the SDC electrolyte pellet. After approximately 10 minutes of drying at room temperature, the LSCF tape cast circle was pressed on to the center of the pellet with a cotton swab. The cells were then placed in a drying oven at 80°C for 2 hours and were then fired to 1080°C for 2 hours with a one-hour burnout at 400°C. A cross-section SEM is show in Figure 15. The top part of the SEM shows the porous LSCF cathode that was used as a counter electrode in the asymmetric cell testing set up. The thickness of the LSCF was approximately 50 μm. The SEM also shows a cross-section of the dense SDC electrolyte that was used as the support for the asymmetric testing set up.

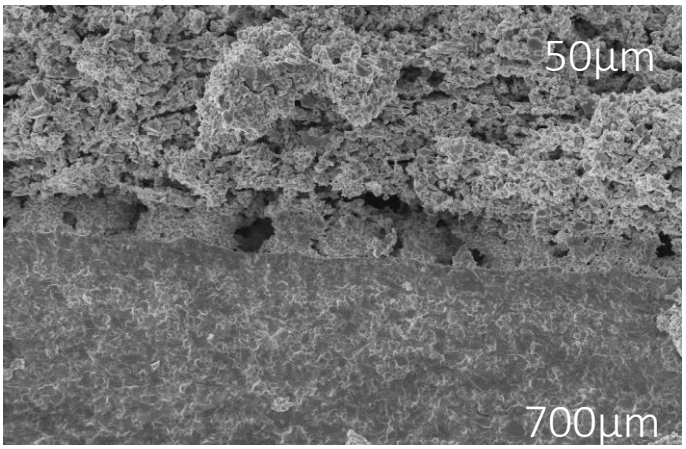

Figure 15. A cross section showing the dense electrolyte support and the porous LSCF cathode.

Similar to the asymmetric cells, symmetric cells allow for isolation of the effects of just the electrode of interest. Instead of a full cell with both a cathode and anode, a symmetric cathode cell has two identical cathodes that are fabricated on either side of an electrolyte support. This not only simplifies the data analysis, but also rules out any performance losses due to improper sealing, which is a difficult part of full cell testing. For the fabrication of the symmetric cells used in this dissertation, SDC was used as the electrolyte and the cathodes were fabricated via a tape casting method just described. The symmetric cell consisted of two porous cathodes of the same type as shown in Figure 15. The symmetric cells were tested in a compression set up consisting of a multi-bore alumina tube, springs and small diameter tubes. A silver electrode was compressed against the cathode with an SDC pellet as a spacer between the compression rod and the silver wire.

3.2 RF Sputtering

Sputtering is a thin film deposition technique that requires the ionization of a process gas (typically argon) and subsequent impact of that ionized gas on the surface of target material. The plasma is generated by applying a potential between a between the target

(cathode) and the substrate (anode) in a low pressure chamber with deposition pressures on the order of 10^{-3} mbar. The positively charged ionized argon atoms are driven to the target and transfers their momentum into the atoms on the surface, which in turn are ejected towards the substrate. While just about any solid material can be sputtered, the power source required depends on the electrical conductivity of the target material. For highly conductive materials, the voltage is applied using a DC power source. For less conductive materials, an RF power supply is required. The RF voltage induces a voltage via capacitive coupling through the target without any charge accumulation. Typically, RF sputtering shows much lower deposition rates, but allows for thin film deposition of non-conductive oxides. To increase the deposition rate, a magnetron source can be used in conjunction with either an RF or DC power supply. The magnetic field can trap the free electrons to a confined area above the target which performs two functions. First it lowers the amount of electrons that bombard the surface, which results in heating of the sample. Second, it increases the probability of the electron ionizing a neutral argon gas molecule that will then strike the target.

The sputtering set up used in this dissertation consisted of a home-built deposition chamber with two DC power supplies and one RF power supply. The set-up is shown in Figure 16. The system has a rough pump and turbo pump capable of pumping the interior chamber down to 10^{-7} mbar. After pumping down, the argon gas is flown in via mass flow controllers with a manual butterfly valve before the turbo pump that allows for modulation of the working pressure in the deposition chamber.

Figure 16 The sputtering system used in this dissertation showing the stainless-steel chamber, the interior of the chamber with heating stage installed, and the argon gas inlets on the top.

RF sputtering from a dense LSCF target was used to deposit a uniform thin film on the polished side of the SDC electrolyte support. The parameters for sputtering were guided by previous work by Lee et al in preparing dense LSCF films[64]. The LSCF target was fabricated from commercial powder (Fuel Cell Materials) by die pressing in a 32 mm die to 15 tons followed by sintering to 1325°C for 5 hours. The pressure and sputtering power were varied to identify optimal coating parameters.

There were significant challenges while optimizing deposition parameters. During RF sputtering runs with 20W power, the LSCF target was prone to cracking during the deposition resulting in unusually low deposition rates. Several changes were made to try to reduce the cracking of the target, which is shown in Figure 17. The target would often crack where the magnets in the sputtering source focused the plasma. The target would crumble under very small force after removal from the holder. Much of the following efforts to fix the problem were guided by discussions with the AJA International Technical Staff. The primary issues of concern were thermal management and stresses in the target

clamping assembly. The target can be elevated to temperatures on the order of 100°C under bombardment by the argon plasma. With metallic targets, the heat is conducted away quickly usually through an additional copper backing plate that physically touches the sputtering source gun. The copper plate is indirectly cooled by water flowing on the other side of the sputtering source gun. To increase the quality of the contact between the flat copper plate and the sputtering source, a copper mesh was placed in between, as advised by AJA. While this probably increased the heat transfer for the LSCF target, the problem with the target cracking continued. The recommendation for thickness of an arbitrary target is 0.125 inches for the ST-10 1-inch diameter sources. In depositions of nickel, it was found that a target of 0.125 inches was actually too thick to spark a plasma. This is most likely due to the ferromagnetic nature of nickel that influences how the magnetic field looks on the other side of the nickel target that is exposed to the argon gas. Polishing the nickel target to smaller than 0.100 inches allowed for easy sparking of the plasma and consistent deposition. Thinner LSCF targets were fabricated to test the thickness hypothesis but the same cracking phenomena occurred. Another possible explanation for the cracking was that the physical contact of the clamp created stress in the target, which was magnified at relatively higher temperatures due to thermal expansion mismatches. Since the fabricated targets are larger than the clamping diameter after sintering, the targets are polished down to a smaller diameter using 120 grit SiC paper. Sometimes the diameter of the target fits almost perfectly into the clamping ring with very little room for thermal expansion. To avoid clamping directly on the target, two strategies were implemented. For the first, the target was polished down to a smaller diameter so that it could physically fit through the clamping ring. It was then attached to the copper backing plate with silver quick-drying

ink so that it would be not fall out of the sputter-down arrangement as shown in Figure 18. This time the clamping ring would attach directly to the copper backing plate with the target sticking through the ring. Typically, the target is flush with the bottom of the clamping ring. However, this set up did not even allow for a plasma to be sparked. Instead of the expected deep purple plasma, there was a faint yellow glow, but no obvious signs of an argon plasma. It was unclear what the faint yellow glow was from, but there was what appeared to be a burn mark at one spot on the clamping ring near the target. A second configuration was fabricated in order to keep the target flush with the face of the clamp. In this arrangement, a thin disk (<.125") was cut from a solid copper rod and polished down on either side with 120 grit silicon carbide paper. Then a CNC was used to bore away the inside leaving a small lip around the perimeter. The lip would be the main contact point to the clamping ring. The LSCF target was polished to a smaller diameter as before and seated into the copper holder with quick drying silver ink. The surface of the target was flush with the top surface of the lip. This allowed the target to sit in the copper holder. In this case, the target was the same height or a little lower than the surface of the clamping ring. After several depositions with a cumulative sputtering time of >15 hours, the target showed resistance to cracking. This set up was used for the remainder of the sputtered films.

Figure 17. Cracking of LSCF targets during RF sputtering.

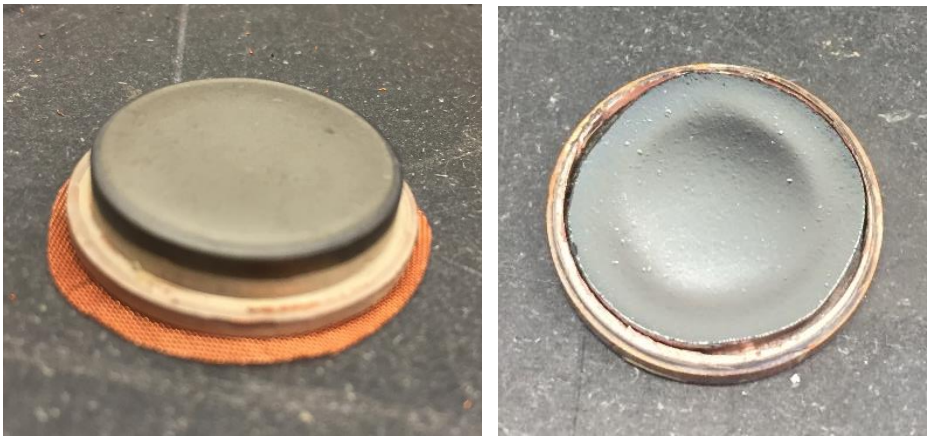

Figure 18. Two target holding set ups where a) the clamping ring pressed against the copper backing plate and b) the clamping ring pressed against the lip of a copper target holder. The copper holder with the small lip was the optimal set up to avoid cracking of the LSCF target.

In addition to the new testing setup, the power source for the sputtering gun was ramped slowly prior to deposition and after deposition was completed. It was recommended that the slow ramping of the power be done each run, but especially the first deposition for a new target. The break-in procedure reduces any internal stress from the high temperature sintering as well as removing any surface contamination. It also prevents large thermal fluctuations that may be present from quick ramping to full power. This was vital to keeping the LSCF target intact for multiple depositions, but was also used for the ceria and doped ceria targets.

At the beginning of each deposition, the chamber was pumped down to a pressure of less than 5 E-5 mbar and then backfilled with argon up to 8E-3 mbar. The plasma for the RF sputtering target was ignited with the help of a secondary sputtering source in the same chamber. This helper plasma was a DC sputtering source with a metal target that would readily spark on its own. Being adjacent to the RF with a small power applied allowed for easy lighting for the RF plasma. The recommended pressure for sparking the RF without a

helper plasma was on the order of 4E-2 mbar according to conversations with AJA International. In other sputtering set-ups the helper plasma it is not necessary. However, achieving the higher pressures needed to spark an RF plasma on its own would tax the turbo pump in the current configuration. After the plasma was ignited at the low pressures, the flow rate of the argon was increased to 60 sccm over the course of one to two minutes to minimize any thermal stresses created by the increasing bombardment of ions and electrons. After reaching the working pressure of 1.6E-2 mbar, the RF power was slowly ramped over the course of one to two minutes to the desired output. For the LSCF targets, the deposition power was kept at 15W. The 15 Watts on the 1-inch target provides a power density of $3W/cm^2$, which is the recommended deposition power for ceramic targets by the Kurt J. Lesker company[65]. It was found that higher powers for that target led to more cracking. For the ceria targets, the deposition power was 20W. The undoped and doped ceria target were relatively more robust, but there were still a few targets that cracked after 20W depositions.

3.3 Morphology Upon Deposition and Post-Testing

The RF sputtering produced a dense, uniformly thick LSCF film. Figure 19 a) shows a cross section of the film deposited on a silicon wafer with indicators of thickness. As shown, the film was conformal and showed no obvious columnar morphology that is more typical of films deposited via PLD. The film was uniform across the width of the silicon wafer piece. Visual inspection of the sample plate after the deposition showed uniform material deposition in a circle approximately 3-4 inches in diameter. Practically, that means up to six samples could be deposited at a given time. Because there is so much variability

in the nature of the nanometer-level fabrication procedure, samples from the same batch were compared for performance increases.

A top down view of the deposited film shows the small grains on the order of a few microns as seen in Figure 19 b). There were some small pinholes noticed infrequently in the film but the vast majority of the top surface initially appears to be dense LSCF film as deposited. It is important to recognize that there not all thin film deposition techniques result in identical morphologies. Simrick et al used pulsed laser deposition (PLD) to deposit thin films of LSCF and found very small grains that changed in morphology from sharp to rounded particles after high temperature testing[66]. With PLD, the deposition temperature is typically on the order of 600°C, which can lead to different initial and final microstructures as compared to the room temperature deposition of sputtering in this work. In much of the thin film work, the beginning and ending morphology are not always pictured. There exists substantial variation in electrochemical performance metrics with varying LSCF thin film setups, which could be due to minor differences in grain size or change in morphology that occurs under testing conditions. The effects of those minor differences on performance are not well studied. Adding to that variability is the fact that thin films degrade much more quickly than porous cathodes. In general, the greater degradation rate can be explained by the surface sensitivity of the experimental set up and the small amount of material deposited. Thus, any minor change in performance are magnified.

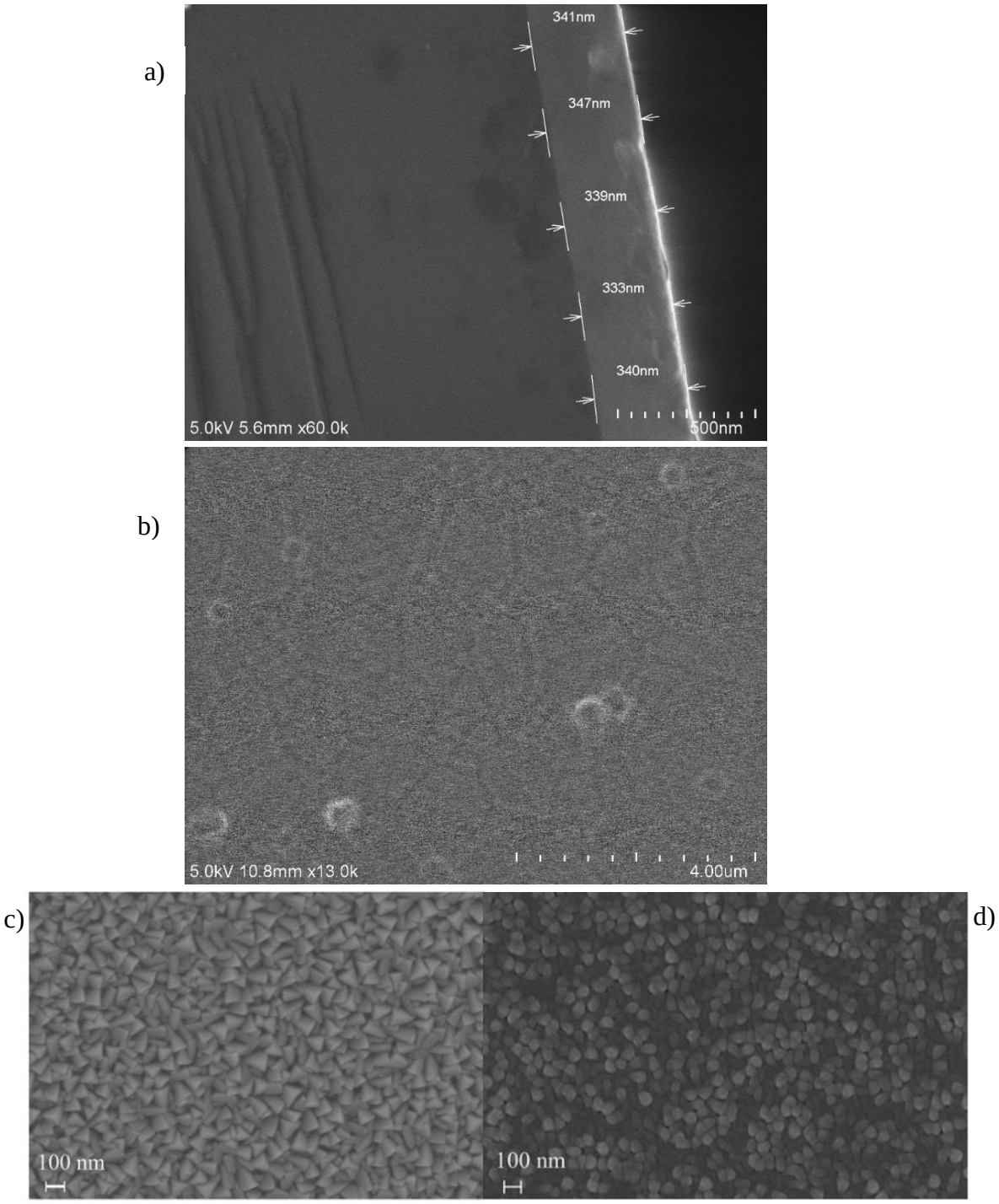

Figure 19. The as-deposited LSCF film shown as a) cross section, b) top-down view before testing. Compare those images to the PLD films by Simrick with c) top-down view as-deposited and d) a top-down view after EIS testing[66].

Previous LSCF deposition suggested a two hour anneal at 800°C after deposition, which is common in many RF sputtering experiments[67]. Often annealing the film is required for film homogeneity since the physical deposition technique could give rise to uneven distribution of elements from the target. It was found that annealing 800°C for two hours resulted in cracking of the film as shown in Figure 20. The cracking in the film is obviously undesirable. In terms of characterizing the ORR activity, the non-uniform surface makes comparison between samples more difficult. It was determined that the ramping rate of 3°C/min for both heating and cooling was too fast and contributed to the cracking. Samples that were heated and cooled at a rate of 1°C/min did not exhibit any cracking even after 100+ hours of testing and thermal cycling between 25-750°C. For the electrochemical data described in this work, the films were mounted in the testing set up after deposition and heated at 1°C/min to 750°C to do an *in situ* anneal. The annealing manifested itself in an equilibration time necessary for consistent EIS spectra.

a) 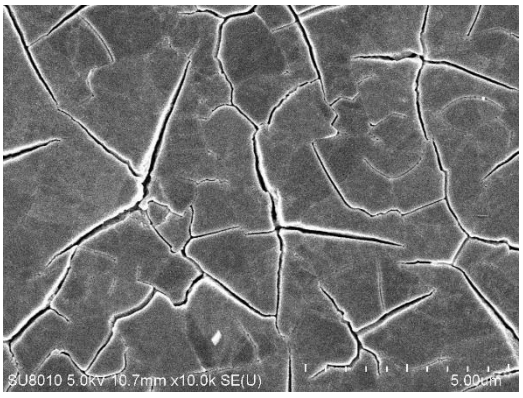 b) 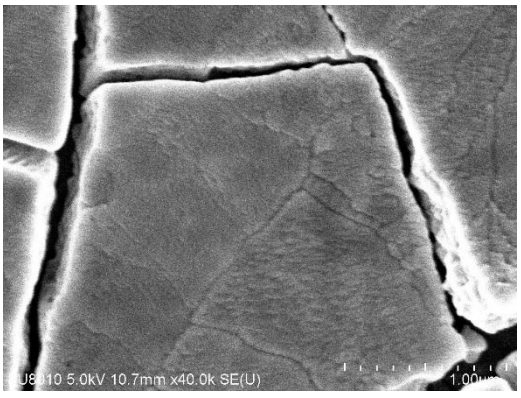

Figure 20. A top-down SEM image taken of the LSCF film after a) annealing to 800°C for two hours and b) zoomed in further after cell testing.

3.4 Electrochemical Characterization

As with any electrochemical measurement, it is important to make electrode connections are not influencing the impedance spectra. Two different current collectors were compared during this work. The first was ring of silver paste along the outer surface of the LSCF film, as shown in Figure 21 a). In practice, the silver paste was applied around the entire circle. Then a small silver wire was twisted together and bent in a circle and attached to the silver paste. The silver paste was applied around the edges of the dense LSCF film to avoid overlapping with the porous LSCF cathode used as the reference electrode. Thus, the electrochemically active area of the dense LSCF working electrode was not covered by any of the paste. The second electrode connection relied on a silver mesh as the current collector. In this set up, silver wire was wound into a circle and flattened between two metal blocks and then adhered to a YSZ or SDC dense pellet with silver paste. This allowed for an easy connection to the silver wire that would connect to the leads of the EIS. The mesh was placed between the silver wire and the dense LSCF film and held in place using a compression testing set up show in Figure 22. The

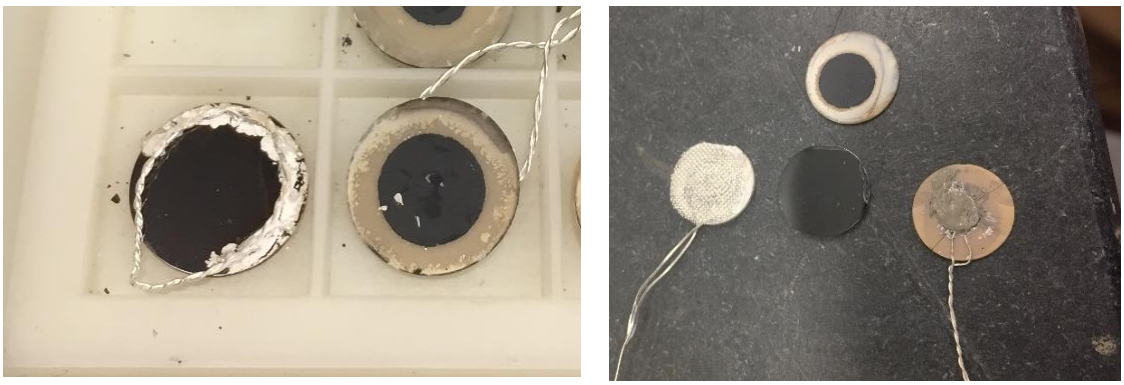

Figure 21. The top and bottom view of the asymmetric cathode with a) silver paste and silver connecting wires and with b) silver mesh on the polished LSCF with silver paste on the porous LSCF electrode.

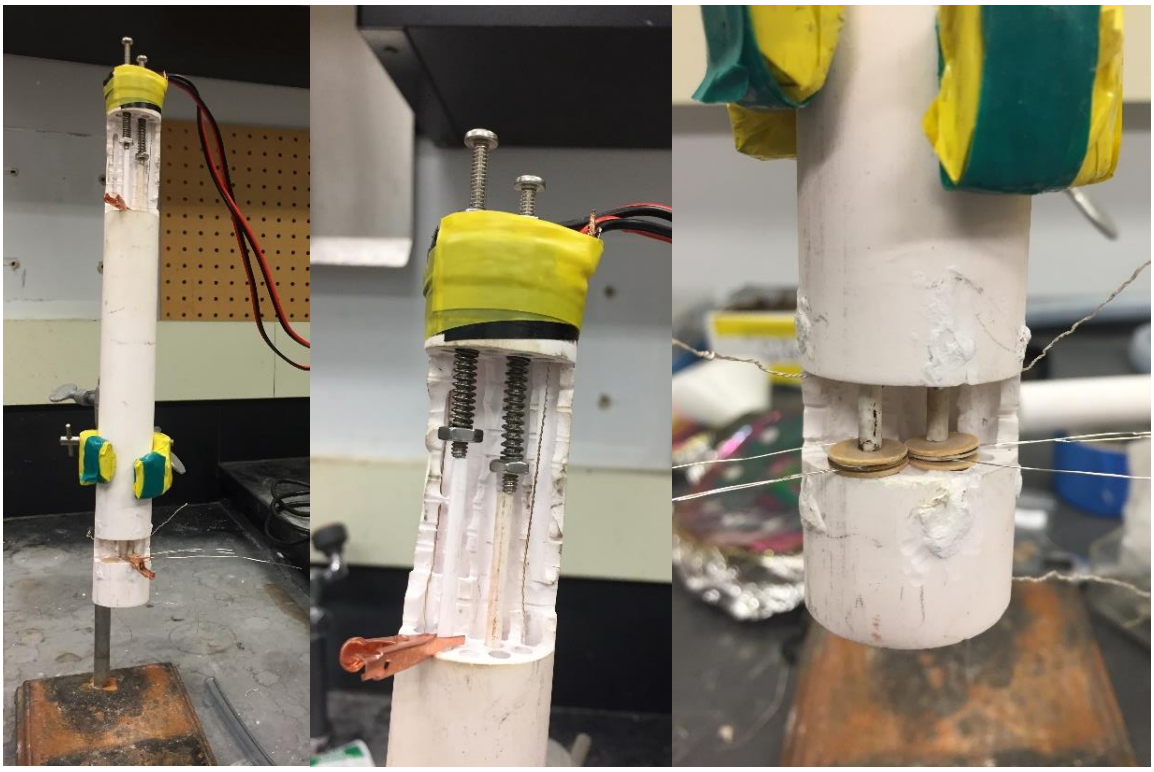

Figure 22. Compression testing setup for asymmetric and symmetric cells.

compression came from the springs that would press up against small alumina tubes. The pressure was enough to prevent the cells from moving, but care had to be taken to prevent the cells from cracking under too much pressure. If the atmosphere needed to be controlled, the set up was placed in a quartz tube with a silicone stopper containing an inlet and outlet small bore alumina tube.

The purpose of the asymmetric cell configuration is to create a dense film that dominates the polarization resistance. Thus, it is important to have a counter electrode with very small impedance so that any changes in the impedance spectra are directly correlated with the working electrode. In thin film experiments, there are several choices for the counter electrode. It is common to simply paint on silver or platinum paste on the opposite

side of the electrode. However, using a paste as the counter electrode can create some errors in the data collected. Adler demonstrated through numerical calculations that differences in the electrode kinetics can cause distortion of the impedance including frequency dispersion[68]. To mitigate dispersion due to differing electrode kinetics, a porous LSCF counter electrode was used. Because it is the same material and theoretical has the same kinetics, there should be minimum impact on the impedance spectra. Figure 23 shows a comparison between the asymmetric cell impedance and a symmetric cell of porous LSCF. The symmetric porous LSCF cell shows a much smaller impedance that is barely visible on the scale of the dense film LSCF. Thus, the impedance spectra for the asymmetric cell testing set up is dominated by the dense film.

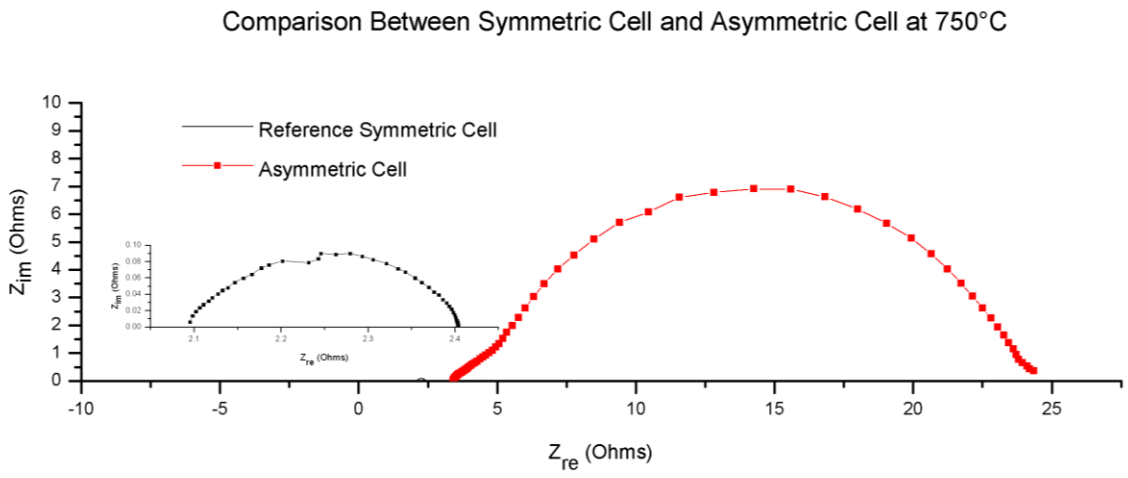

Figure 23. Comparison of the impedance spectra for the LSCF dense film and a symmetric cell with two porous LSCF cathodes at 750°C. The inset graph is an enlarged view of the impedance of the symmetric cell, which is hardly visible on the scale of the dense film impedance.

Figure 24 shows the impedance spectra on two different samples that were fabricated under the same conditions. The only difference between the two is the current collector,

which were tested as previously described. There are several important observations that can be drawn from the figure. First, the spectra show identical features with a small variation in the magnitude. Thus, we can be confident they are capturing the same behavior. Second, the difference in magnitude of the two arcs corresponds to scatter in the experimental data. The difference in the x-intercept is determined by the thickness of the pellet used, so slightly thicker electrolytes will haves slightly larger resistance before any normalized conductivity values are calculated. While the difference in the magnitude of the polarization resistance between these two samples appears large, the differences due to the coatings vary the polarization by an order of magnitude. When taking experimental measurements of thin films, even slightly changes in the surface morphology can influence the electrochemical behavior.

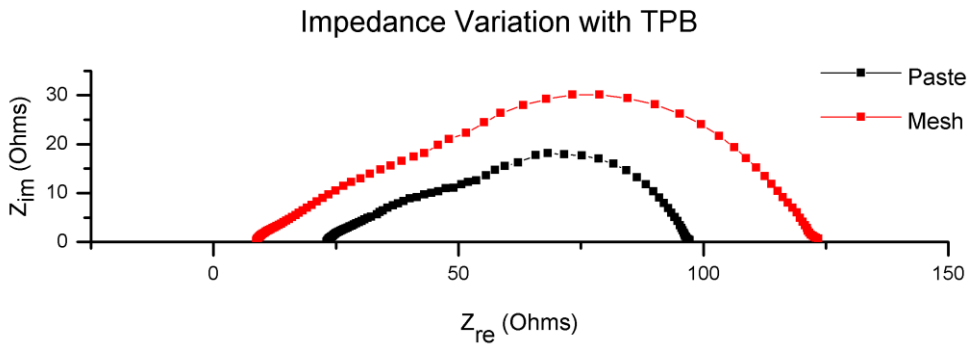

Figure 24. EIS spectra taken on two samples fabricated under the same conditions with the only change being the type of current collector used.

After confirming the current collection is not contributing to the collected data, it is necessary to confirm that the impedance arc is a measurement of the oxygen reduction reaction occurring on the surface and not due to a bulk film feature. One way to confirm that the surface is the prominent feature is to vary the partial pressure of oxygen. The bulk ionic conductivity should not be affected by small variations in the oxygen partial pressure.

The oxygen reduction reaction varies directly on the partial pressure of oxygen[69]. Impedance spectra collected in several different oxygen partial pressures are shown in Figure 25.

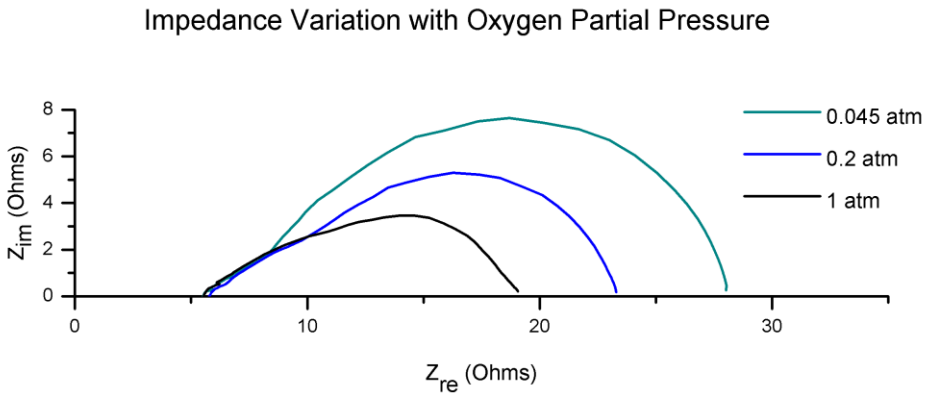

Figure 25. Impedance spectra collected at varying oxygen partial pressures showing the defining characteristic of the spectra is due to the oxygen reduction reaction activity.

The plot demonstrates that the main impedance arc at lower frequencies is dependent on the partial pressure of oxygen. Thus, the dominant contribution to the impedance spectra is the oxygen reduction reaction on the surface. This matches previous continuum models developed for mixed conducting films that suggest the low frequency impedance arc is associated with the oxygen reduction reaction and smaller impedance arcs at higher frequencies correspond to mass transfer between the cathode and electrolyte[70].

The samples were typically annealed operando at 750°C for 3-4 hours or until the impedance spectra was not changing after consecutive 60-minute intervals. Interestingly, the impedance of the thin film cells showed a low impedance upon reaching 750°C that would approximately double by the time the impedance spectra had equilibrated. Other thin films deposited via physical deposition methods have shown a transition from amorphous to crystalline between 450-600°C[71]. While this may indicate amorphous films as a method to improve conductivity for low temperature solid oxide fuel cells, the reason for the initial low impedance was not further investigated.

For thin film experiments, it is important to justify the testing set up is in fact probing the reaction instead of a bulk phenomena. It is well known that thin films may be influenced by sheet resistance, which can dominate the impedance spectra or cause erroneous conclusions to be drawn[53], [70], [72], [73]. One way to make sure that the impedance of the asymmetric cell is controlled by the surface and not bulk diffusion through the thin film is to vary the thickness. If the polarization resistance does not change with the film thickness, then the EIS spectra can be attributed to the surface ORR processes. To test this several different film thicknesses were used varying from 200-700 nm.

The thickness of the LSCF film is a significant consideration when characterizing material properties. It is important for the total thickness to be smaller than the characteristic thickness, which is the value at which the bulk diffusion pathway is dominant over the surface exchange pathway. This characteristic thickness (L_C) is defined as

$$L_C = \frac{D^*}{k^*} \qquad \textbf{Eq 25}$$

Where $D^*$is the oxygen self-diffusion coefficient and k is the surface exchange coefficient. For mixed conducting perovskites, the characteristic thickness on the order of ~100μm[74]. Thus, it is unlikely for thin film experiments to be approaching that limitation. That being said, how the current is collected is an important feature specifically for thin film electrochemical measurements. As previously mentioned, both a mesh and a silver wire/paste configuration were tested and showed the same electrochemical phenomena. The conclusion that the mesh and silver paste give the same electrochemical impedance is most likely due to the high electrical conductivity of the LSCF backbone. In this testing setup, there does not seem to be a need for the typical photolithography of the current collector. For the case of just the thin film cathode (i.e. without surface modification), previous numerical simulations have shown the requirement for closely spaced current collectors[75].

The impedance spectra for LSCF thin films of varying thicknesses are shown in Figure 26. The plot shows that the polarization resistance decreases with increasing film thickness until about 450 nm. Thicker films showed no further increase in polarization resistance. One explanation for this is that the film is limited by a contribution from sheet resistance. The interesting aspect is that the general shape of the EIS spectra does not change much over the range of thicknesses, so perhaps the effective sheet resistance is exhibited by both the ionic and electronic charges carriers and thus manifests itself as part of the mixed bulk/surface reaction. One unusual feature of the plot is the difference in slope

for the 376 nm film (0.93 eV vs ~0.73eV for other lines). It is expected that the activation energy should around 1-1.5 eV. One possibility for the lower activation energy is due to the multiple processes occurring in the impedance of the thin film in this work. As described in Figure 24, there are several features to the impedance with the main arc at low frequencies attributed to the ORR. The change in the total polarization will be a sum of the changes of each individual process. If the two smaller processes that occur at higher frequencies change less with temperature, the overall polarization behavior will change less with temperature. Smaller changes of polarization with temperature correspond to a smaller slope in the Arrhenius plot and thus a lower activation energy. Thus, the lower apparent activation energy can be attributed to sum of the behavior and will underestimate the ORR specific activation energy.

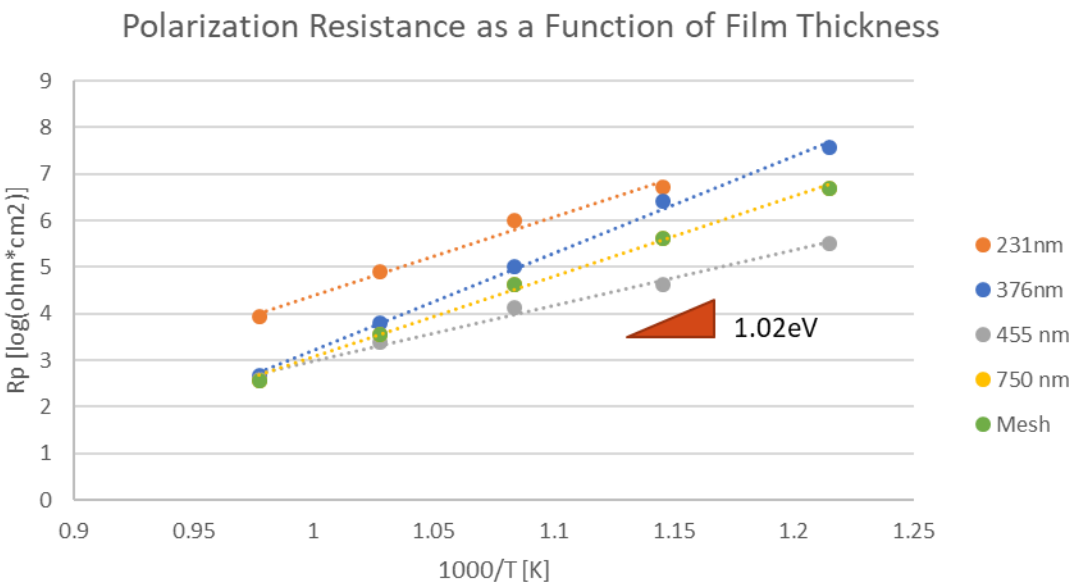

Figure 26. Polarization resistance values for LSCF film ranging in thickness from 321-750 nm.

As will be described in the subsequent chapter, the as deposited LSCF film was not completely dense. The TEM images presented in the next chapter show that the porosity was well distributed throughout the thickness of the film. This porosity could have also played a role in the change in polarization resistance observed with changing thickness. The amount of connected porosity could have decreased with increasing film thickness which would manifest in a larger observed impedance. Additionally, the decreasing polarization resistance with increasing thickness up to ~450 nm could also be explained by the increase in surface area of the nano-porous LSCF cathode.

CHAPTER 4. CERIA COATINGS ON LSCF CATHODES

4.1 Overview of Chapter

As has been previously mentioned, past literature indicates that vacancy concentration is a direct predictor of SOFC cathode performance. However, few groups have controlled the vacancy concentration of the surface modification material directly. This chapter focuses on surface modification of an LSCF backbone through infiltration of symmetric cells and RF sputtering for conformal deposition on the asymmetric cell testing platform. Both undoped ceria and doped ceria are used to modify the surface of an LSCF cathode backbone. The scientific and technical objectives of this chapter are as follows:

- Understand the role of ionic conductivity of the material deposited on an LSCF backbone on performance by varying the doping concentration of samarium in ceria
- Correlate electrochemical performance with morphology of the surface modification material
- Use the asymmetric cell testing platform to identify the correlation between film thickness and polarization resistance for doped and undoped conformal films

4.2 Fabrication

The symmetric cells were fabricated similar to the asymmetric cell testing platform described in Electrolyte Supported Cell Fabrication in Chapter 2. The process will be described here briefly. First, approximately 0.35g of SDC with 1 wt% PVB binder was pressed to 335 MPa in a 13 mm die. This electrolyte support was then fired to 1450°C for 5 hours. A porous cathode fabricated via tape casting was attached to the electrolyte with

an SDC buffer layer. This buffer layer slurry used SDC powder fabricated through a co-precipitation method which results in a very small particle sizes. The high surface area of the powder provides a larger driving force for sintering, which allows for a dense SDC layer without having to expose the porous tape cast cathode to excessively high temperatures which would decrease the surface area and thus performance of the cathode. Approximately 30μL of the buffer layer slurry was dropped on the electrolyte support and let dry for approximately 10 minutes. The porous cathode was punched out from a tape fabricated according to the previously mentioned recipe and pressed onto the buffer layer using a cotton swab. After the cathode and buffer layer were applied to both sides of the electrolyte support, the pellets were fired to 1080°C for 2 hours.

For the infiltration of complex oxides, it is important that the resulting oxide is stoichiometric. The final composition can vary without the use of a proper chelating agent. Two different chelating agents were used to identify any differences in performance or morphology of the infiltrated coatings of undoped ceria. The first is glycine, which is a simple amino acid that can complex at the amine or hydroxyl ligands. The second is citric acid, which is a carboxylic acid that has four ligands to bind to metal ions in solution. For both cases, the cation to chelating agent molar ratio was held constant at 1:1. The polarization resistances for symmetric cells infiltrated with 0.03M undoped ceria on LSCF are shown in Figure 27. The polarization resistance does not depend on the chelating agent used.

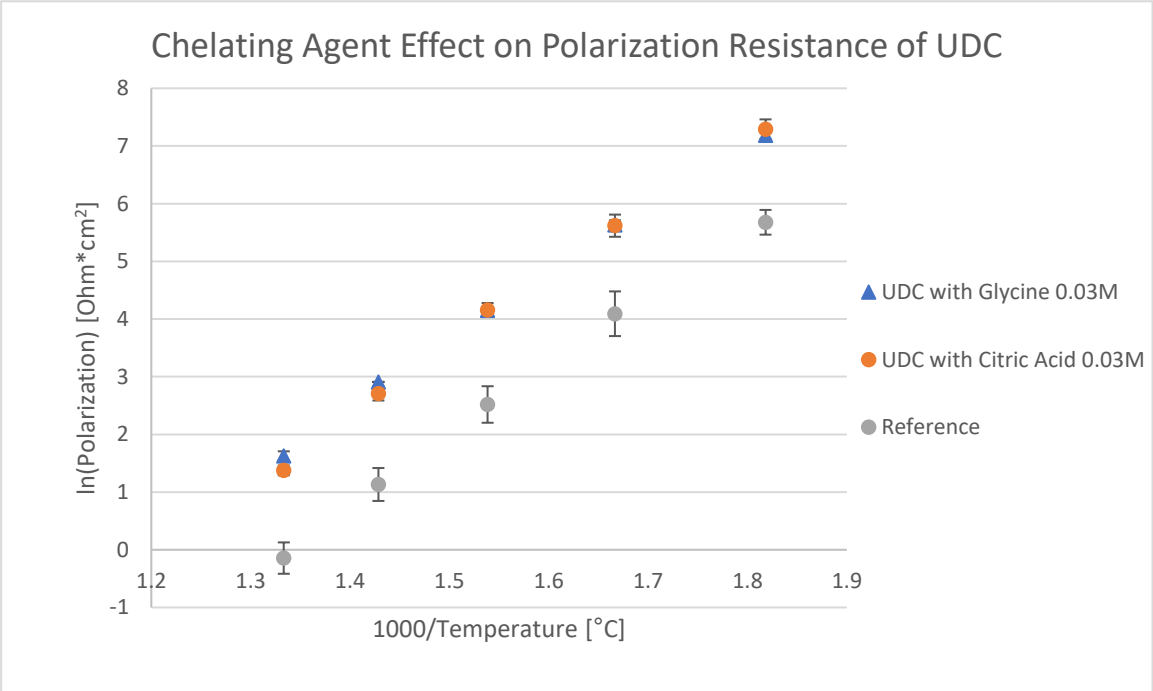

Figure 27. The effect of chelating agents on the polarization resistance of undoped ceria infiltrated on an LSCF backbone. The error bars indicated one standard deviation.

a)

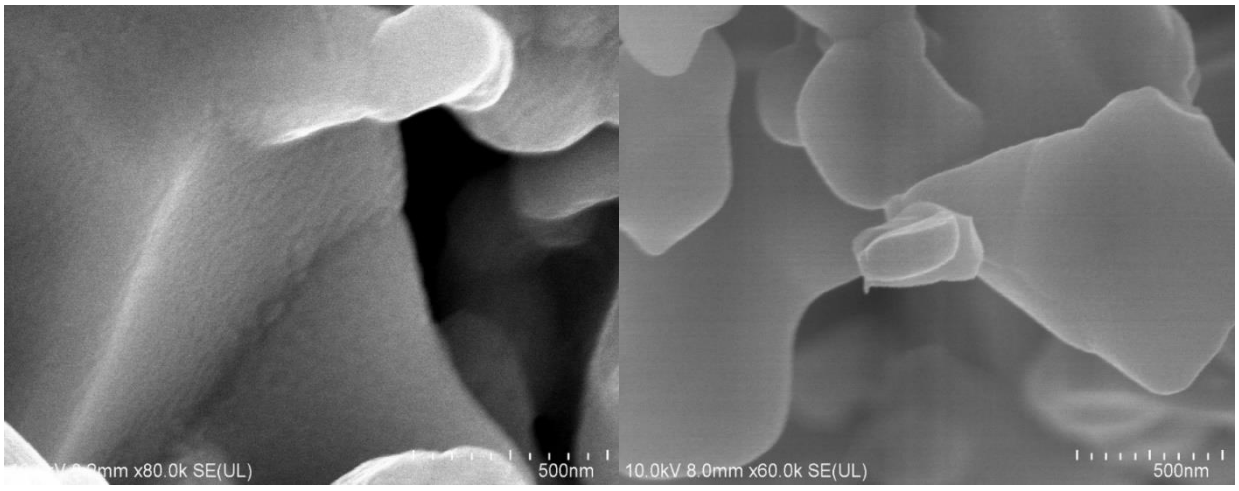

b)

Figure 28. SEM micrograph of the undoped ceria infiltration on the LSCF cathode backbone. The coatings are faint because of the small amount of material deposited and the excellent surface coverage.

It is expected that using citric acid will result in a homogenous coating, but the effect of the citric acid and glycine on the morphology is not obvious. The SEM images of the infiltrated solution after testing is shown in Figure 28. The top image a) shows the nearly conformal coating of the infiltrated solution with glycine. The ridges evident on the LSCF backbone indicate where the coating is present. The bottom image b) shows an SEM image of the infiltrated solution with citric acid. Although the surface morphology is not as clear as the top image, a similar morphology is hinted at.

4.3 Infiltration of Undoped Ceria Coatings on LSCF

In this section the LSCF cathode has been infiltrated with varying doping levels of samarium in ceria. It is anticipated that increasing the vacancy concentration of the infiltrate will increase the performance.

For the undoped ceria, four infiltration molarities were tested ranging from 0.3M to 1.0M. Above 1.0M the solution becomes more difficult to infiltrate as evidenced by the solution not visibly wicking into the porous LSCF. Even with vacuum infiltration, the solution does not always appear to fully integrate into the cathode backbone. Instead, a light precipitate forms on top of the cathode which, after firing, blocks some of the surface porosity. The effect of molarity on polarization resistance for a cathode symmetric cell is shown in Figure 29. The figure indicates two interesting behaviours. First, the 0.03M, 0.10M and 0.5M solutions all decrease performance to the same level. If ceria is acting as a physically blocking non-conformal layer, then the increasing the molarity should show progressively worse performance as more ceria is used to block the active surface sites.

Second, the polarization resistance of the 1.0M undoped ceria solution is not only lower than the previous concentrations, but also lower than the reference cathode.

The morphology for the infiltrated undoped ceria is shown in Figure 30 with increasing molarity of the infiltration solution from top to bottom. As the concentration is increased, there is a morphology change from sparse island (0.03M) to a slightly more connected network of islands (0.10M, 0.50M) to nearly conformal coverage (1.0M). This suggests that a conformal film of ceria may be more beneficial to performance than the higher surface islands, which goes against conventional wisdom. In most cases, performance increase is attributed to increasing the surface area and increasing the availability of sites for the ORR to occur.

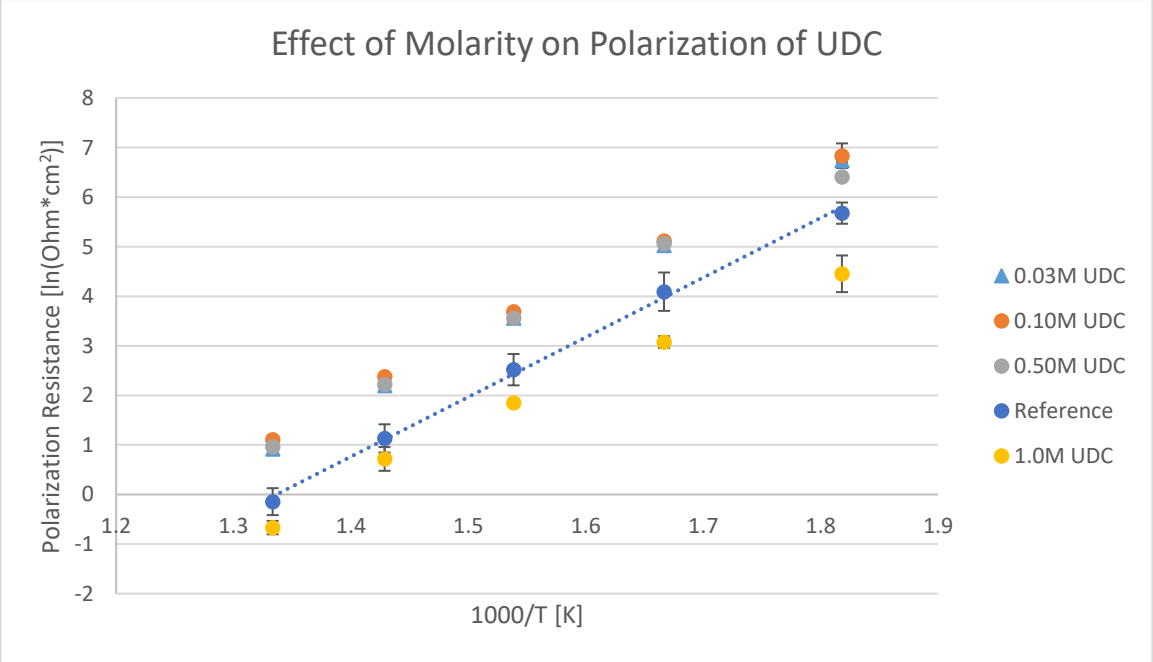

Figure 29. Polarization resistance for infiltrated undoped ceria of varying molarities.

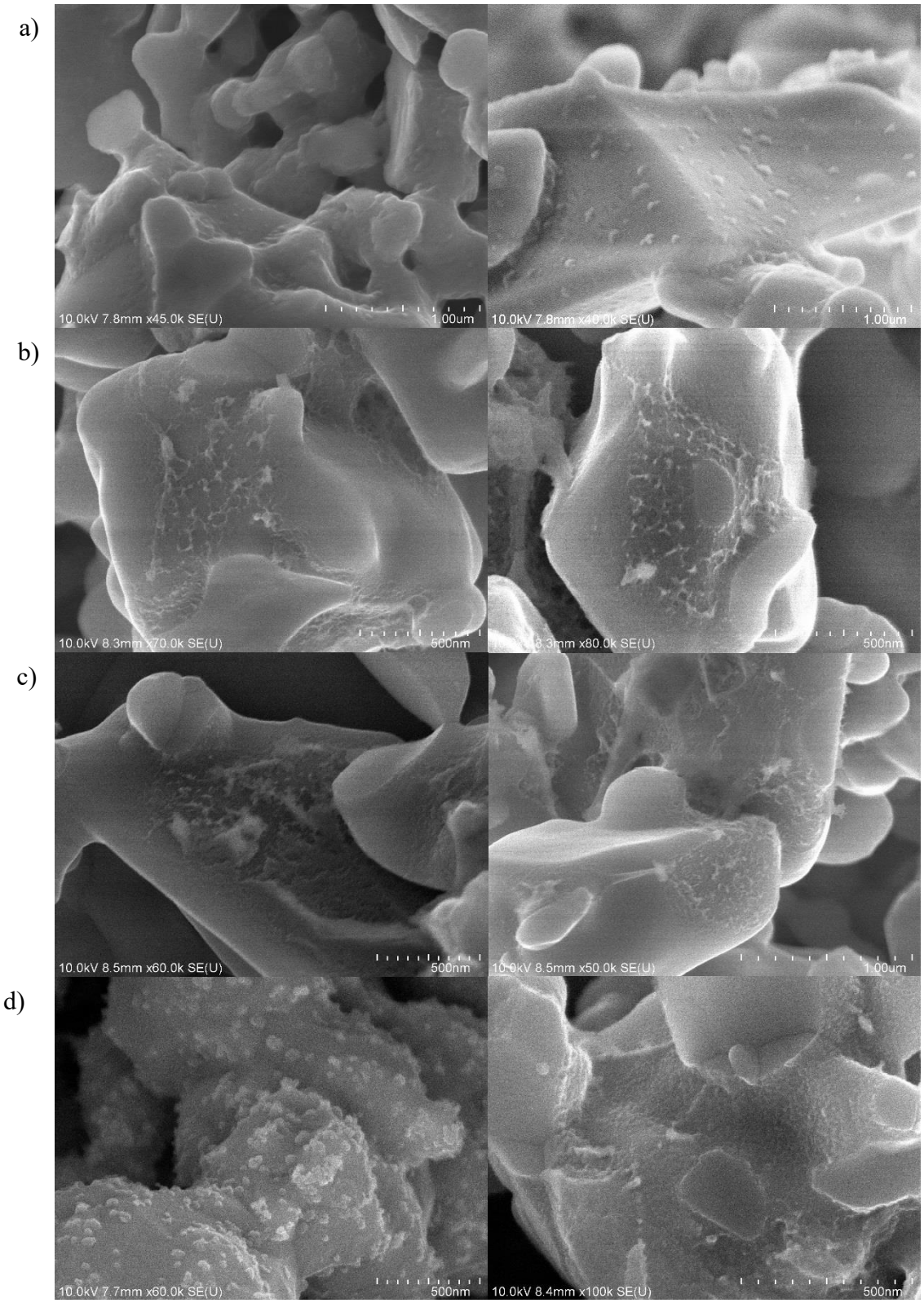

Figure 30. SEM images of a) 0.03M UDC, b) 0.10M UDC, c) 0.5M UDC and d) 1.0M UDC. Note the morpohology changes from 0.5M to 1.0M. Each row is the same sample at two different regions. Note the scale bars are either 500 nm or 1000 nm.

4.4 Thin Films of Undoped Ceria

4.4.1 Sputtering Deposition

Testing conformal thin films is a difficult in a porous cathode, which was the motivation for creating the asymmetric cell in this work. This set up allowed for conformal films of ceria to be deposited via RF sputtering. The sputtering set up has been previously described. Briefly, for each deposition the chamber was pumped down to less than 5 E-5 mbar and then backfilled with argon up to 1.6E-2 mbar working pressure. The power was ramped slowly to 20W and the thickness was controlled by varying the sputtering time. The deposition rate of the ceria at 20W and 1.6E-2 mbar working pressure was approximately 40 nm/hour. A cross-section of the ceria film deposited on a silicon wafer is shown in Figure 31. The as-deposited film was dense and evenly conformal throughout the width of the substrate. Figure 31 b) shows a top down view of the as deposited thin film of ceria. The top down view demonstrates the uniform small grains on the order of 50 nm in diameter.

While the SEM cross-section appears to show a dense film, closer inspection via TEM demonstrates that both the LSCF and thin film ceria coating were porous. Figure 32 shows the TEM cross section of the 80 nm ceria-coated LSCF. Figure 32 a) shows the transition from dense SDC electrolyte to porous LSCF with an 80 nm ceria coating. From those TEM images it can be seen that the LSCF supported significant nanoscale porosity with some porous channels extending from the SDC substrate to the surface. Judging by this 2-dimensional cross-section, the LSCF appears to have continuous porosity throughout the thickness of the film. Figure 32 c) and d) reveal the columnar morphology of the ceria

coating. The ceria film also shows a rougher surface than the LSCF film. Also notice the poor physical connection between the ceria and the LSCF. There is considerable porosity between the two different films. As opposed to PLD, where the substrate is typically heated to 600-700°C, the RF sputtering used in this work deposited the film at room temperature. With less thermal energy available for mass transport, films deposited at these lower temperatures can maintain porosity. Figure 32 e) shows the selected area electron diffraction pattern for the surface modified LSCF. While both films were deposited at room temperature, there exhibit much different morphologies. The rings in the pattern correspond to the ceria film and indicate it is composed of small grains with random orientation. This coincides with the small morphology seen in Figure 31. The bright spots in the diffraction pattern arise from the a very crystalline LSCF thin film. The following electrochemical data is based off the microstructure shown in Figure 31 and Figure 32.

4.4.2 Conformal Thin Film

The conformal thin films of ceria were electrochemically characterized under open circuit voltage and under bias. As previously mentioned, the asymmetric cells were tested in air using the compression cell set up. The connections were made with silver paste on the porous counter electrode and silver mesh on the dense working electrode. For all biased measurements, a negative applied potential was used with the dense cathode defined as the working electrode. The LSCF dense backbone was kept at ~450 nm and the thickness of the subsequent ceria film was varied at 80, 160 and 320 nm.

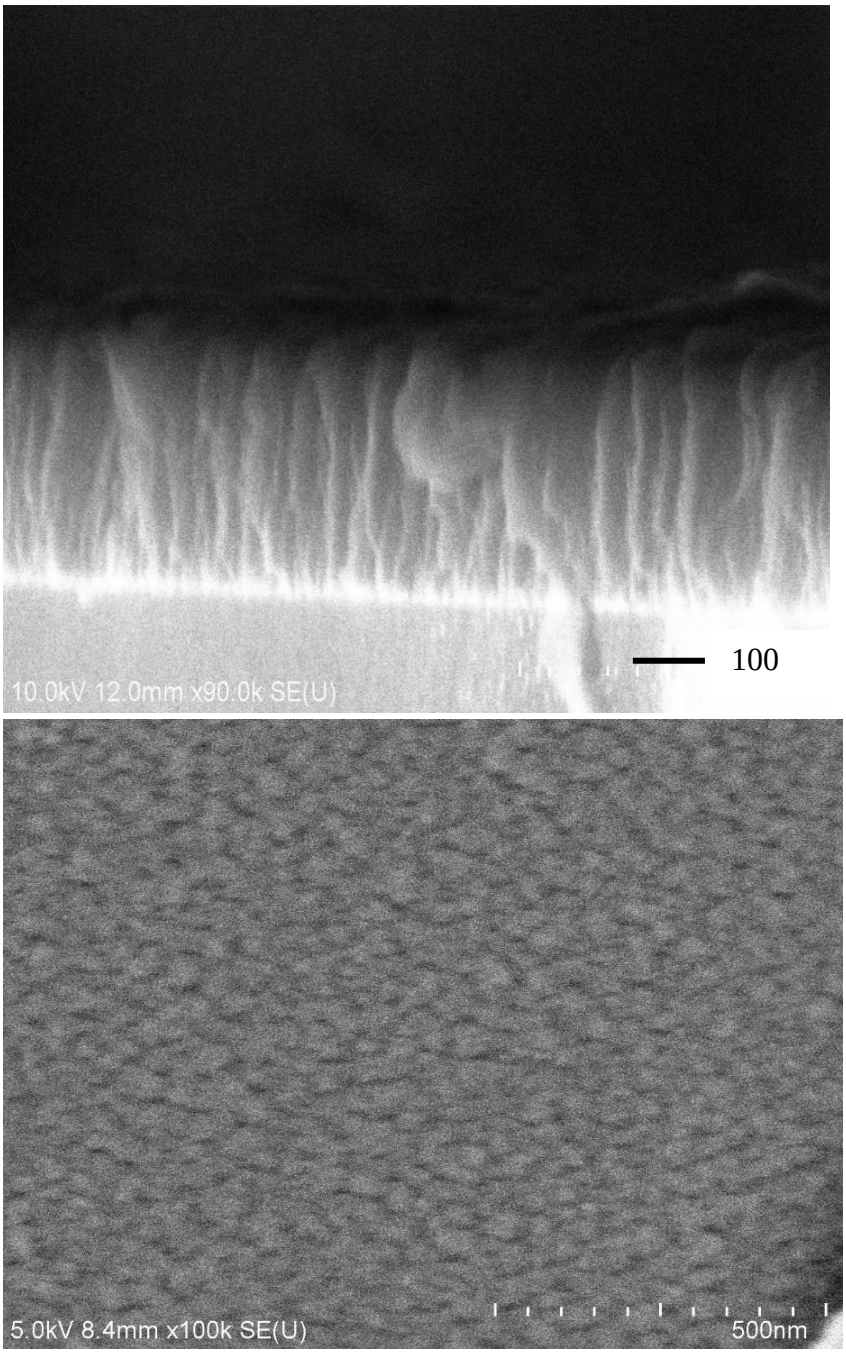

Figure 31. SEM of the cross-section of the ceria film deposited on a silicon wafer. The film thickness is approximately 340 nm.

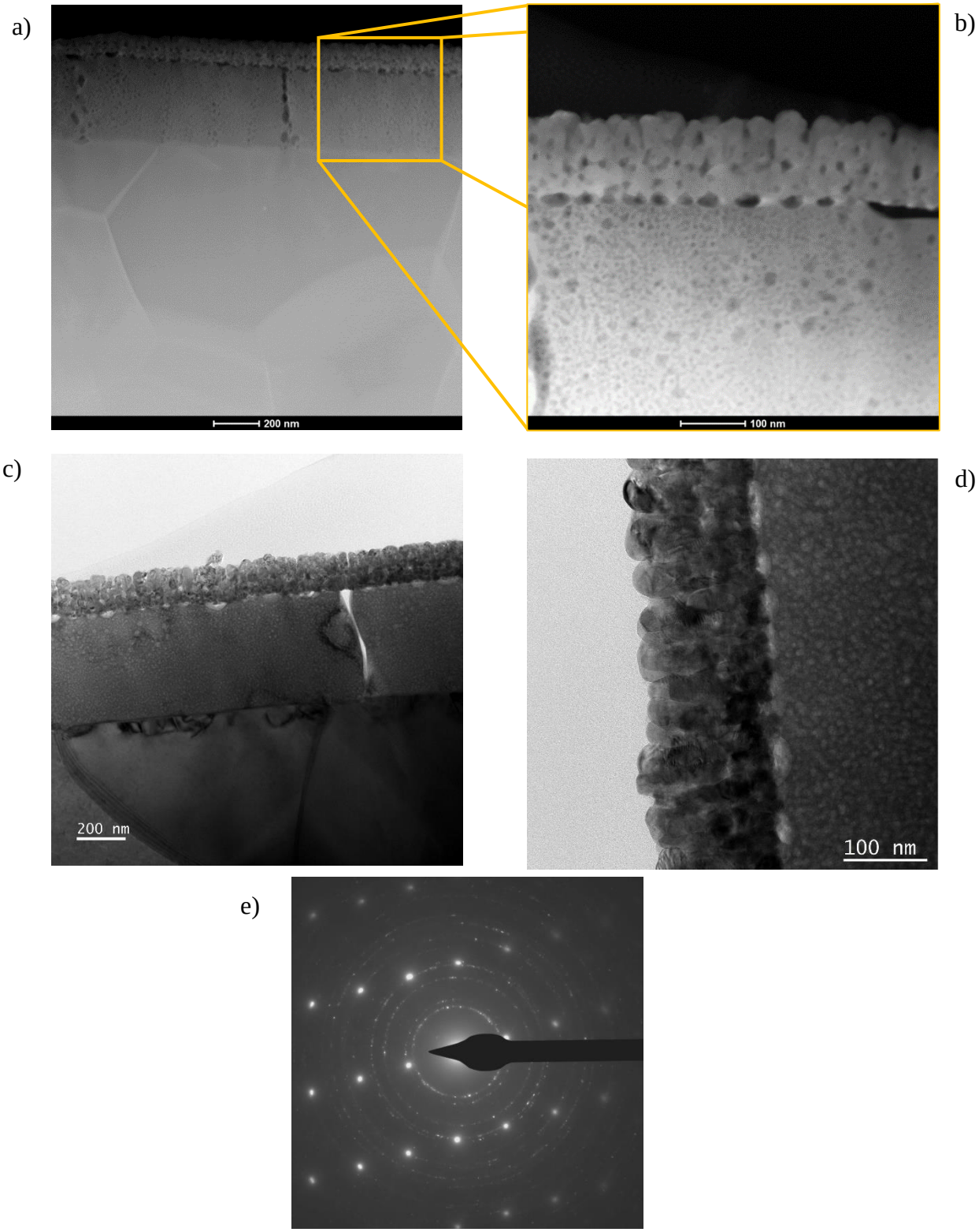

Figure 32. TEM cross-section of the asymmetric cell a) showing the dense SDC support, the LSCF cathode and the ceria coating, b) zooming in on the LSCF and the ceria coating on top, c) showing contrast between the ceria and LSCF, d) zooming in on the columnar structure of the ceria film and e) diffraction pattern of the ceria coated LSCF.

The Nyquist plot of impedance variation with film thickness is shown in Figure 33. The thinnest coating of 80 nm showed an initial increase in polarization relative to the reference cell without any ceria coating. However, the increasing the ceria film thickness to 160 and 340 nm showed a decrease in polarization resistance of nearly one order of

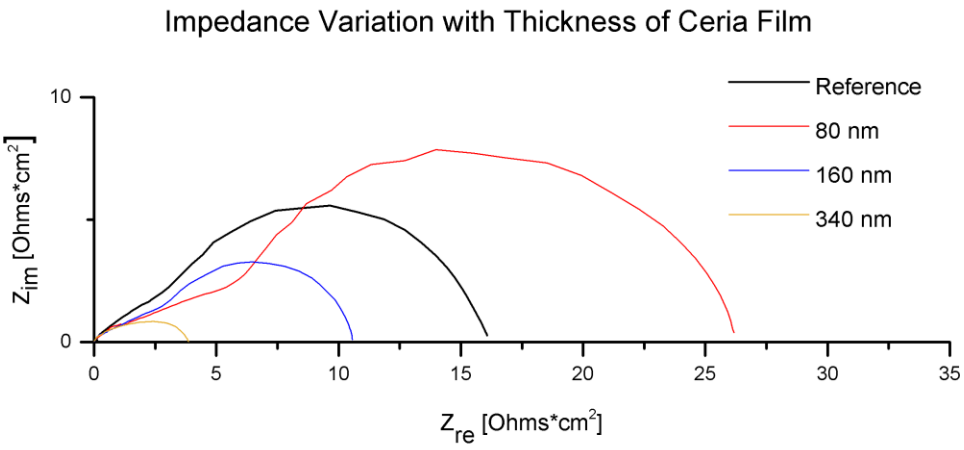

Figure 33. The variation in electrochemical impedance as a function of ceria film thickness.

magnitude. Figure 34 shows the calculated impedance as a function of film thickness. This trend replicates the trend observed in the undoped ceria infiltrated cells, where lower molarity solutions initially increased polarization resistance while the higher molarity solution decreased the polarization resistance. The higher molarity solution deposited more solution per given volume infiltration resulting in a more conformal-like and relatively thicker film. The EIS for these samples were all taken at open circuit voltage. While this serves as a useful indicator for cell performance, impedance behaviour under bias is more representative of fuel cell operating conditions.

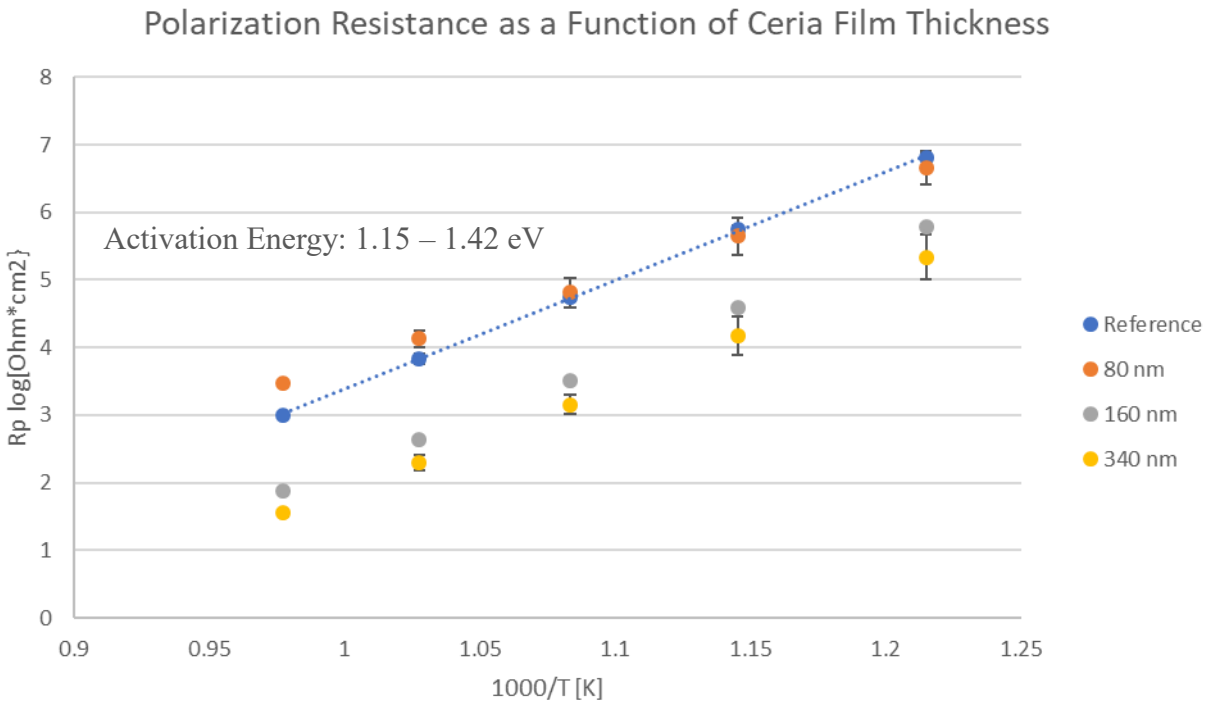

Figure 34. Plot of polarization resistance as a function of ceria film thickness.

The variation of impedance under bias for the reference LSCF thin film is shown in Figure 35. All biased measurements were taken at 750°C in ambient air. For each sample, the cathodic bias was varied from OCV to about -0.6V. However, using only the applied potential is not as helpful in comparison between cathodes. The overpotential is a more accurate metric to compare different cathodes because it takes into account the voltage drop associated with the ohmic resistance. The overpotential was calculated by the following equation:

$$\eta = V_{applied} - iR_{ohm} \qquad \textbf{Eq 26}$$

Where η is the overpotential, $V_{applied}$ is the potential applied between the working and counter electrode, i is the current, and R_{ohmic} is the ohmic resistance, which was taken from the impedance spectra.

Figure 35 a) displays the effect of increasing biased voltage. Two important observations come from this plot. First, polarization resistance decreases relative to the OCV impedance. Second, there is a saturation of improvement after -0.2V. Further biasing does not further decrease polarization loss. In fact, it increases slightly with larger cathodic biases. While the magnitude of the polarization resistance changes, the shape of the arcs does not. This indicates that the mechanism is not changing with the application of the bias. Figure 35 b) shows the change in impedance under OCV conditions after the final biased measurement. For the reference LSCF film, there is a small positive residual effect initially after the biased measurement. However, the impedance returns to the original OCV value after 2-3 hours. In comparison to the ceria modified films, the impedance change after the biased measurement is almost negligible, as will be shown in the following plots.

Figure 36 shows the behaviour of the asymmetric cell with an 80 nm thin film ceria. There are several important distinctions between the thin film ceria coating and the reference LSCF backbone under a bias. Figure 36 a) shows the same trend of decreasing polarization under increasing cathodic bias. However, the raw data shows significant deviation from the expected arc. With the reference backbone, the same arc shape was maintained independent of the magnitude of the bias. For the 80 nm coating, a -0.08V overpotential showed almost no effect on the impedance, but a -0.15V overpotential showed a dramatic improvement and a non-static impedance with time. The phrase “non-static” speaks to the fact that the data points do not form a regular arc due to the time

interval used to collect the data. Because each point represents a different frequency, there is an increasing time interval between data points as the EIS potentiostat moves from high to low frequency. If the impedance changes with time and the time interval is significant with respect to that change, the data points will deviate from an expected arc. For instance, if the impedance of the asymmetric takes several hours to reach an equilibrated value under a given condition, the impedance arc is not anticipated to deviate during the test. However, if the impedance takes 5-10 minutes to equilibrate under a given condition (such as under a cathodic bias) and there is 40 minutes in between data points being collected, the arc collected during the impedance run will deviate from the expected arc. If the polarization resistance increases, an elongated arc would be expected. If the polarization resistance decreases, the arc would retreat towards the origin. For the 80 nm ceria film under -0.15V and -0.2V overpotential, there is a noticeable decrease in polarization resistance measured as frequency decreases. As with the reference LSCF thin film, the decrease in polarization saturates after about -0.25V. However, the data for the 80 nm ceria still shows a large scatter, i.e. not forming an exact arc as expected. This large scatter was evident in multiple samples and was characteristic of the 80 nm ceria film. Figure 36 b) displays the change in impedance at OCV after the biased measurements were taken. The first measurement taken after the bias (blue triangles) shows the elongated arc that occurs when the impedance increases on the time scale of the measurement as mentioned previously. This indicates that the initial relaxation is relatively quickly. From that point, the polarization resistance increases with increasing time. The Nyquist plot also shows that after about 20 hours, the relative change in resistance with time is small with the value holding slightly below the original impedance. Notice also that the ohmic resistance (the first x-intercept) decreased

after the biased measurement and maintain that lower value throughout the following 20-hour dwell.

a)

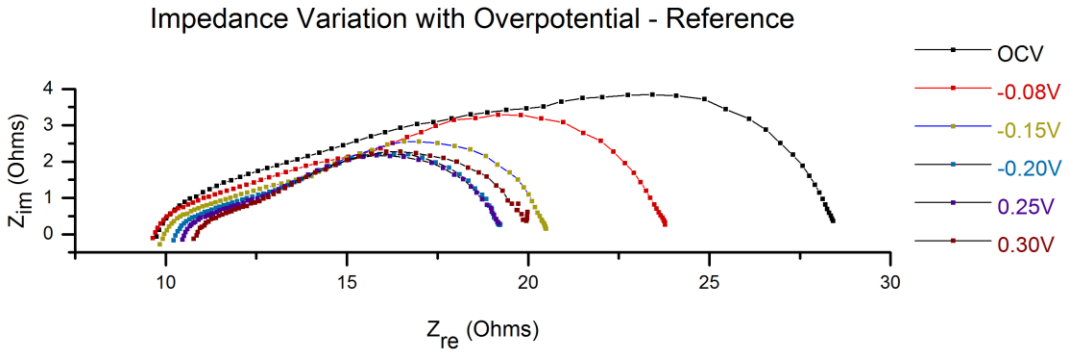

b)

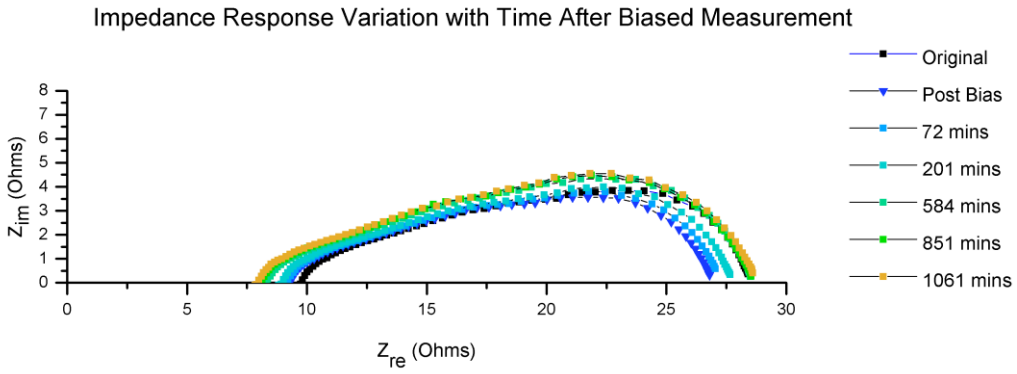

Figure 35. Impedance response of reference LSCF film a) under varying bias and b) under OCV after biased test.

Figure 37 shows the Nyquist plots for the LSCF dense cathode with a 160 nm ceria film. As seen in a), the impedance is relatively unchanged with the application of a cathodic bias. While there is a slight decrease in the polarization resistance, the change is much more subdued when compared to the LSCF reference film and the 80 nm ceria-coated LSCF. Note that the overall polarization resistance is smaller than the reference and the 80 nm ceria. Additionally, the plot in b) shows a different behaviour after the application of the cathodic bias. Instead of an initial decrease in resistance and a gradual regression to the pre-bias measurement, the 160 nm ceria-coated sample show increasing polarization

a)

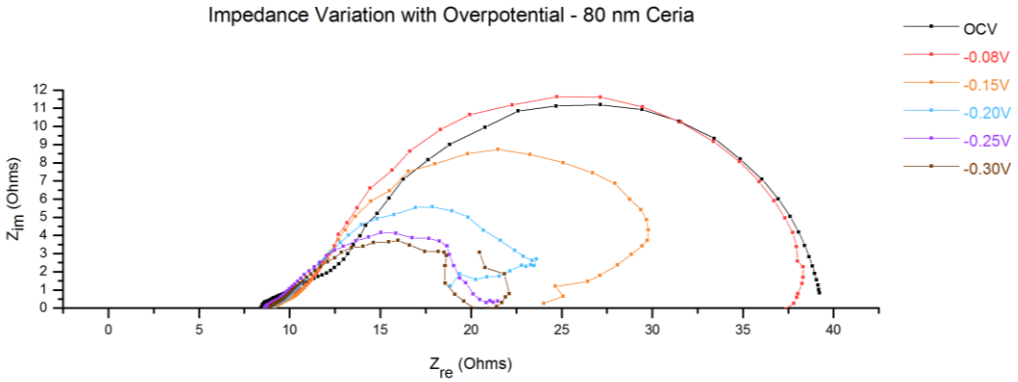

b)

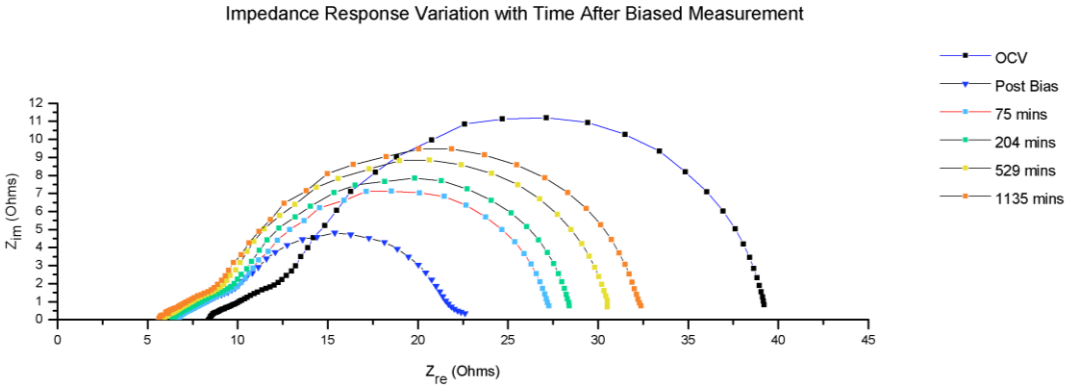

Figure 36. Impedance of asymmetric cell with 80 nm ceria coating a) under varying bias and b) the relaxation behavior after the biased measurement.

beyond original value. In other words, the performance is worse after the application of the bias, which is the opposite of the trend usually observed in SOFC cathode literature. Notice also that the shape of the arcs are similar to the previous LSCF and 80 nm coated LSCF samples.

Figure 38 shows the Nyquist plot for the LSCF cathode modified with a 340 nm ceria thin film. One of the first noticeable differences as compared to the previous samples is the shape of the impedance arc. The LSCF reference, the 80 nm ceria on LSCF and the 160 nm ceria on LSCF all had a dominant arc at lower frequencies with a minor arc at higher frequencies. However, the low frequency arc evident in the 340 nm ceria on LSCF samples is depressed. As with the 180 nm ceria, there is little change in impedance with the cathodic bias and there is a slight increase in the ohmic polarization. Figure 38 b) reveals the same behaviour as the 180 nm ceria: a small decrease in ohmic resistance and an overall increase in polarization resistance. The magnitude of the total increase in polarization is similar to the 180 nm ceria samples.

a)

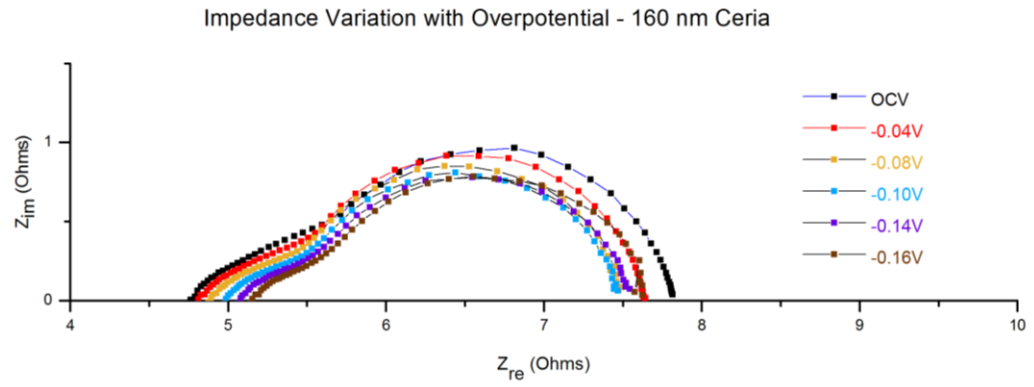

b)

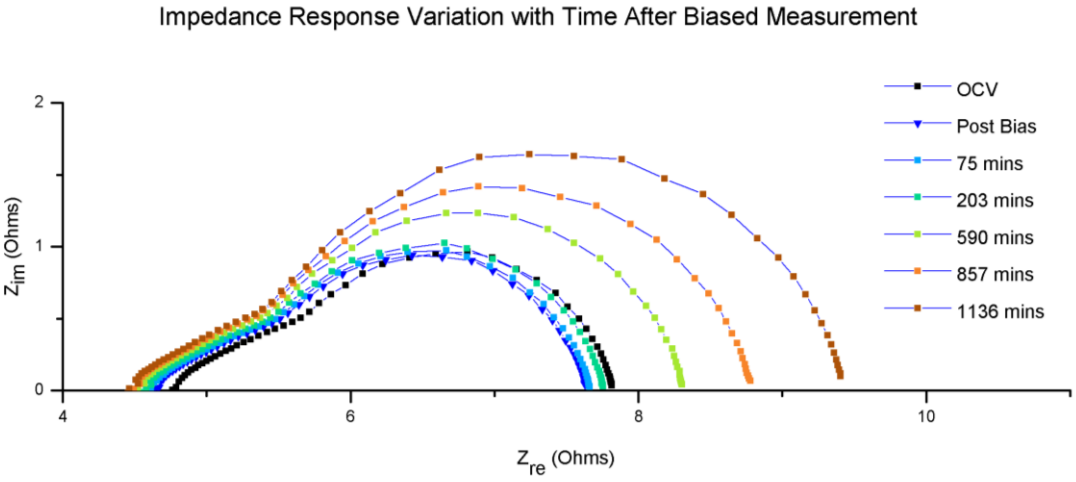

Figure 37. Impedance of asymmetric cell with 160 nm ceria coating a) under varying bias and b) the relaxation behavior after the biased measurement.

a)

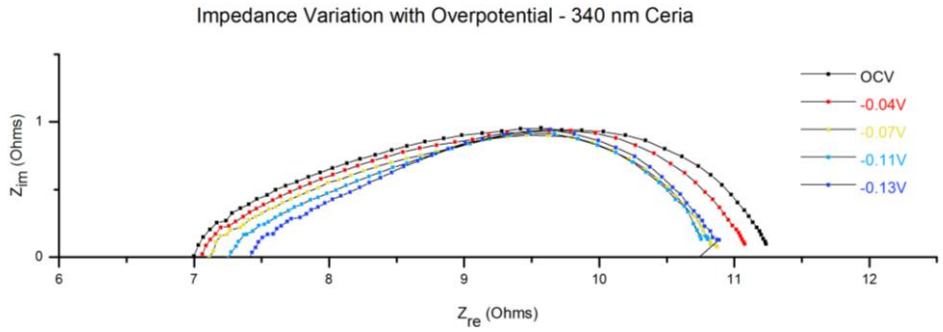

b)

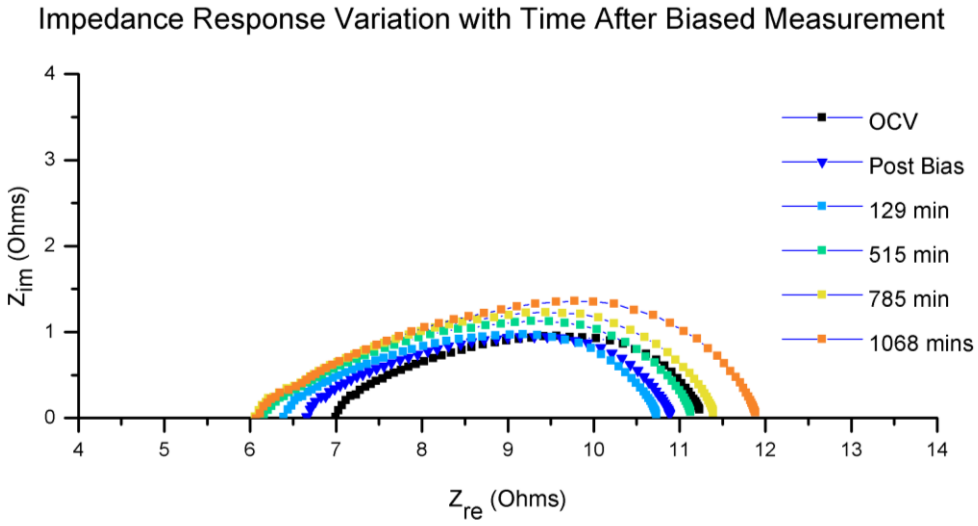

Figure 38. Impedance of asymmetric cell with 320 nm ceria coating a) under varying bias and b) the relaxation behavior after the biased measurement.

4.5 Infiltration of Samarium Doped Ceria

Three different doping levels were used for the SDC infiltrations including 10, 20 and 30 mol % samarium. Most infiltrations in the literature have focused on 20DSC because it is the doping level for optimum oxygen ion vacancy conduction when SDC is used as an electrolyte. However, increasing the doping level will likely suppress the

reduction of Ce^{4+} since there are less Ce^{4+} present in higher doped solutions due to the electroneutrality of the aliovalent dopant.

The polarization data for varying concentrations of precursor is shown in Figure 39. The activation energy does not appreciably change and is close to 1.98 eV for both the reference and infiltrated samples. This value is slightly higher than expected as references to literature values. As also seen in the UDC samples, there is an increase in polarization for lower concentrations (0.1M, 0.2M) and then decrease with increasing concentration. The maximum performance is at 0.3M after which the polarization begins to increase, but remains below the reference cathode.

The polarization data for varying concentrations of 20SDC is shown in Figure 40. Similar to the previous behaviour of UDC and 10SDC, lower molarity infiltration caused an increased in the polarization resistance. After 0.2M 20SDC, increasing the molarity decreased the resistance up to 0.4M 20SDC, which showed better performance than the reference LSCF uncoated cathode. The activation energy changed slightly from about 1.98 eV for the reference to about 1.8 eV for the 0.4M 20SDC. Infiltration with 0.5M 20SDC showed a decrease in performance.

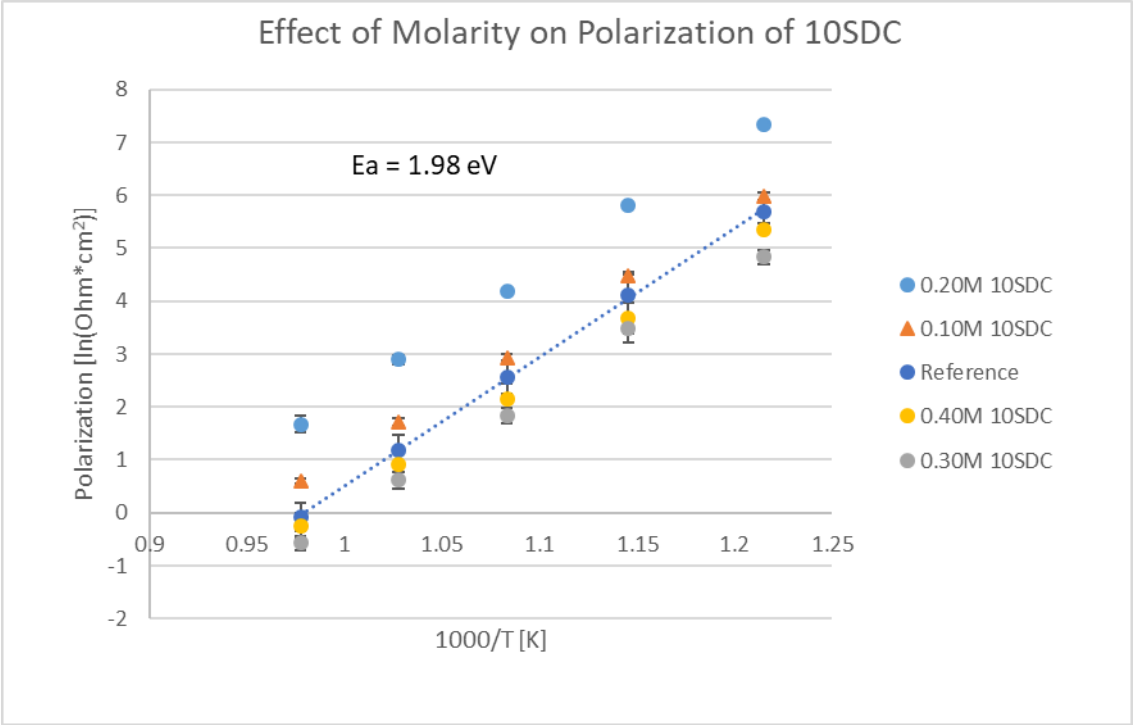

Figure 39. Polarization resistance changes as a function of the molarity of 10SDC. The lowest polarization resistance is found with 0.3M solution.

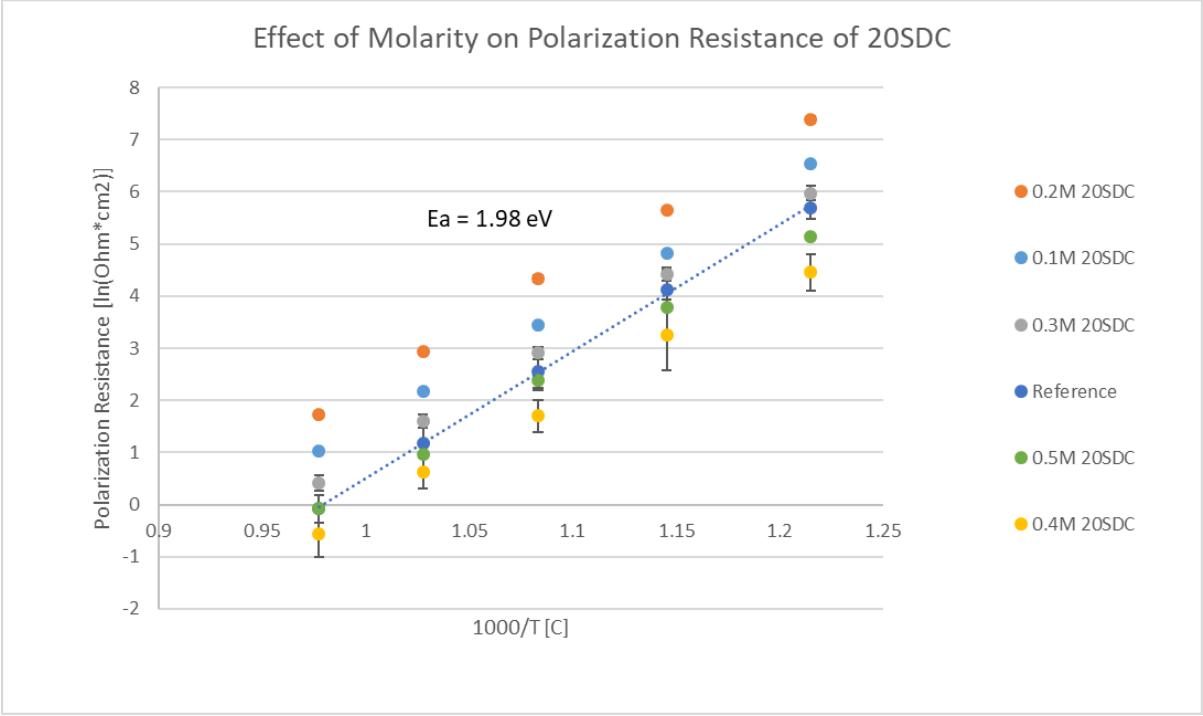

Figure 40. Polarization resistance changes as a function of molarity of 20SDC.

The literature suggests that 20SDC should be the best because of its optimum ionic conductivity for bulk ion conduction. However, the literature also proposes that increased vacancy concentration is important for ORR. Thus, solutions of 30SDC were also infiltrated. The 30SDC infiltration showed the same trend in performance as the 10SDC and 20SDC as shown in Figure 41. At low molarities, the infiltrations showed a negative effect on the performance with a minimum in resistance for the 0.3M solution. At 0.4M, the performance regresses to the baseline LSCF cell. The fact that the 30 SDC equivalent performance gains to the 20SDC raises the idea that oxygen vacancy concentration may be more important than the oxygen ion conductivity. The results suggest that the oxygen vacancy concentration doesn't necessarily increase the performance, but having a surface with oxygen vacancies is import to the ORR. It has been demonstrated that the activation energy for oxygen conduction is lowest and the ionic conductivity is highest at the optimum 20 mol% samarium doping[76]. Because the performance increase seems independent of the doping concentration, it appears that the infiltrated particles may increase performance by the vacancies at the interface of the SDC and LSCF, which would vary less than the bulk oxygen vacancy concentration.

An interesting aspect of all three infiltrations is the intial decrease in performance followed by the dramatic increase in peformance beyond the LSCF baseline. This is contrary to previous SDC infiltration[26]. There are two differences between that previous report and this work. In this work, only 5 µL of solution was infiltrated (versus 10µL) and there was no additional solvent added to increase wettability (versus 0.6:1 propanol in water). The change in performance could be related to morphology of the deposited material at lower concentrations. For example, the smaller particles could support a

different thermodynamically stable concentration of vacancies as has been previuosly descried in the literature review. For this work, the analysis will focus on the performance increase of all doping levels at the optimum doping concentration.

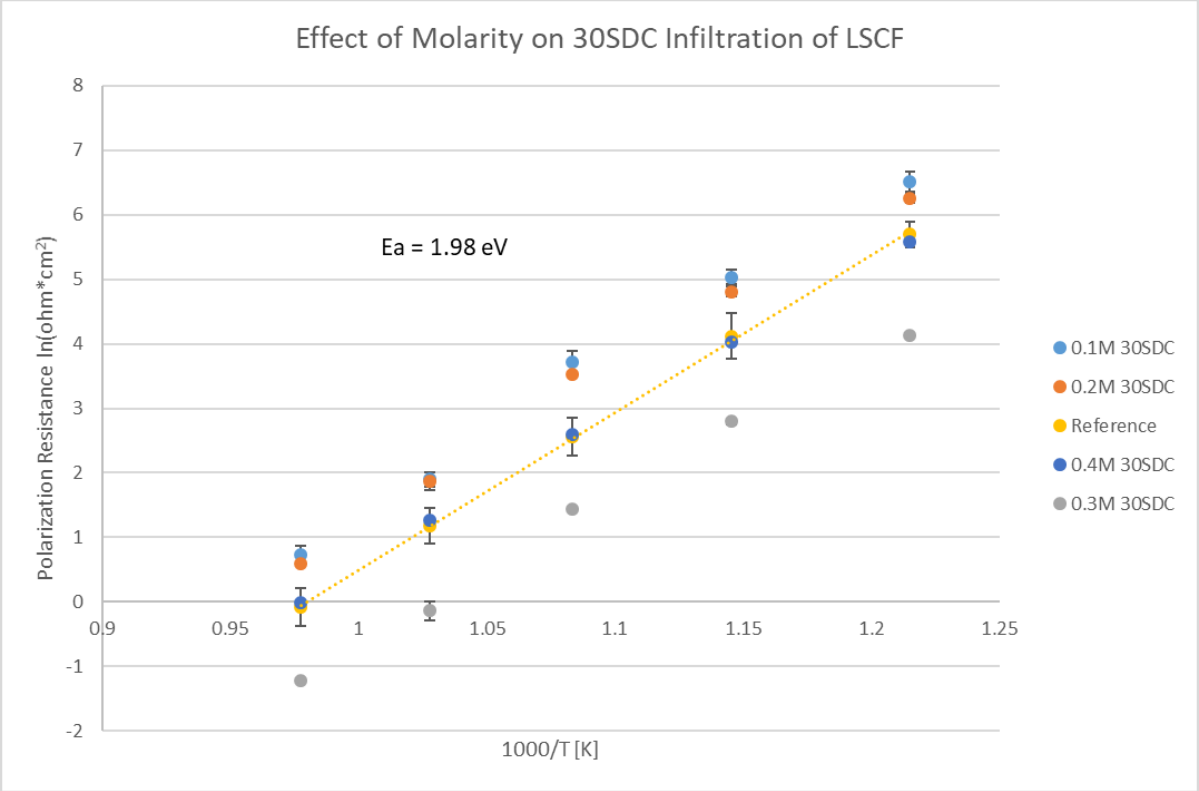

Figure 41. Polarization resistance of 30SDC infiltrated into LSCF symmetric cell.

4.6 Conformal Thin Films

The SDC thin film coatings were fabricated under the same sputtering conditions as the previous ceria coated LSCF asymmetric cells. For this set of experiments, the thickness of the SDC film was varied to 80 and 160 nm. All electrochemical testing was performed at 750°C in ambient air. The cathodic bias was applied using the dense film as the working electrode and the porous LSCF as the counter electrode. The overpotential was calculated as described in the previous section.

Figure 42 is a Nyquist plot of the impedance measured for the reference, 80 nm SDC film and 160 nm SDC film under OCV. The first thing to note is that the impedance increases with increasing thickness of the SDC film with the reference LSCF film showing the lowest polarization resistance of the three samples. Another aspect of the plot to note is the change in the arc shape for the 160 nm SDC film. At higher frequencies, there exists a depressed semi-circle that is apparent until the larger arc associated with the ORR begins to dominate at intermediate and lower frequencies. Looking just at the polarization resistance, the impedance increases by about 2x from reference to 80 nm-coated SDC and another 2x to 160 nm. Keep in mind that the calculated polarization resistance of the 160 nm coated LSCF adds the contribution by both phenomena (i.e. both arcs instead of only calculating the ORR impedance from the single dominant arc). This depressed smaller arc seen at higher frequencies may be due to a mixed diffusion-reaction limited condition that occurs with thicker SDC films.

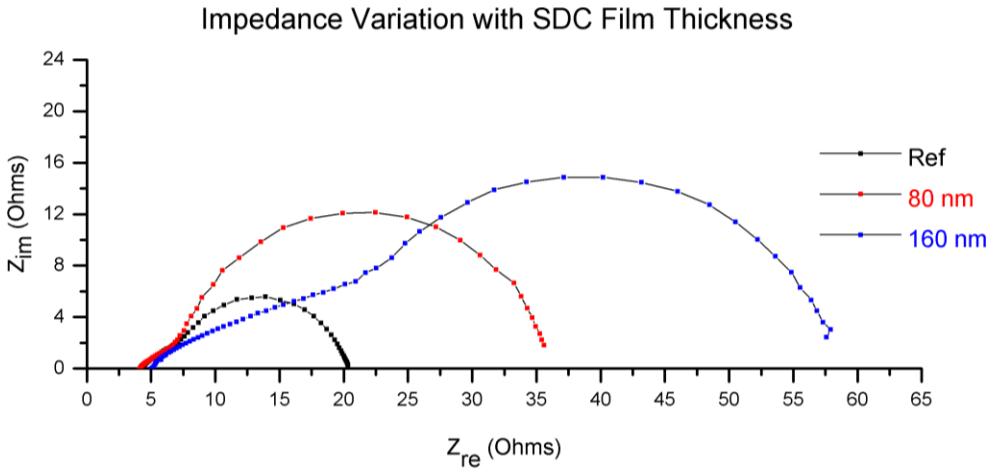

Figure 42. Nyquist plot showing the relationship between impedance and thickness of 20SDC film.

Figure 43 demonstrates the effect of bias on the SDC-coated LSCF samples. For both the 80 nm and 160 nm films, applying a cathodic bias decreases the polarization drastically. In comparison to the LSCF film reference, which saw a polarization decrease of approximately 50% under bias, the SDC coated LSCF showed nearly an order of magnitude decrease. Also different was the behaviour under bias beyond -0.2V. In the reference cells, there was a minor decrease in polarization resistance after -0.2V. However, for the SDC coated samples, there was no saturation observed. Increase the applied cathodic bias beyond -0.4V further decreased the observed impedance. Beyond -0.3V, the relative change in impedance was less significant than at a lower bias. For reference, a typical fuel cell in a commercial operating application would most likely be operated around 0.7V for optimum power output.

a)

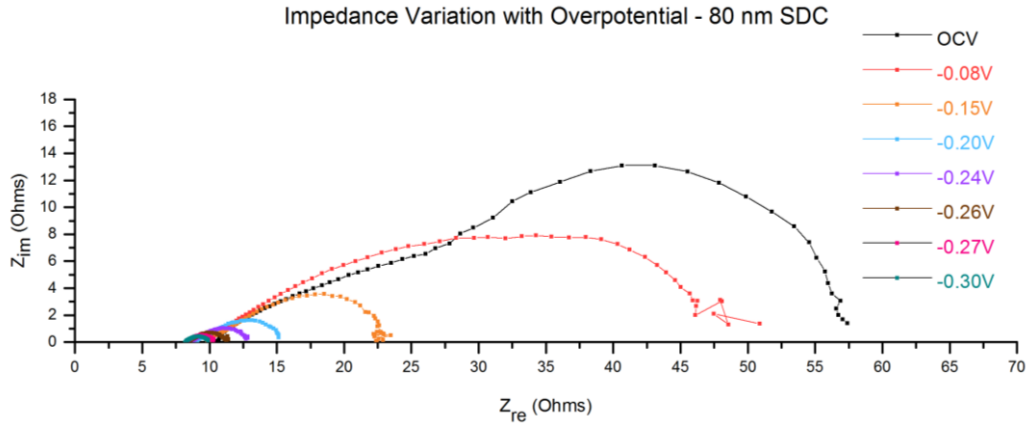

b)

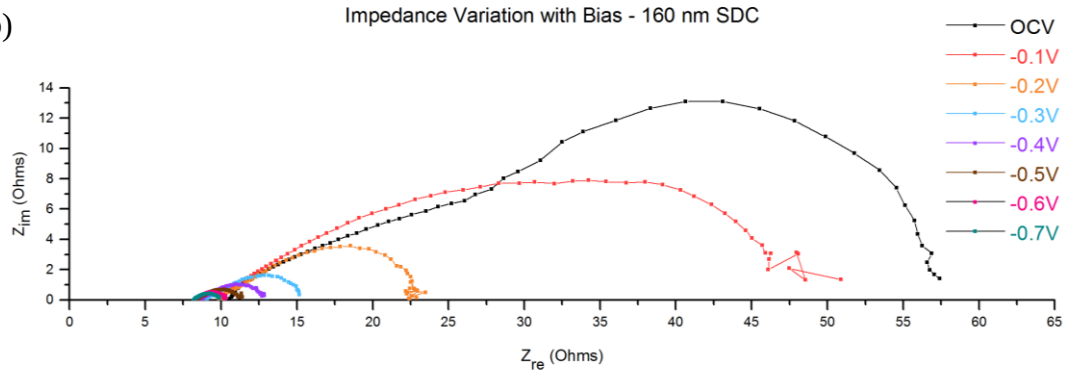

Figure 43. Nyquist plot of a) the 80 nm SDC-coated LSCF and b) the 160 nm SDC-coated LSCF under varying bias

4.7 Discussion

When viewed together the previous thin film and infiltration experiments give insight into the behaviour underlying the performance change due to the surface modification.

First, I'll discuss the doped ceria because it helps add some context to the undoped ceria results. The infiltrated samples with varying samarium dopant concentration showed that polarization resistance does not scale with ionic conductivity. The interesting aspect of the test was that 10SDC, 20SDC and 30SDC all showed nearly the same enhancement in performance at approximately the same molarity of infiltrated solution. This indicates two possible factors that govern ORR performances. First, the morphology of the surface modification is important. Because the molarity influences the morphology, the optimal coating is a slightly larger, but not complete dense film. Figure 30 shows how the morphology changes for the undoped ceria, which is the same trend seen in the morphology of the doped ceria infiltrated solutions. This means there is an optimum morphology between the small, isolated nanoislands at low molarities and the more conformal thicker films at the higher molarity. At higher molarities, there may also be a tendency for pores to be blocked due to slightly higher viscosities which is commonly observed for concentrated solutions. This blocking of pores could would also manifest as a decrease in performance because of a more limited active surface area as compared to the reference porous cathode. The higher concentration solutions could have also led to a thicker deposited film, which could be the cause of the decrease in performance as well. The conformal thin films deposited on the asymmetric cell testing platform further justify the interpretation that a thicker SDC film decreases performance for the doped ceria samples. The asymmetric cell set up eliminates any decrease caused by isolation of pores. The increase in polarization resistance observed with increasing film thickness demonstrates that the dense conformal thin film decreases performance.

With these results in mind, it is possible to describe a possible route for the performance enhancement for the doped ceria surface modification as shown in Figure 44. Since the optimal performance enhancement was found with the infiltration, the optimal morphology is most likely discrete particles on the surface of the LSCF backbone. Because the performance enhancement is independent of bulk ionic conductivity, then the oxygen transport is likely to occur on the surface of the particle instead of through the bulk. Again, if the bulk ionic conductivity was the governing factor than it would be expected that the thin film SDC would show a decrease in polarization. However, the conformal films showed higher polarization resistance relative to the reference LSCF reinforcing the idea that the discrete particle morphology is more important. The concept that you can "overdope" SDC beyond the maximum for ionic conductivity and still observe an increase

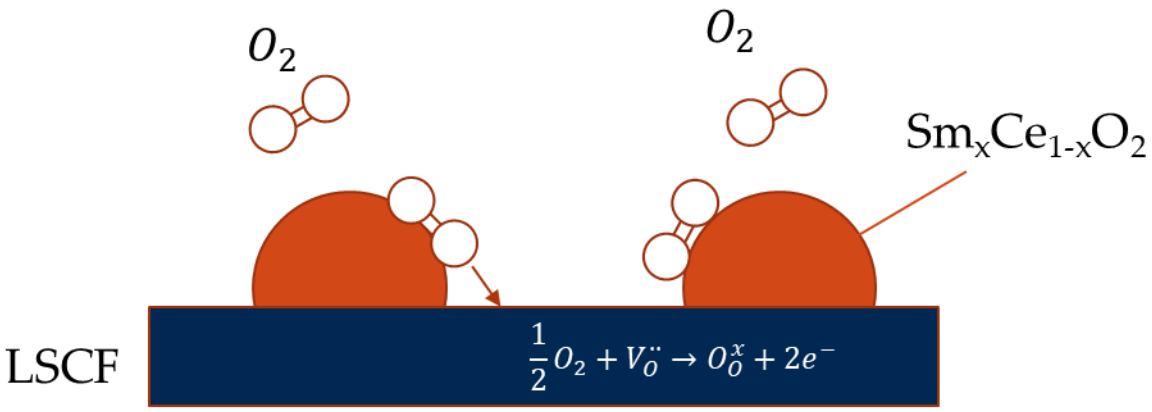

Figure 44. Schematic showing a possible mechanism for enhancement of the doped ceria surface modification on an LSCF backbone

in performance is supported by literature. Yang et al who found that doping samarium into ceria beyond 20 mol % results in increased effect interactions (between cation and vacancies), but electrochemical strain microscopy indicates these associated defects may lower activation for ORR and increase surface exchange rates[77].

It could be argued that the conformal films were relatively thicker than the infiltrated samples. However, the 80 nm thickness is on the same order of magnitude as the infiltrated samples judging by the SEM which shows particles on that same order of magnitude. While TEM was not performed on the infiltrated samples, the thickness from a cross-section can be estimated to be on the order of 30 to 50 nanometers.

The performance of the doped ceria thin films under bias helps develop an understanding of the undoped ceria under bias as well. Previous thin film cathode literature has shown that performance will increase under an applied cathodic bias. However, the performance increase under bias has not been directly correlated with oxygen ion vacancy concentration as is demonstrated in this work. One of the key features of the impedance of the 80 nm and 160 nm SDC films on LSCF is the constantly decreasing polarization resistance with increasing bias. Recall, the SDC films showed a drastic decrease in polarization with increasing cathodic bias while the 160 nm and 320 nm undoped ceria showed very little change in polarization resistance with cathodic bias. The change of polarization resistance as a function of cathodic bias are compared in Figure 45. In this figure, there are three distinct regions describing different behaviours under bias. For the 160 nm and 320 nm undoped ceria films, there is little change in polarization resistance with increasing cathodic bias. For the 80 nm and 160 nm SDC, there is a drastic decrease in polarization with increasing cathodic bias. However, the 80 nm ceria and the LSCF reference films demonstrate an intermediate response to increasing bias. It is important to keep in mind that these values are normalized. In absolute terms, the 160 nm and 320 nm ceria showed the lowest polarization and the 80 nm and 160 nm SDC showed the highest polarization resistance. This visual allows us to make some nuanced observations about the

thin films. Suppose that the vacancy concentration in the film determines the behaviour under bias. It would be expected that the SDC films and the thicker undoped ceria films would have opposite behaviour because the former has high oxygen vacancy concentration and the latter has relatively much less. We do in fact see that the SDC films show a drastic change under bias while the thicker undoped ceria films show relatively little change under bias. The LSCF reference film serves as valuable data point because of its intermediate vacancy concentration relative to the undoped and doped ceria. This intermediate ionic conductivity fits directly in between the doped and undoped ceria films seen in Figure 45. With the previous knowledge in mind, the data point that sticks out is the 80 nm thin film of undoped ceria. A priori, it is expected that this undoped ceria film would have a low vacancy concentration, which would be in line with expectations for bulk ceria. However,

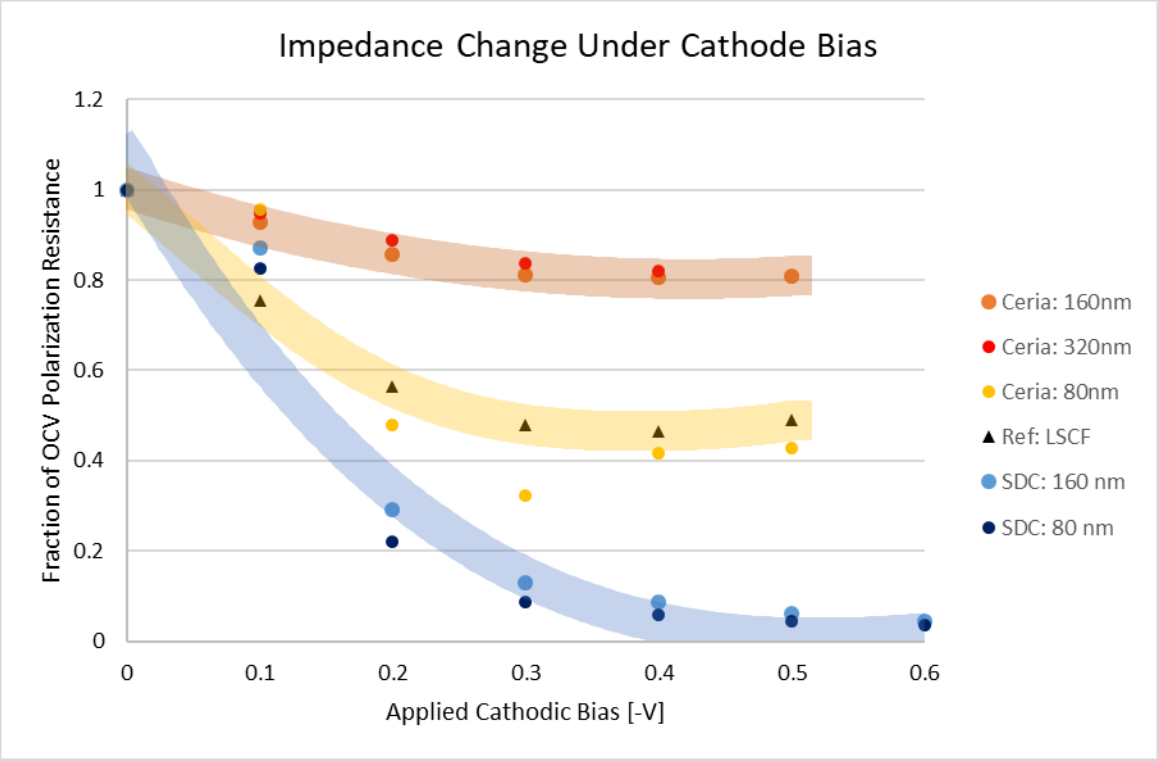

Figure 45. Comparison of the change in polarization resistance as a function of cathodic bias

the experimental results indicated rather significant oxygen vacancy concentration. Recent thin film experimental literature suggests that thin films of undoped ceria can support higher vacancy concentration than bulk undoped ceria, especially under bias. Zhang et al probed the oxidation state of cerium in a thin ceria film using ambient-pressure X-ray photoelectron spectroscopy[78]. One important result that work is the correlation between Ce^{3+}/Ce^{4+} oxidation reduction with applied bias shown in Figure 46. There are two main points to draw from the two figures. As demonstrated in a), under a cathodic bias there is a smaller concentration of Ce^{3+} (or a larger concentration of Ce^{4+}). The half reaction taking place on the cathode is:

Cathode $$\frac{1}{2}O_2 + V_O^{\cdot\cdot} + 2e^- \rightarrow 2O_o$$ **Eq 27**

Under equilibrium conditions there is a given vacancy concentration in the ceria. Under an applied cathode bias, the flow of oxygen ions is increased to the counter electrode meaning more of the oxygen ion vacancies are filled with an oxygen ion from the gaseous oxygen. Thus, the concentration of vacancies would be expected to be smaller. Figure 46 a) shows the quantitative difference under an applied bias as a relative decrease in Ce^{3+} which given an intimal Ce^{4+} state is a proxy for the vacancy concentration (lower Ce^{3+} means lower vacancy concentration due to charge balance considerations).

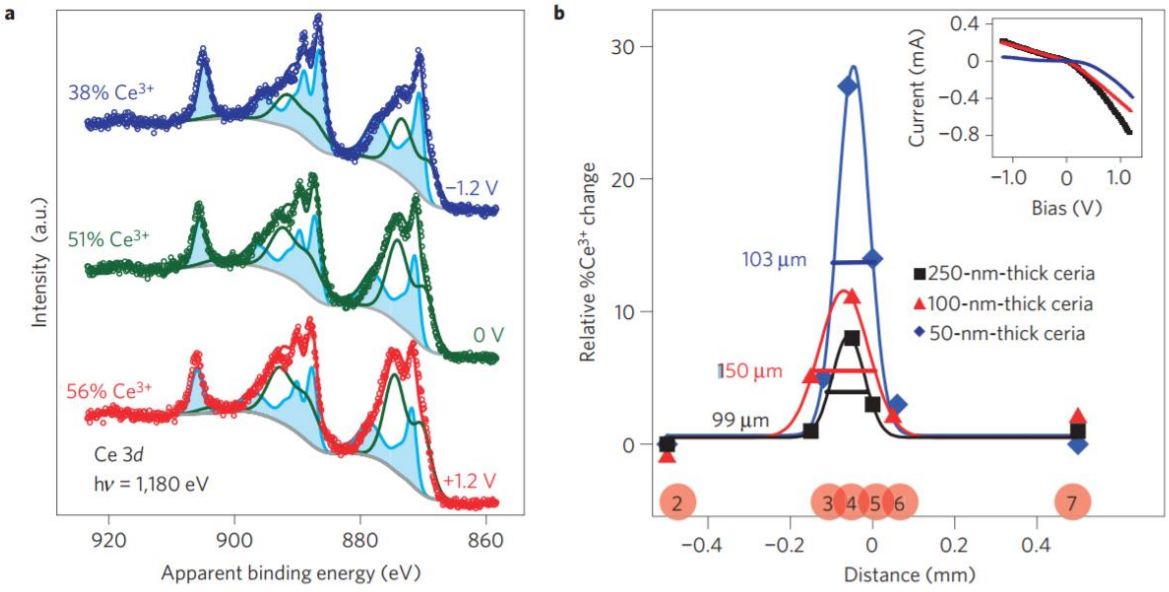

Figure 46. The change in oxidation state of a) a 50 nm ceria film under different applied biases and b) the relative % Ce3+ change under bias for varying film thicknesses. Figure taken from [78]**.**

The second point to draw from Figure 46 is the change in relative Ce^{3+} concentration for varying thicknesses of the ceria film. The films used in that work (50, 100, 250 nm) are very similar to the films in this work (80, 160, 320 nm), thus the behaviour under bias is a valid comparison. The plot shows that at a given bias, the relative change in Ce^{3+} concentration is inversely correlated to the film thickness. The 50 nm ceria film showed the largest change in Ce^{3+} concentration under bias.

At this point it is important to note that vacancy concentration may not be the ultimate predictor of ORR performance. As mentioned before, if vacancy concentration was the most important attribute, then the 20SDC films should have shown the lowest impedance. Instead, perhaps the amount of Ce^{4+} available to be reduced and/or the reducibility are better indicators. Referring back to Figure 45, the relative change in polarization resistance

may be a useful indicator for ORR activity. The SDC films showed the largest change under bias also have the highest vacancy concentration. The thicker ceria films show little change under bias, but have the lowest a priori vacancy concentration. The lack of change in polarization resistance under bias suggests there is not a large change in the vacancy concentration. On the other hand, the 80 nm ceria film showed the intermediate change in polarization resistance with bias suggesting there is some change in the vacancy concentration. Both of those observations coincide with the results in Figure 46. In other words, the thickness of the film influences the ease of which a Ce^{4+} can be reduced to a Ce^{3+}. If the ceria can easily reduce, then under a bias (i.e. realistic operating conditions), the Ce^{3+} is more stable thus inhibiting the incorporation of an adsorbed oxygen into the vacancy site. This idea is supported by the work of Suzuki et al where they demonstrated a relationship between grain size and enthalpy of formation as shown in Figure 47[79]. The important idea from that plot is that undoped ceria shows a marked change in oxygen vacancy formation energy with smaller grain size. In this case, grain size is being used as a proxy for film thickness in order to correlate to this work. However, the doped ceria does not show the same change in enthalpy of formation. This corroborates the previous rationale that relative change in polarization resistance under bias can correlate to enthalpy of formation of oxygen ion vacancies. In other words, the thinnest ceria film shows the poorer performance relative to the thicker ceria films because the Ce^{4+} has already been reduced to Ce^{3+} at a larger thermodynamically stable level. Thus, there is a larger driving force required to incorporate an oxygen in the vacant site for thinner films of undoped ceria. This concept is reinforced by work done in Gorte's group. Yu et al infiltrated different cathode materials into a YSZ backbone and then coated the composite cathodes

with ceria, strontium oxide and alumina[59]. They found that within several cycles of the ALD of ceria, the polarization resistance increased. The thicknesses of the ceria are on the order of nanometers and are an order of magnitude thinner than the films tested in this work. They suggested the ceria deposited via ALD could be predominantly in the +3 oxidation state although they did not provide any surface characterization to justify that assertion since the deposited films on the porous cathode did not provide a large enough signal for XPS or other surface characterization.

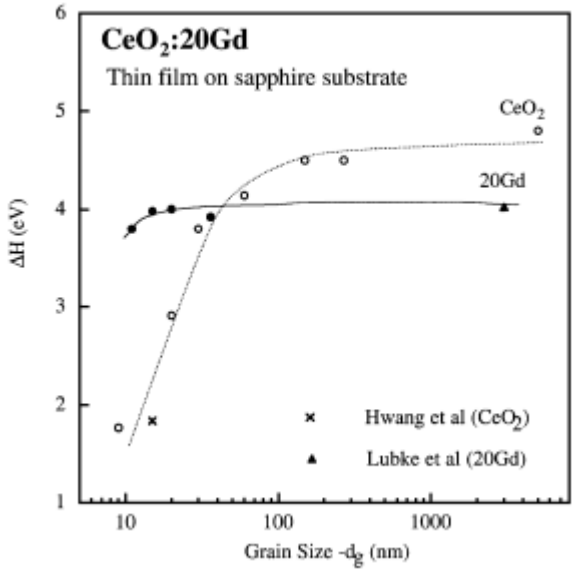

Figure 47. The enthalpy of formation for an oxygen vacancy in undoped ceria and 20GDC [79]

It is important to note that the preceding discussion has focused on explaining why the 80 nm thin film showed poor performance. The obvious question remaining is to explain why the 160 nm and 320 nm undoped films showed better performance than reference LSCF. It would be expected that thicker films of undoped ceria would serve to block the ORR. However, the porosity present in the deposited films allows for a reaction path for

the reduction of oxygen. Again, increasing the film thickness does not intuitively result in higher activity. Looking just at surface exchange coefficients, LSCF should perform better than the undoped ceria judging by experimental results on bulk powders. In order to further investigate, it would be necessary to have a better idea for how performance changes with thickness to identify at which point the ORR performance would decrease. Chueh et al demonstrated an interesting property of ceria films in anode environment[80]. The authors found that burying the nickel or platinum current collector under an SDC film showed the same polarization resistance as when the metal contact was on top of the SDC. In other words, the boundary between the gas phase and the ceria phase may be more important than the traditional triple phase boundary argument for improving performance on the anode. The stabilization of oxygen ion vacancies was attributed to a negative entropic contribution to the chemical potential of surface oxygen that shows less of a dependence on temperature and partial pressure of oxygen. It is noteworthy that the SDC films used in that experiment were on the order of 1 μm, which suggests perhaps thicker undoped ceria films have an opportunity to further increase performance. However, further work is needed to confidently answer any questions about improving performance with increasing thickness of undoped ceria. That works is beyond the scope of the current work.

CHAPTER 5. SURFACE MODIFICATION WITH PRASEODYMIUM DOPED CERIA

Modifying the surface of a cathode has been investigated, but previous literature has not been able to define the relative importance of vacancy concentration and electronic conductivity in terms of the ORR catalytic activity. Many studies will modify the surface with a new material, but often both the ionic and electronic conductivity are varied. Additionally, new materials with different crystal structures and different morphologies can also impact the performance beyond the intrinsic ionic and electronic conductivity. Thus it is important to be able to vary the ionic and electronic conductivity of a given single material and correlate those properties to ORR activity.

The goal of this chapter is to investigate the importance of ionic and electronic conductivity using the praseodymium doped ceria system. The scientific and technical objectives are as follows:

1. Identify the doping concentration that minimizes polarization resistance of an infiltrated solution on an LSCF backbone.
2. Identify key characteristics of the optimal solid solution by using techniques that mimic the realistic operating conditions of a fuel cell
3. Use XPS to characterize the praseodymium and cerium in the surface modification

5.1 Fabrication

Ceria has been a widely studied material for many decades in many different areas of catalysis. It is also commonly used in a fuel cell operating environment, which provides a vast foundation of previous literature to compare to. It's behaviour in many atmospheres and operating conditions have been probed and can help support future studies. Many of those studies have used a variety of dopants that vary the electronic and ionic conductivity. Praseodymia is single dopant that manipulates both electronic and ionic conductivity and thus is valuable to use in studying surface modification.

Recently, the increase in performance for state-of-the-art surface modification has been ascribed to nano islands of PrOx that can precipitate out of praseodymium-based thin films[81]. Since Ce and Pr are located adjacent to each other in the lanthanide series, they share similar size and electronic structure. Previous attempts at doping Pr into Ce have claimed a limited solid solubility. Others have shown complete solid solubility. The current work has demonstrated solid solubility. However similar in size, there are still significant changes in material properties that occur throughout the solid solution.

The first electrochemical work on praseodymium doped ceria traces back to the work of Takasu and Matsuda in the early 1980's[82]. The authors found a solubility limit of 70 mol% praseodymium in ceria and performed conductivity and transference number measurements displayed in Figure 49. The total conductivity increased with increasing praseodymium content. The main contribution was from the electrical conductivity as seen by the decreasing ionic transference number with increasing praseodymium content. Several groups have followed up that work with XRD and conductivity measurements, but

the data was inconsistent in magnitude of the conductivity, phase stability and trend in lattice parameter for increasing praseodymium concentration. Nauer et al observed secondary phases with 40 mol% doping, but mentioned that the Pr^{3+}/Pr^{4+} ratio may be dependent on cooling rate[83]. Shuk and Greenblatt found evidence of secondary phases as low as 30 mol% in XRD from powders made by a hydrothermal method[84]. They also mentioned the importance of thermal history. If a sample was quenched to room temperature, the lattice constant would increase with increasing Pr concentration. However, if the sample was heated to 850°C and slowly cool, the lattice constant would decrease. Stefanik studied the electrical properties of praseodymium doped ceria from 0 to 20 mol %[85]. In his fabrication of dense pellets for conductivity measurements, he found it difficult to fabricate without the presence of cracking on the surface. To minimize the cracking, he sintered the samples under vacuum, but small amount of cracking was still present[86]. The literature on the preparation of dense pellets of praseodymium doped ceria shows the difficulties in preparation for conductivity measurements.

Several different compositions of praseodymium doped ceria powders were fabricated in this work via a citric acid combustion method. Each of the powders was phase pure up until the 70 mol% doping, after which powder decomposed into two phases (the doped ceria and the pure praseodymium oxide). Several different methods were attempted to attain dense pellets for conductivity and transference number measurements. For each method, the pellet was pressed in a 13 mm die assembly to 5 tons (approximately 335 MPa). The first method was simply to fire in air up to 1500°C for 5 hours. However, even after that relatively high sintering temperature and long dwell time, the density was not sufficient for conductivity measurements, as shown in Figure 48a). Some of the pellets

were still intact after this firing schedule, while other samples showed cracking on the surface and through the bulk of the pellet. The cracking could be attributed to the large expansion that occurs with praseodymium-containing oxides. Stefanik mentioned in his dissertation that the PDC samples were fired in a vacuum to 1450°C to avoid the large volumetric changes at higher temperatures by effectively expanding the material at lower temperatures. With that in mind two additional methods were attempted: sintering in vacuum and sintering in a reducing atmosphere. Using a vacuum tube furnace, the samples were pumped down to a rough vacuum and then heated up in a continuous vacuum to 1400°C. Unfortunately, the pure alumina tubes could not handle the temperature and pressure combination. The tubes would deform and open cracks letting air rush in at the highest temperature dwell stage. The pellets from that firing also exhibited the same cracking morphologies. The second method was to fire the pellets in a reducing condition. For this, the same vacuum tube furnace was used with a new alumina tube. After removing the oxygen with the rough pump, the pump was disconnected from the system and 10% hydrogen in argon was backfilled into the tube. After a slight positive pressure was attained, the reducing gas valve was opened and the outlet gas passed through an oil bubbler. This allowed constant flow of the reducing gas throughout the sintering. After firing to 1400°C for 5 hours, the praseodymium pellets did appear dense but were completely green, as shown in Figure 48 b). The green color comes from the Pr^{3+} state, which coincides with the green crystals of commercially available praseodymium (III)

nitrate. The reduced pellets were then allowed to slowly oxidize at room temperature over a few days, but unfortunately also cracked into unusable pieces.

Figure 48. Images of a) 30PDC fired to 1500°C for 5 hours taken in SEM and b) praseodymium oxide fired under reducing conditions to 1400°C.

With these fabrication challenges, it was decided to rely on literature values for the total conductivity and ionic transference number measurements, which were taken from Takasu and Matsuda and are shown in Figure 49[82]. The previous literature provides conductivity data in the composition and temperature range studied in the current work. Because the data in the paper was only represented in graphical format, it was necessary to use a program that translate the image into tabular data that can be used in the current analysis. To accomplish that data collection, the web program WebPlotDigitizer was used[87]. WebPlotDigitizer is a web app built in HTML5 that can be run from a browser without any software download. The process is as follows:

a)

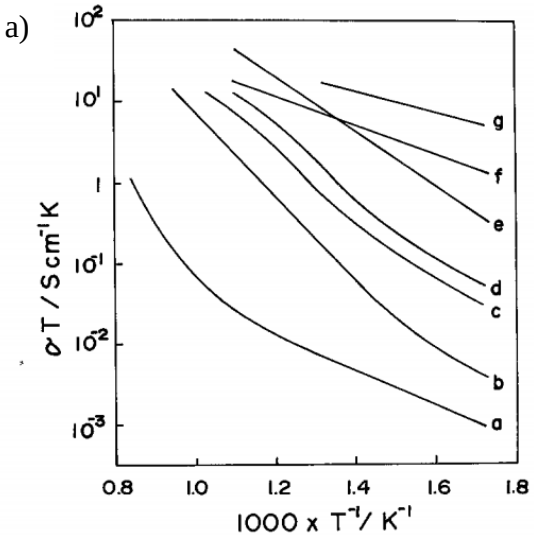

Fig. 2. Variation of conductivity in 0.21 atm of oxygen with reciprocal temperature for the $Ce_xPr_{1-x}O_2$ system. The value of x; a:1, b: 0.9, c: 0.8, d: 0.7, e: 0.6, f: 0.5, g: 0.3.

b)

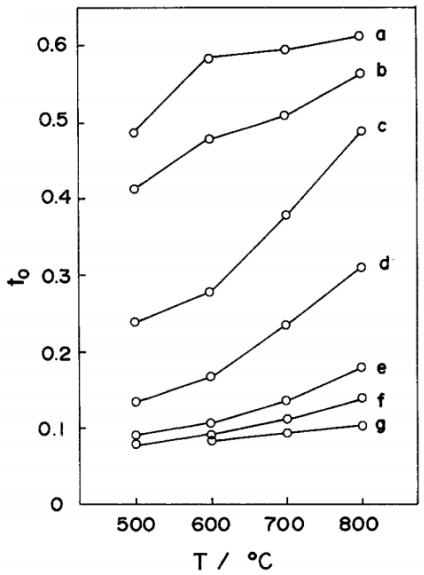

Fig. 3. Ionic transference number of the $Ce_xPr_{1-x}O_2$ system as a function of temperature. The value of x; a: 1, b: 0.9, c: 0.8, d: 0.7, e: 0.6, f: 0.5, g: 0.3.

Figure 49. The a) conductivity as a function of doping concentration and temperature and b) the ionic transference number as a function of dopant concentration and temperature[82].

1. Upload an image of the figure with any accepted file format (JPEG, PNG, BMP, GIF). I generated a .PNG file by taking a screen shot of the plot.
2. Calibrate the axes via the straightforward instructions on the website. All that is required is two known points on the X-axis and two known points on the Y-axis. After choosing the points, the values were entered in the dialog box. For the conductivity plot, I selected the log option for the y-axis in the conductivity plot. I checked the accuracy of the axes by moving the cursor around the map and making sure the cursor values matched the expected values.
3. Choose “Automatic Mode” and select “Pen” to trace the conductivity lines. You are able to vary the width of the pen with a bar in the top of the page. I used different widths depending on how close the lines were. I selected black as the “Foreground Color” because it was the color of the data in the plot.

4. Then I used the “Averaging Window” algorithm with different Px values until I found a desirable fit to the data.
5. The data was then copied into Excel and used for the comparison of performance to conductivity and ionic transference numbers.

5.2 X-ray Diffraction of Ceria and Doped Ceria

Powders of ceria with varying dopant levels of praseodymium were synthesized using the citric acid method. Stoichoimetric amounts of praseodymium nitrate hexahydrate and cerium (III) nitrate hexahydrate were dissolved in deionized water to yield the desired molarity solution. Citric acid was used a chelating agent with a 1:1 molar ratio of citric acid to metal cations. Ammonium nitrate was used to maintain a 1:1 fuel to oxidizer ratio for ideal combustion[88]. The solution was heated on a hot plate until the water boiled off and the solution turned into a foam. The foam would then smoulder and leave behind fine, homogenous powders that were then calcined at 800°C for two hours.

X-ray diffraction was used to identify the phase formation of the doped and undoped ceria. Ceria and praseodymia take on a fluorite crystal structure with 0.4% difference in ionic radius and as such should have high solid solubility across the doping concentrations. The spectra for the doped and undoped powders are shown in Figure 50. The peaks for pure praseodymia match to PDF card 00-042-1121 for Pr_6O_{11} and the peaks for pure ceria match to PDF card 00-004-0593 for CeO_2. Solid solubility of praseodymium in ceria is demonstrated up to 70 mol% praseodymium. This is consistent with previous XRD characterization of the Pr-Ce system[82]. Above 70 mol%, a secondary peak associated with praseodymium oxide is present as seen in Figure 50 b). The slight shift

a)

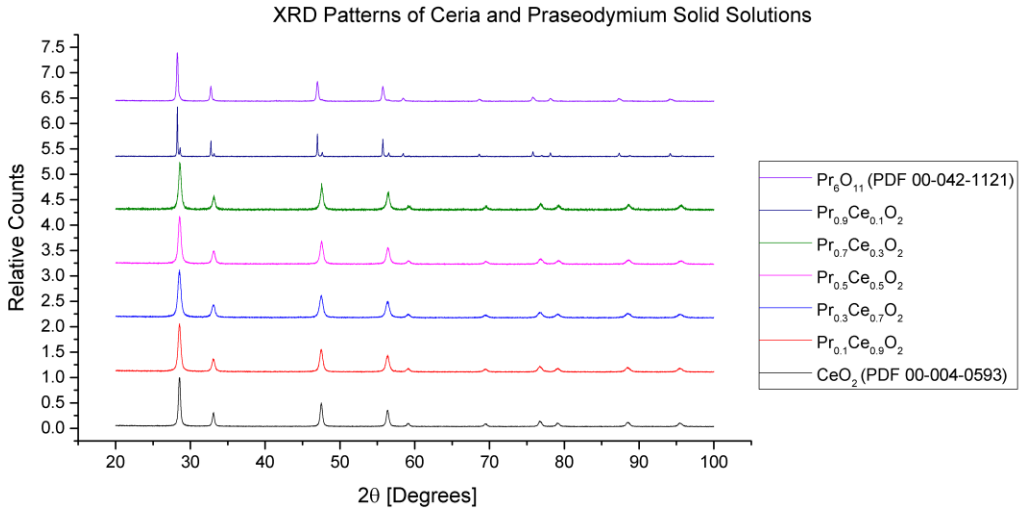

b)

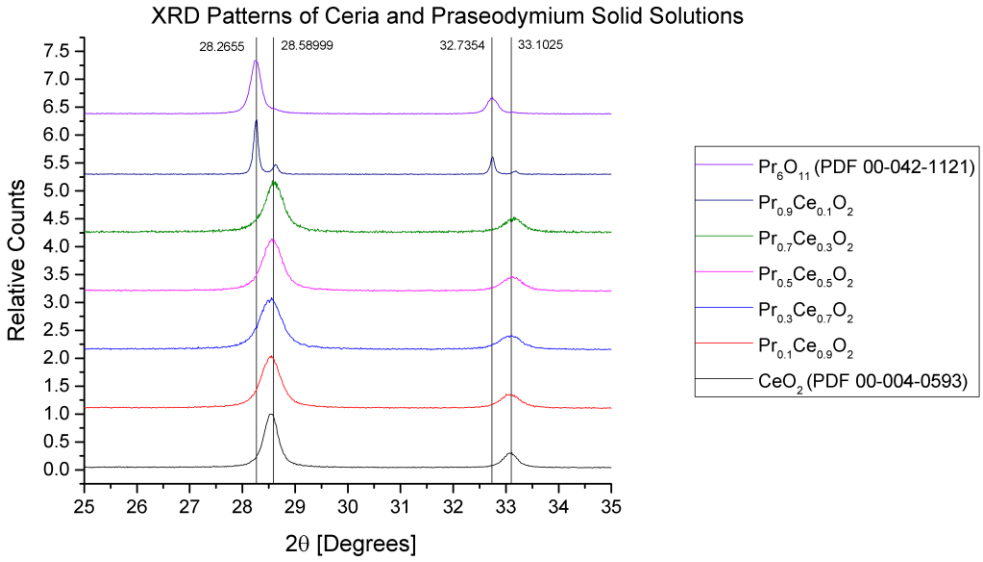

Figure 50. XRD patterns of praseodymium doped ceria a) over the whole 2θ range and b) zoomed in on the first two major peaks.

towards the lower 2θ values is consistent with the smaller ionic radius of praseodymium versus the cerium cation. The peaks for all powders show a relatively large full-width at half-max which is consistent with a broadening that is expected with smaller particles sizes made via the citric acid method.

5.3 Varying Molarity

The praseodymium nitrate solution was infiltrated into the porous LSCF cathode at varying molarities to identify effects on performance. It has been demonstrated that molarity and a number of other factors influence final coating ability of the infiltrant[30]. The viscosity of solutions will increase with increasing molarity and may have trouble infiltrating into the porous cathode. Many solutions in the literature use less than 1M concentration, which may be due to the difficulty in infiltrating solutions with slightly higher viscosity. In this work, the molarity was varied from 0.1 to 2.0 M. Figure 51 shows the morphology changes due to the changes in concentration of the infiltrated solution with a) showing the LSCF backbone without any infiltration. Figure 51 c) and d) shows the change from an isolated island morphology to a more conformal morphology with increasing molarity. Typically, an isolated island morphology is thought to be more desirable because of the increase in surface area relative to a conformal coating. However, as shown in Figure 52, the polarization resistance decreased with increasing molarity. For the praseodymium infiltration, any coating increased ORR performance with the highest molarity solution showing the largest improvement. The activation energy of the for the reference symmetric cell is 1.95 eV while that of the infiltrated praseodymium was slightly lower. The 2M praseodymium oxide infiltrated solution showed the lowest activation energy of about 1.7 eV.

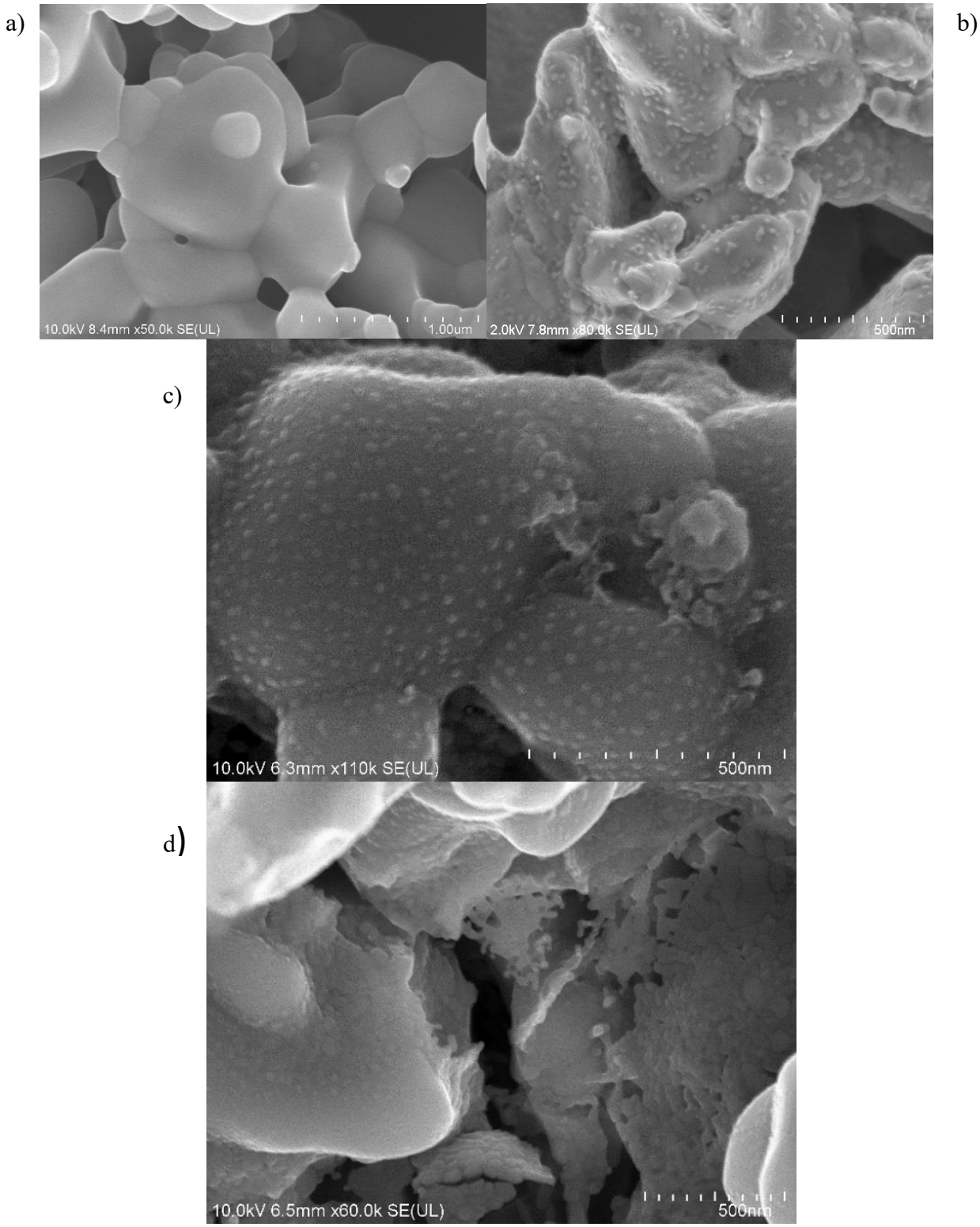

Figure 51. SEM images of a) LSCF backbone without infiltration b) backbone with 0.1M praseodymium nitrate c) backbone with 1.0 M praseodymium nitrate and d) backbone with 2.0M praseodymium nitrate.

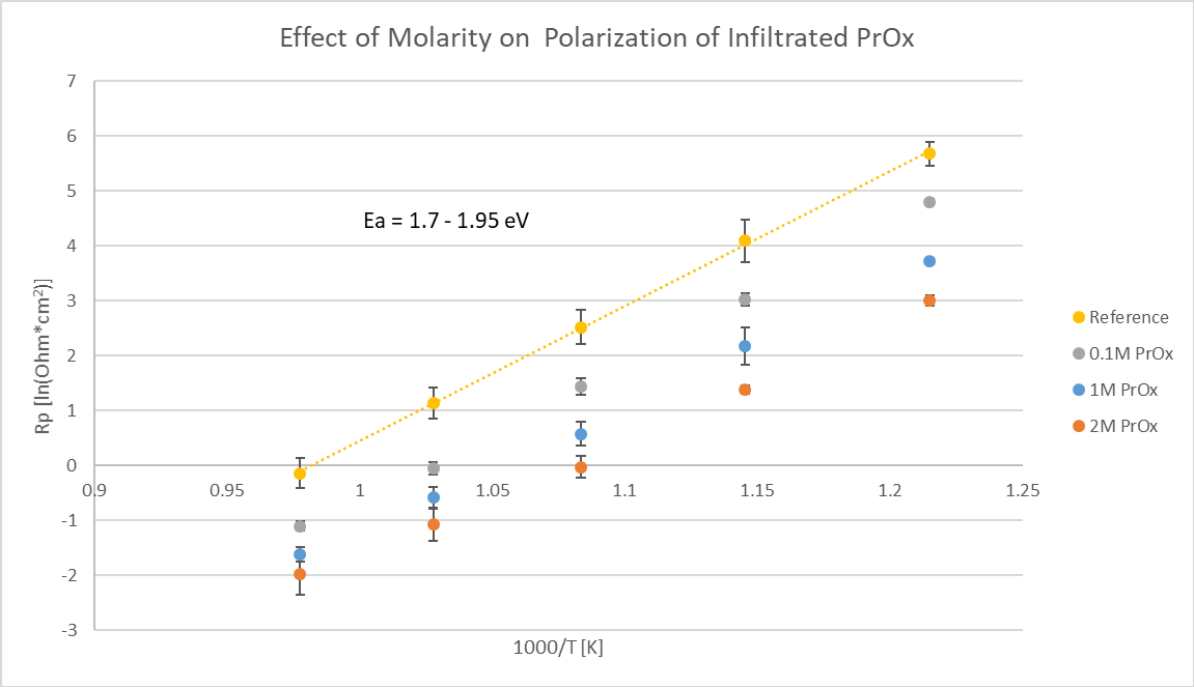

Figure 52. The variation in polarization resistance for varying concentrations of praseodymium nitrate infiltrated solutions. The error bars represent one standard deviation.

5.4 Infiltrated PDC

The performance increase associated with the infiltrated praseodymium oxide demonstrates the possibility for improvement with the surface modification. However, it is difficult to pinpoint the exact characteristic of the praseodymium oxide that provided the enhanced performance. A better way to gain understanding is to isolate a single host material with a given crystal structure and morphology and modify the properties through doping. The cerium-praseodymium system provides a great case due to the large changes in electronic and ionic conductivity while only varying the doping concentration.

Figure 53 shows how the polarization resistance varies with doping concentration of praseodymium in ceria. Notice that the undoped ceria shows a slight increase in resistance and that the resistance decrease with increasing praseodymium content. However, after 50 mol% praseodymium, the polarization resistance increases with increasing praseodymium content. The 50PDC proved even better than the undoped praseodymium, which has demonstrated high performance on its own. The 90 mol % praseodymium was not infiltrated because of the previous XRD result that showed phase separation about 70 mol % Pr. Also note that the activation energy of the 50 PDC is slightly lower than the activation energy for the LSCF reference (1.95 vs 1.7 eV). The optimal doping concentration results in approximately two orders of magnitude decrease in polarization resistance. Now that there is a clearly identified optimal solution, it is important to identify key characteristics of that composition that lead to the enhanced performance.

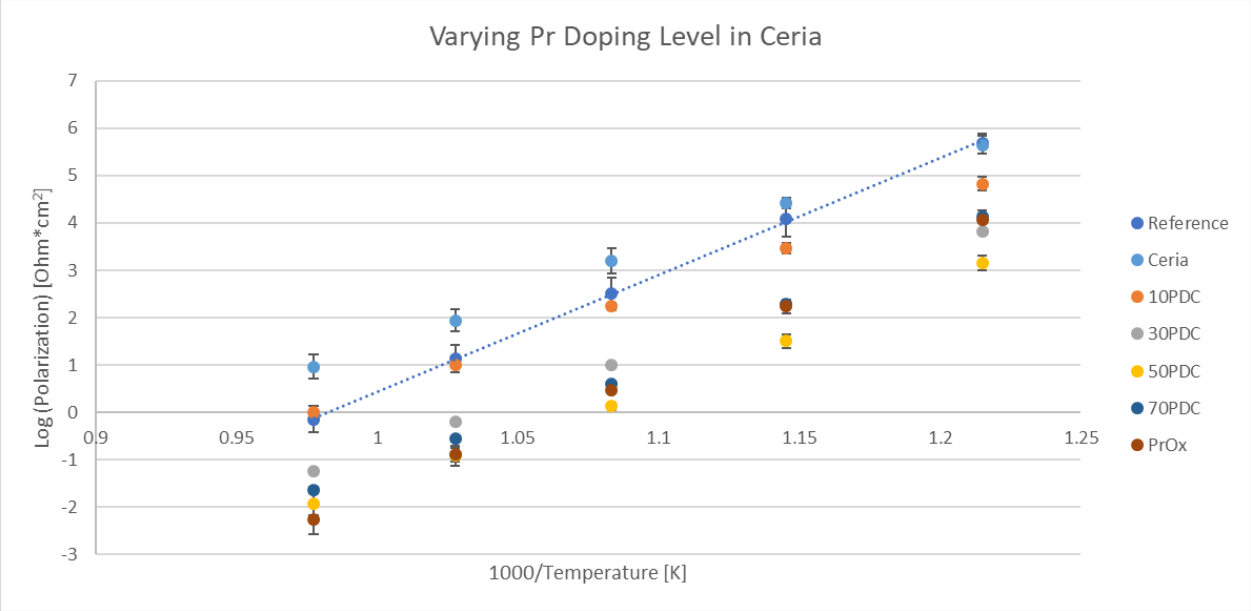

Figure 53. The variation in polarization resistance as a function of praseodymium doping concentration from 550 to 750°C

5.5 Ionic/Electronic Conductivity of PDC

As shown previously in Figure 49, increasing praseodymium concentration increases the ionic and electronic conductivity and decreases the ionic transference number. Figure 54 shows how the polarization resistance varies with ionic conductivity of the praseodymium doped ceria solid solutions. Each dopant level shows four or five points which represent different temperatures ranging from 550 to 750°C. The polarization resistance decreases with increasing temperature so the points toward the bottom of the plot for a given material are the higher temperatures. For the 30 PDC and the 50 PDC there is a similar trend of increasing ionic conductivity at higher temperatures. However, the 70 PDC shows very little change in ionic conductivity with temperature. Another important take-away is the that increasing the ionic conductivity does not correlate to uniform decrease in polarization resistance. It appears that above 50 PDC, further increasing the ionic conductivity does not yield better performance. This is contrary to the rule of thumb that simply increasing ionic conductivity of the infiltrated solution will yield lower polarization resistance.

Figure 55 demonstrates the correlation between electronic conductivity and polarization resistance for 30, 50 and 70 PDC. Similar to the previous figure describing ionic conductivity, the polarization resistance does not directly correlate with performance. For the 30 PDC, there is a minor change in electronic conductivity with temperature with a slight increase in conductivity at higher temperatures. On the other hand, both 50 PDC and 70 PDC show decreasing electronic conductivity as temperature increases. Again, increasing the electronic conductivity from 50PDC to 70 PDC does not result in any further performance increases.

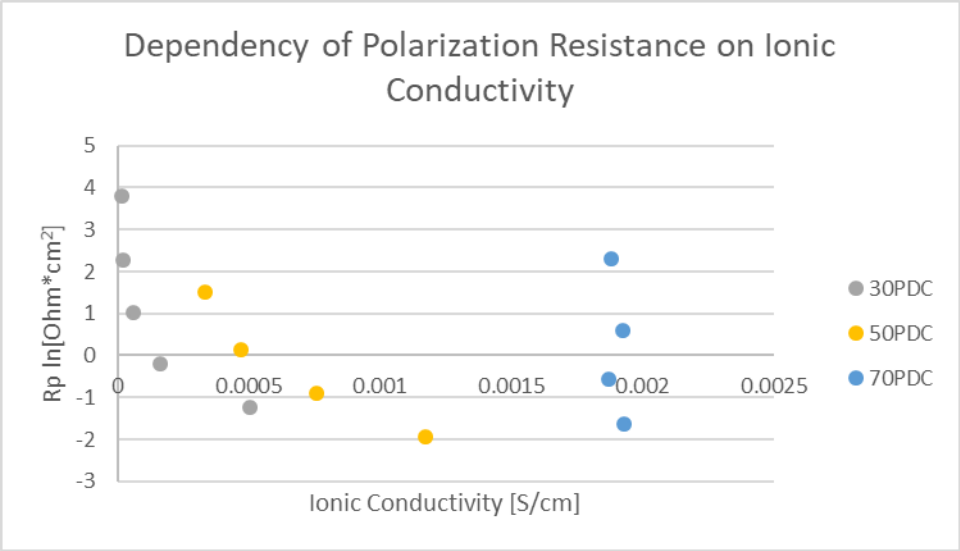

Figure 54. Polarization resistance as a function of ionic conductivity for 30, 50 and 70 PDC. Each composition has several points which indicate different operating temperatures.

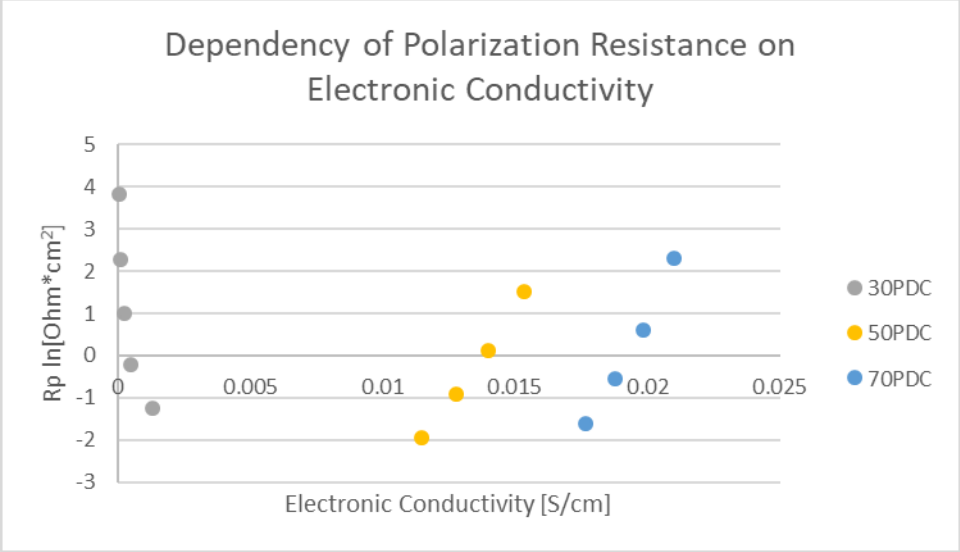

Figure 55. Polarization resistance as a function of electronic conductivity for 30, 50 and 70 PDC. Each composition has several points which indicate different operating temperatures.

5.6 XPS of Prasedoymium doped Ceria

In order to better understand the effect of the infiltrated praseodymium doped ceria coating, the powder samples were characterized with X-ray photoelectron spectroscopy. Since ceria is an active catalyst by itself, the Ce 3d spectra was first explored to help explain the difference in performance for the PDC infiltrated samples. If undoped ceria shows excellent catalytic activity, then any dopants that increase activity may be interacting with the cerium.

5.6.1 Ceria

In this work, XPS is used to monitor the oxidation state of cerium. Ceria has been widely studied in many catalytic applications due to its redox properties under different operating conditions. More specifically, the catalytic ability is often ascribed to the 3+/4+ redox couple in ceria. The hybridization that occurs between the 4f cerium and the oxygen 2p allows for unique electrochemical properties. However, this hybridization makes interpretation of the cerium 3d spectra nontrivial. In most cases, one or two peaks are associated with a given element. For cerium, there are multiple peaks associated with the 3+ and 4+ states and the peak heights are not linearly dependent on the concentration of either the Ce^{3+} or Ce^{4+}.

Previous X-ray photoelectron work by Burroughs et al and by Romeo et al have associated 10 peaks with the cerium $3d_{5/2}$ and $3d_{3/2}$ as shown in Table 4[89], [90]. Following their interpretation, the v, v'', and v''' are attributed to CeO_2. The v and v'' are due to a mixture of $(5d6s)^0\ 4f^2\ O2p^4$ and $(5d6s)^0\ 4f^1\ O2p^5$ configurations and the v''' is for the $(5d6s)^0\ 4f^0\ O2p^6$ final state. The v_0 and v' are a combination of the $(5d6s)^0\ 4f^2\ O2p^4$

and $(5d6s)^0\ 4f^1\ O2p^5$ for Ce_2O_3. Each of those peaks also correspond to the cerium $3d_{3/2}$ (designated with a u) due to the spin orbital coupling. In practice, the v_0 and u_0 are difficult to identify because the energy separation from other peaks is not large.

The purpose of the deconvolution of the cerium peaks is to identify the amount of Ce^{3+} which acts as a proxy for the vacancy concentration since the reduction of ceria requires an oxygen vacancy to maintain electroneutrality. However, quantitatively determining the defect concentration is not as straight forward as taking the ratio of the 3+ to 4+ peaks. As the CeO_2 is reduced to Ce_2O_3, it would be expected that the u''' peak will decrease because there is no $4f^0$ structure is Ce_2O_3 and that the u' peak would increase[90]. However, in practice, the u' increases before any decrease is seen in u''' due to changes in the hybridization. The u''' peak, as mentioned before, comes from the hybridization of the cerium 4f with the oxygen 2p: $(5d6s)^0\ 4f^0\ O2p^6$. Because there is no $4f^0$ in Ce_2O_3, the hybridization will decrease with more reduction. However, Kotani et al showed that a decrease in the hybridization actually results in an increase of the $4f^0$ contribution[91].While there are less $4f^0$ states as ceria is reduced, the increase in intensity offsets some of that change. Allahgholi et al have recently reinvestigated the linear dependence on the u''' peak and found it to be useful after a correlation for Ce^{3+} plasmon satellite peaks[92]. Also, XPS requires an ultra-high vacuum environment, which may alter some of the spectra when left under those conditions for long time durations[93]. However, all the XPS data collected in this work was done with minimal time in the UHV conditions meaning all XPS experiments were conducted in less than 5 hour runs.

An estimation of the Ce^{3+} to Ce^{4+} ratio is typically obtained from a ratio of the integrated area of the Ce^{3+} peaks (v^0, v', u^0, u') to the sum of the integrated areas for all 3+ and 4+ peaks[78], [94], [95]. In other words, the ceria oxidation state is estimated from a linear combination of the 3+ and 4+ spectra. The 3+ and 4+ reference spectra were taken from Thermo Avantage software XPS Knowledge Base and are shown in Figure 56[96]. The reference spectra were compared to commercial powders of CeO_2 and $CePO_4$ and found to accurately measure the 4+ and 3+ valence of cerium. The peak fitting for the 3+ and 4+ reference cases performed with the following constraints: spin orbit coupling of ~18.45 eV with a fixed ratio of 1.5 (3d(5/2) : 3d(3/2) ratio). All spectra with any 4+ character were corrected to the u''' (Ce 3d3/2) peak at 916.7 eV.

The fitting of the Ce 3d spectra for the praseodymium doped ceria was done using Thermo Avantage software. The spectra under consideration was first charge shifted using the v''' peak as the reference at 916.70eV since all the powders had significant 4+ character. The peaks were then fit using a Shirley background and the Ce^{4+} and Ce^{3+} reference spectra in the Thermo Avantage software, which are taken from synchrotron measurements by Beche et al[97]. The Shirley method is an iterative background subtraction technique that uses area under the curves to compute the background.

The Ce 3d spectra for PDC of varying dopants are shown in Figure 57. From that figure, the 10, 30, 50 and 70 PDC all show nearly identical features. Since overall Ce signal for each of the samples corresponds with the amount of cerium present, samples with lower cerium content will have a lower signal to noise ratio. The important features to note in comparing the features are changes in the relative intensities of peaks, which are indicative of differing amounts of Ce^{4+} to Ce^{3+}.

Table 4. Peaks associated with the cerium 3d spectra characterized through X-ray photoelectron spectroscopy.

Peak	Cerium Oxidation State	Literature Values[90]	
		Binding Energy (eV)	HWHM
v_0	+3	880.6	0.9
v	+4	882.60	0.9
v'	+3	885.45	1.40
v''	+4	888.85	1.54
v'''	+4	898.40	0.9
u_0	+3	898.4	0.9
u	+4	901.05	1.00
u'	+3	904.05	1.41
u''	+4	907.45	1.53
u'''	+4	916.70	1.00

In this case, the Ce^{4+} shows nearly 100% of the total area of the curves for each of the powders. A representative spectra for the XPS fit is shown for the $Pr_{0.10}Ce_{0.9}O_2$ in Figure 58. Note that the fit completely dominated by the Ce^{4+} spectra. The quantitative values calculated from the ratio of the total areas of the Ce 3+ and 4+ peaks revealed greater than 98% 4+ character, which was essentially 100% given the few percentage point variance with multiple sample batches.

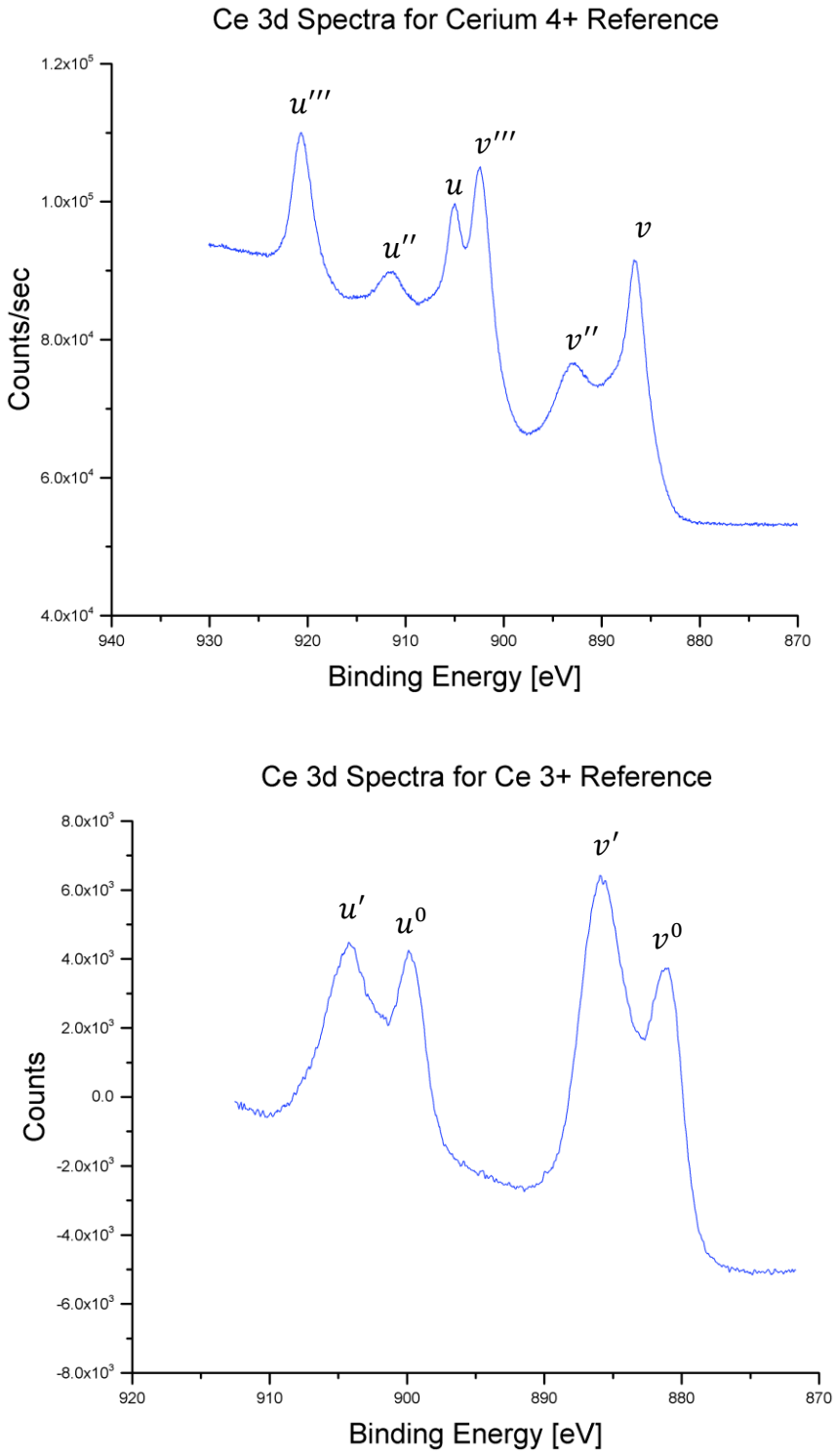

Figure 56. Reference XPS spectra for Ce 4+ and Ce 3+ taken from data files in the Thermo Avantage XPS software used to acquire the data.

XPS spectra in general often rely on very nuanced changes in the spectra to make conclusions. It may be tempting to try and draw conclusions from the XPS spectra in Figure 57. For example, there are some slight differences in peak height for the two peaks in the between 900 and 910 eV for the 50PDC and 70 PDC. However, much of the fitting and interpretation is based on ratios of peak heights within a given reference spectra. In other words, because each material only displays 4+ spectra, all of the peak heights are expected to be consistent or rather the ratios of peak heights should be constant. So while there are a few differences in peak height or peak shape around the 4+ spectra for each dopant level, those differences are most likely due to minor variations in the lab scale XPS system and the variations inherent in changing the concentration of cerium in each sample. Each of the spectra in Figure 57 contain different amounts of cerium and are all normalized by peak with a binding energy of ~920 eV.

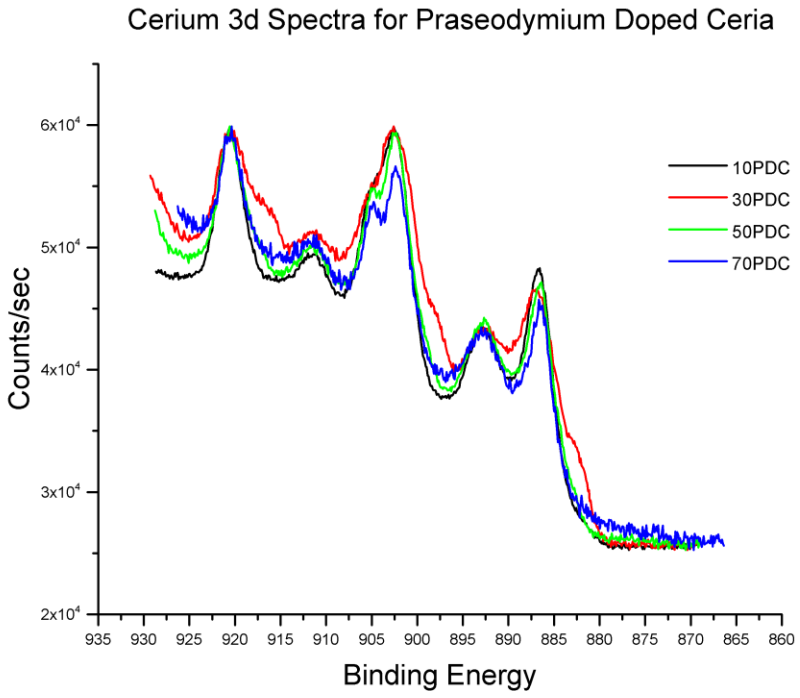

Figure 57. The Ce 3d XPS spectra for praseodymium doped ceria at varying dopant levels taken from the infiltrated samples.

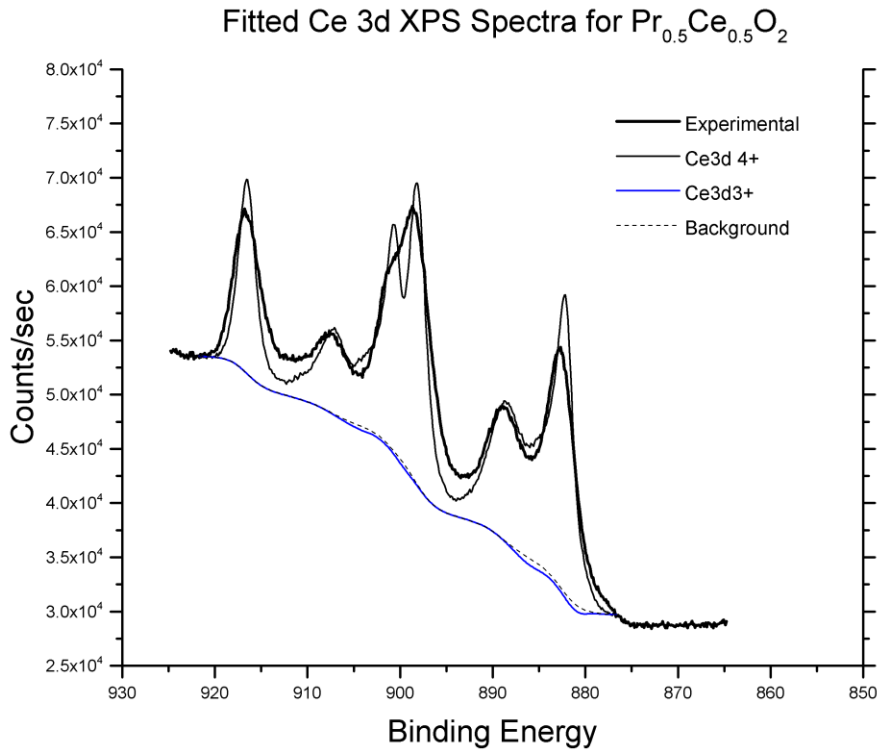

Figure 58. The fitted XPS Ce 3d spectra for 50 mol% praseodymium-doped ceria. Note the spectra is nearly 100% Ce^{4+}.

5.6.2 Praseodymium

The literature on Pr 3d spectra is not as well estalbished as the Ce 3d spectra. However, there are several examples in the literature of peak deconvolution to determine oxidation states**[98], [99]**.The Pr 3d spectra has three spin-orbit doublets that characterize the main peaks that are labelled 3d5/2 ($\boldsymbol{a}, \boldsymbol{a}', \boldsymbol{a}''$) and 3d3/2 ($\boldsymbol{b}, \boldsymbol{b}', \boldsymbol{b}''$). There are two additional minor features including a peak labelled $\boldsymbol{t}$ that is a result of a multiplet effect and an Auger peak for oxygen above 970 eV binding energy. In this work, the oxygen Auger peak is not present because the upper limit of the scan was 970 eV. Examples of

comparable Pr 3d spectra are shown in Figure 59. The spectra are shown as an example of the peak fitting, but note that they use different naming conventions.

Table 5 shows the peaks associated with the Pr 3d spectra used in this work. The fitting for this work is based off of the process outlined by Borchet et al. The spin-orbit splitting between the a/b doublets and the a''/b'' doublets should be 20.40 eV. The ratio of a''/b'' was set to 2/3 and the ratio for a/b and a'/b' were set to 0.58, which provided a better fit for the data in their work and in this work. In order to do any sort of semi-qualitative comparison between oxidation states of Pr, it is imperative to track certain features that are present in only the Pr^{3+} or Pr^{4+}, but not in both. Ogasawara showed that the a''/b'' doublet is absent in the Pr_2O_3 spectra, which means that peak will guide the interpretation of the oxidation state in the mixed 3+/4+ samples[100]. Sinev et al demonstrated that a completely oxidized praseodymium oxide sample (i.e. almost exclusively 4+), the ratio between the a''/a' was about 0.28. Thus, the oxidation state of Pr can be estimated according to[98]:

$$\frac{[Pr^{3+}]}{[Pr^{3+} + Pr^{4+}]} = 1 - \frac{1}{0.28}\frac{area(a'')}{area(a')} \qquad \textbf{Eq 28}$$

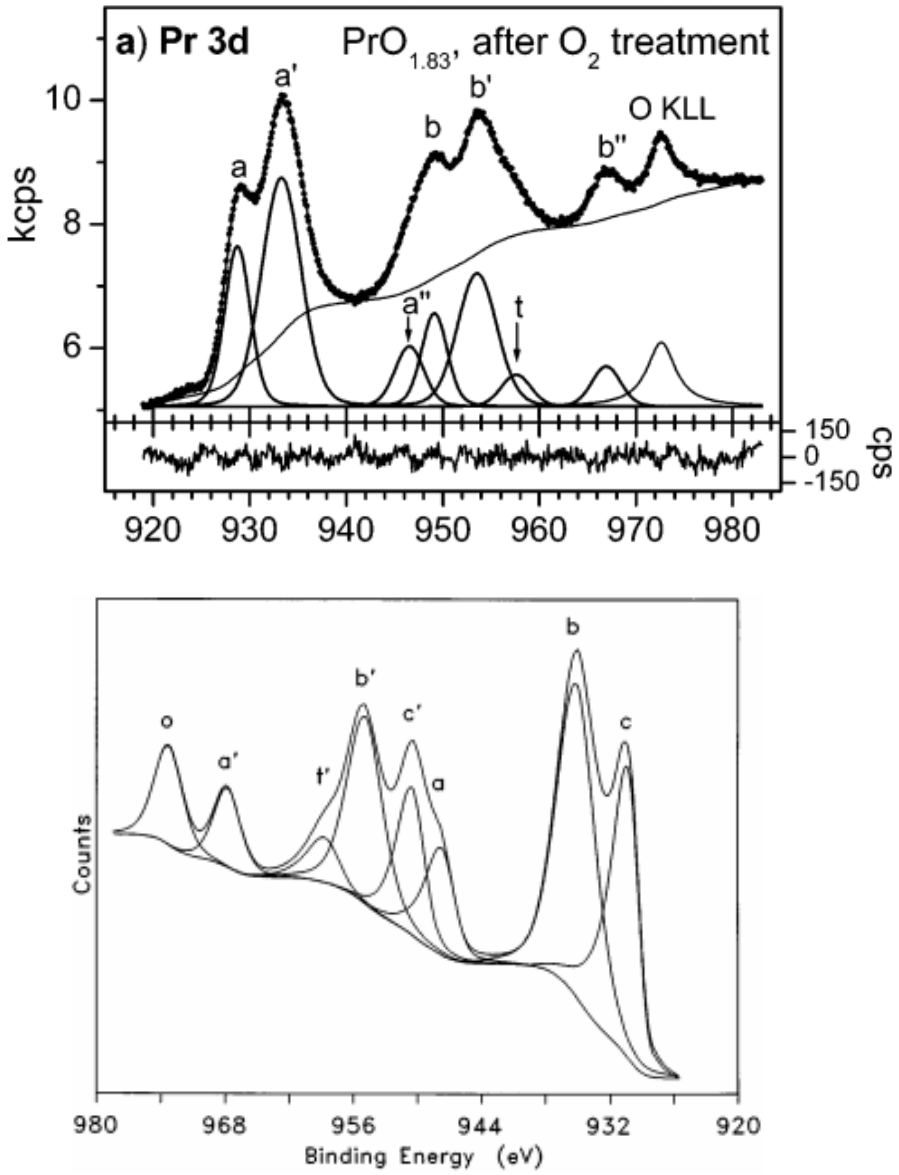

Figure 59. Two reference Pr 3d XPS spectra taken from literature that identify the relevant praseodymium peaks. Note that the x-axis is binding energy, but one is descending and the other ascending. Also note the naming convention is not the same between the two [98], [99].

Table 5. Peaks associated with Pr 3d spectra

Peak		Binding Energy	
		Reference[98]	**This Work**
3d5/2	a	928.7	928.67
	a'	933.3	933.27
	a''	946.5	945.62
3d3/2	b	949.1	948.74
	b'	953.6	953.40
	b''	966.9	966.17
Multiplet	t	957.6	957.49

Using the previously described software and fitting process, the ratio of Pr 4+/3+ was calculated for each of the praseodymium doped ceria compositions. With less peaks to worry about during fitting, it is more straightforward than the Ce 3d spectra. Figure 60 shows an example fit for the 10 PDC composition. The large peak below 920 eV is the last peak associated with the Ce 3d spectra. Figure 61 compares the Pr 3+/4+ ratio for each composition of praseodymium doped ceria. The ratio increases to a maximum around 50 PDC and then decreases with the full praseodymium oxide. While it may be tempting to correlate the performance with the amount of Pr^{3+} present, the difference in the calculated ratios among the 30, 50 and 70 PDC is not significant enough to be confident that the Pr^{3+} is the deciding factor. The next section will explore the valence band characterized via XPS to identify important changes around the 50 PDC composition.

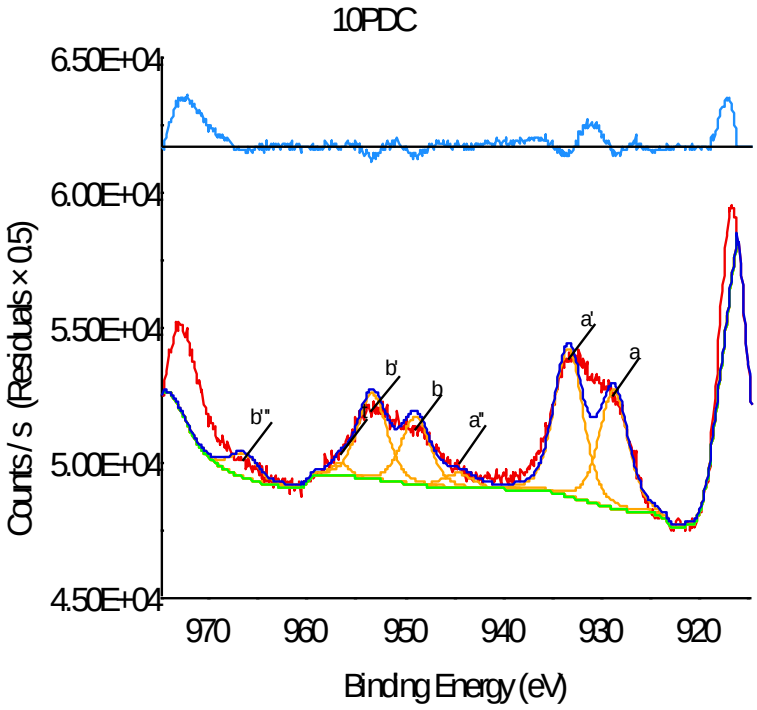

Figure 60. Fitting the Pr 3d spectra for the 10PDC composition.

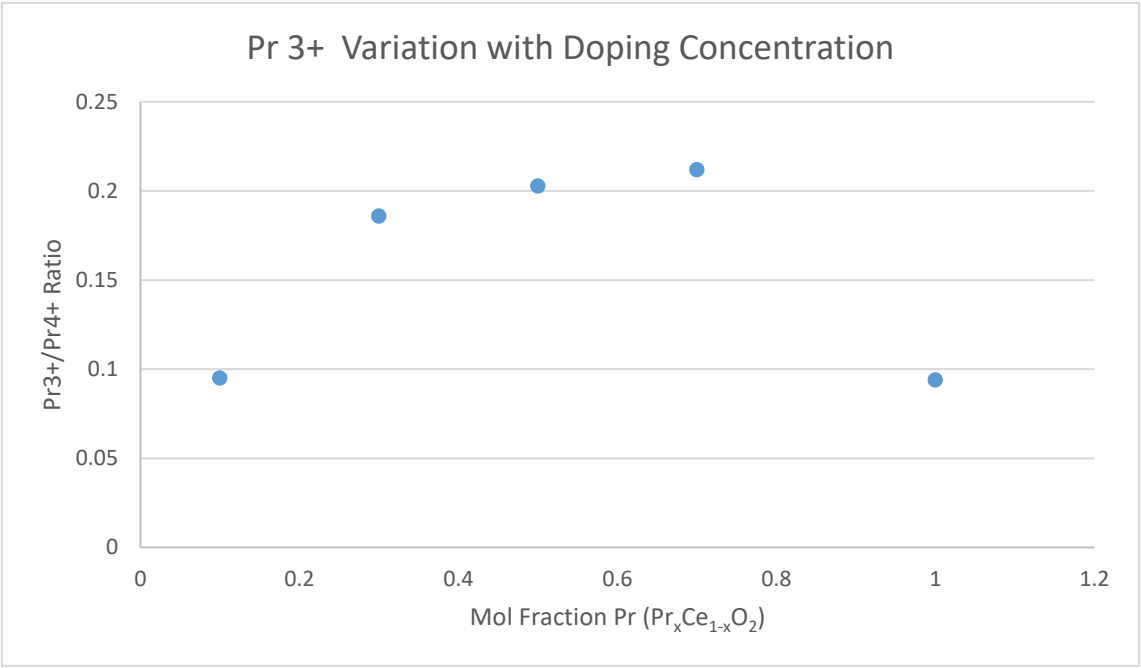

Figure 61. The variation in the Pr 3+/4+ ratio as a function of praseodymium content in the ceria host.

5.6.3 Valence band

Beyond the specific elemental characterization, XPS also provides insight into valence band. Because ORR is an electrochemical reaction, minor changes in the valence band of the surface species are likely to plan a large role in the performance. The valence band for XPS is evident at very small binding energies and can give information about the density of states and the relative distance from the Fermi level.

The valence band spectra for various levels of praseodymium doped ceria are given in Figure 62. All compositions show a similarly shaped spectra with a small peak between 0-10 eV and a larger peak at 15-30 eV. At first, there does not seem to be a definitive trend. It may be expected that increasing the doping concentration would shift the observed peaks closer to the Fermi level because of the increase in electrical conductivity observed with increasing praseodymium content. The spectra show no obvious shift from that perspective.

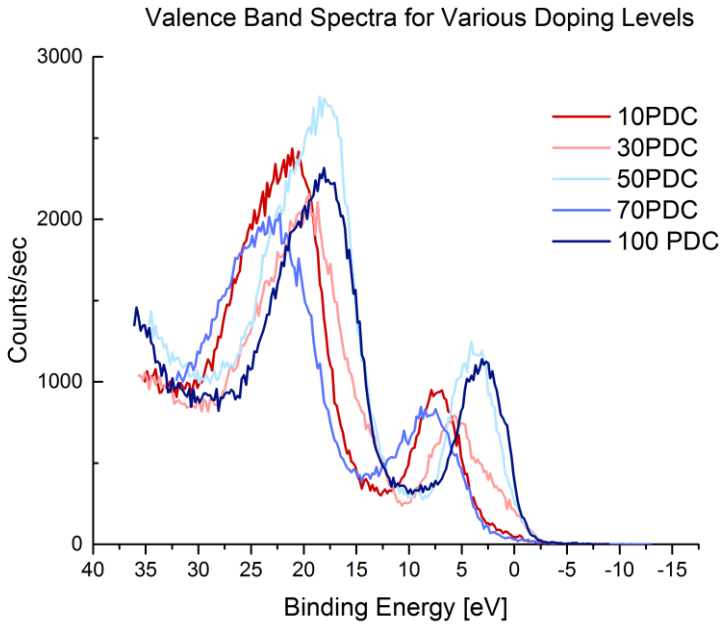

Figure 62. The valence band spectra for praseodymium doped ceria

However, plotting the peak heights and the peak binding energies versus mol % praseodymium brings out subtle changes that occur right at the 50 mol % praseodymium, where the maximum performance was found. Figure 63 shows valence band peaks and peak binding energy as a function of composition. Note that Peak A refers to the larger peak at high binding energies and Peak B refers to the peak at lower binding energies. In both plots, both peaks are plotted for completeness even though they demonstrate the same trend. In Figure 63 a), the general trend of valence band peak height suggests that 50 PDC should be the minimum value since the peak heights increase as composition both increase and decreases from the 50 mol % dopant level. However, 50 PDC shows the largest peak height for both peaks in the valence spectra. IN Figure 63 b), there is a somewhat similar trend with composition with valence band binding energy. In this case, 50 mol % is a local minimum, which translates into the smallest bandgap observed for the doped ceria. The undoped praseodymium also displayed an equally small bandgap, but in comparison to the 30 and 70PDC, the 50PDC had the lowest bandgap again correlating to the highest performance composition tested. The undoped praseodymium may have an equivalent band gap, but the other electrical properties that present in the mixed compositions allow for the higher performance.

The height of the valence band correlates to the density of states available near the Fermi level. Thus, the 50PDC composition showed the largest density of states. This could be due to an optimization in Pr/Ce mixing. When starting from pure praseodymium oxide you are decreasing the density of states as you increase the amount of cerium, except for the 50 mol% PDC composition. That composition could be unique because of the distribution of each component. At 50 mol %, there is the highest likelihood of a cerium

being adjacent to a praseodymium, which may be the important feature. Below 50 mol %, not every cerium may be next to a praseodymium cation. Above 50 mol%, the praseodymium-praseodymium neighbours may dominate the electrical behaviour. The benefit of adjacent praseodymium to cerium is described further with literature references in the discussion section.

The binding energy of the peak speaks to the distance from the Fermi level. The fact that the valence band is so close to the Fermi level (0 eV) for 50 PDC and pure praseodymia suggest metal-like electric structure. If the conductivity was more metallic, it would be expected that the conductivity would decrease with increasing temperature. While that was seen for the 50 PDC, there were no electrical measurements taken on the pure praseodymium oxide in the literature reference or in this work because of the difficulty in preparation of the pure praseodymium oxide dense, as previously mentioned. However, the 70PDC also showed a decrease in electronic conductivity with temperature, but did not show the small band gap. One explanation for this is that the conductivity was still polaron based (i.e. thermally activated), but any increase in conductivity was offset by the increasing Pr^{3+} that occurs. Remember that polaron hopping requires there to be a Pr^{4+} next to a Pr^{3+} for the electron to jump to. The 30, 50 and 70PDC all showed higher Pr^{3+} concentrations as shown in Figure 61.

a)

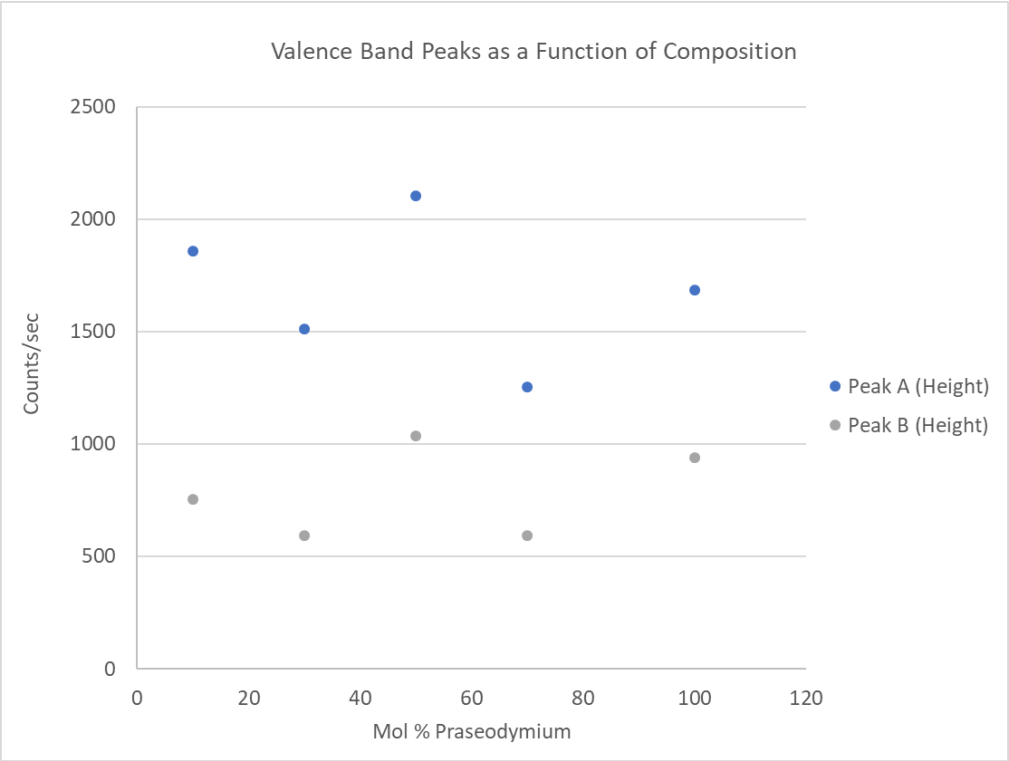

b)

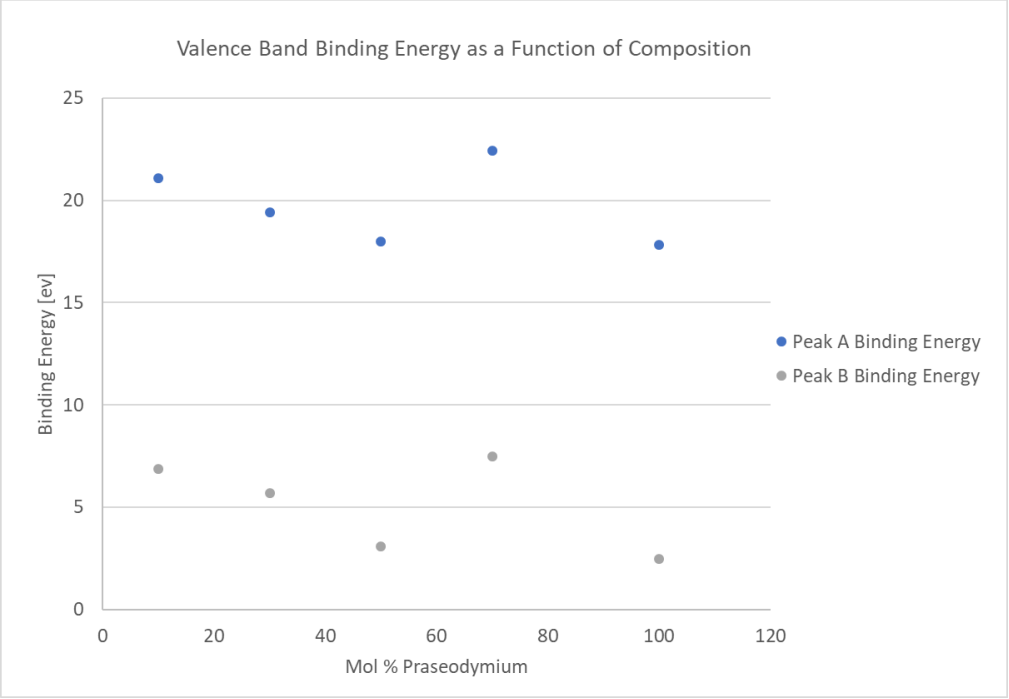

Figure 63. The valence band a) peaks and b) binding energy as a function of mol % praseodymium

While XPS is a powerful tool for surface characterization, the results may not be representative of the cerium and praseodymium at solid oxide fuel cell operating conditions. XPS characterization requires ultra high vacuum environment and is typically done at room temperature on the lab scale equipment. This obviously varies from the oxygen rich environment at 750°C that the cathode is exposed. This is especially important on the cathode side because the ORR properties and the oxidation state of ceria and praseodymia vary with temperature and partial pressure of oxygen. In order to gather more realistic data, it's possible to control the atmosphere and temperature using an ambient-pressure XPS. Unfortunately, the testing set up is very challenging and the X-ray source required is a synchrotron at a national facility like Argonne National Laboratory. Because national labs are user facilities, the preparation and execution of a single experiment is non-trivial. Thus it is more viable to find a lab scale technique that provide insight into the behaviour at more realistic operating conditions. One technique available is thermogravimetric analysis (TGA), which allows for control of the atmosphere and the temperature of a very sensitive mass balance. This means minor mass fluctuations can be tracked in real time in at a variety of temperatures. Particularly relevant for this material system is mass loss due to formation of oxygen vacancies.

5.7 TGA of PDC

One important characteristic of a cathode material is the behavior under temperature at a given partial pressure of oxygen. As temperature increases, the conductivity increase observed could be due to electronic or ionic defects. Typically, electronic compensation occurs at high pO_2 and low temperature, while ionic compensation occurs at low pO_2 and high temperatures. One method to probe this behavior is measuring the weight change that

occurs using thermogravimetric analysis. The TGA equipment is a highly sensitive mass balance that can be heated in a controlled atmosphere. Any reduction in praseodymium or cerium from 4+ to 3+ creates an effective negative site on the lattice. To maintain electroneutrality, oxygen must exit the lattice and in doing so leaves behind an oxygen vacancy, which is an effective positive charge on the lattice. With TGA, the mass and therefore the mols of oxygen lost can be tracked and then correlated to the degree of reduction. Eq 29 and Eq 30 describe the reduction and formation of an oxygen ion vacancy using Kroger-Vink notation.

$$2Pr_{Ce}^{x} + O_{O}^{O} \rightarrow 2Pr_{Ce}^{\prime} + V_{O}^{\cdot\cdot} + \frac{1}{2}O_2 \qquad \textbf{Eq 29}$$

$$2Ce_{Ce}^{x} + O_{O}^{O} \rightarrow 2Ce_{Ce}^{\prime} + V_{O}^{\cdot\cdot} + \frac{1}{2}O_2 \qquad \textbf{Eq 30}$$

For this experiment, the powders were fabricated using a citric acid combustion method where stoichiometric amounts of cerium (III) nitrate and praseodymium (III) nitrate were added to de-ionized water to attain a final solution concentration of 1M. Citric acid was used as a chelating agent and added to in a 1:1 molar ratio to the cations in solution. Ammonium nitrate was added to maintain a 1:1 fuel to oxidant ratio[88]. The solution was heated on a hot plate until the water evaporated and the citric acid smoldered leaving behind a small particle size powder. The powders were then calcined to 700°C for 2 hours. For the TGA measurement, a mass on the order of several milligrams was used. After equilibration at room temperature, the powders were heated to 1000°C at a ramp rate of 10°C/min in air.

The main metric followed in this experiment is the deviation in stoichiometry for the given composition. The deviation from nominal stoichiometry was calculated by dividing the mass loss at each temperature by the molar mass of oxygen and then normalizing by the number of moles of oxygen present at the beginning of the run. Figure 64 shows the non-stoichiometry of the powders as a function of temperature in an ambient air environment. The dotted box shows the temperature range used in the EIS testing of the symmetric cells for reference. As seen in this figure, there is a significant variation in nonstoichiometry with varying praseodymium content. Ceria and 10PDC shows very little change in oxygen content throughout the temperature range. Above 30PDC oxygen begins to leave the lattice around 200°C with 30PDC and 50PDC varying more or less linearly with temperature. At 70PDC there is a drastic increase in nonstoichiometry as the behavior also exactly mimics pure praseodymia with nearly 0.5 mol oxygen missing per mol praseodymium. The trend of increasing nonstoichiometry with increasing praseodymium ends with 90PDC. This can be explained by the phase separation that occurs above 70 mol% Pr in ceria as identified by XRD in previous sections. If the phases were completely separated, it would be expected that the nonstoichiometric behavior would be a linear combination of the ceria profile and the praseodymia profile. However, the behavior shows smaller than expected oxygen loss, which may be due to a detrimental feature of the combination of ceria, praseodymia and praseodymium-doped ceria phases in the powder. The praseodymium oxide reference also shows a large nonstoichiometry through 1000°C.

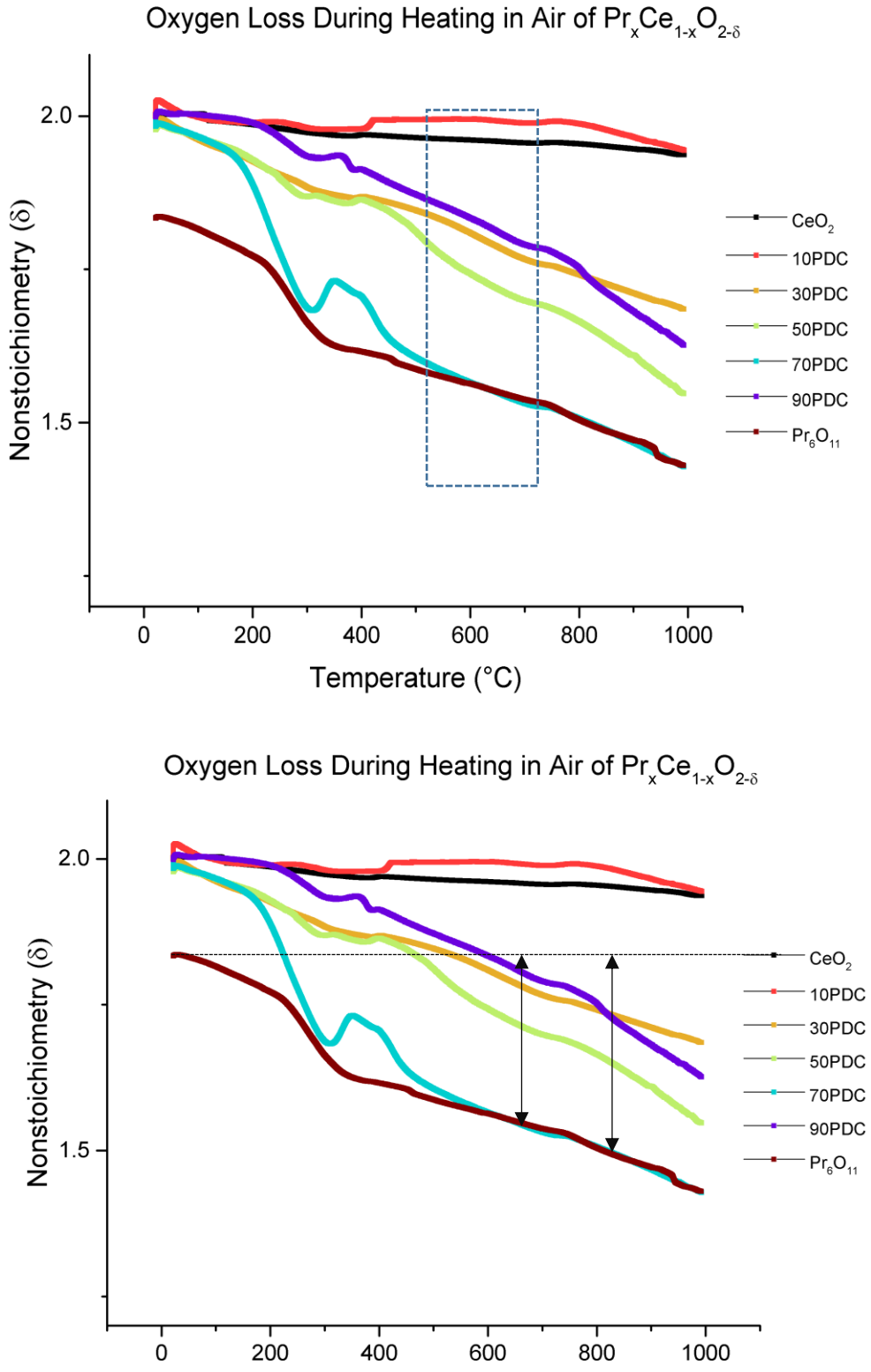

Figure 64. The a) nonstoichiometry of praseodymium-doped ceria powders as a function of temperature measured in air by TGA and b) the same plot showing the praseodymium oxide baseline used in the calculations. The dotted box shows the temperature range of the electrochemical testing (550-750°C).

Notice that the curve starts at a lower nonstoichiometry at the initial temperature than the doped ceria compounds. This is due to the inherent nonstoichiometry in praseodymium oxide. The thermodynamically stable compound is Pr_6O_{11}, or $PrO_{1.83}$ when normalized by Pr. Thus the starting point is at 1.83 on the y axis. The calculated oxygen loss was subtracted from 1.83 to generation that curve.

Further analysis of this plot reveals more subtle information about what is happening at these realistic operating conditions. In order to better understand what is occurring, it is valuable to normalize the oxygen loss to compare compounds with differing compositions. Figure 64 b) shows the amount of oxygen lost at specific temperatures for the pure praseodymia powder. The mols of oxygen lost at those given temperatures were normalized by the mol of praseodymium, which gave a benchmark value. Normalizing the mols oxygen lost per mol of praseodymium allows for comparison between different compositions of praseodymium doped ceria.

Table 6 compares the normalized oxygen loss per mol praseodymium for 30, 50 and 70 PDC. The first column $PrO_{1.83}$ shows the mols of oxygen lost per mol praseodymium and is the reference used to compare the other compositions. Under each composition is the expected mols of oxygen lost give the amount of praseodymium present. For the 30 PDC, the amount of oxygen lost would be expected to be 30% of the values of pure praseodymium. Likewise, it would be expected that the 50 PDC composition would show 50% of the mols of oxygen lost because only half the cations are praseodymium. The column labelled “Actual” is the calculated oxygen lost based on the TGA data. The column labelled “Ratio” is the Actual divided by the Expected. A number greater than 1 indicates that there is more reduction occurring than a linear combination of praseodymium and

cerium in their respective oxides. Each of the compounds show a greater oxygen loss than the expected. Looking at the ratios for each compound, there is a relative minimum for the 50PDC, where the optimal performance was found for the infiltrated samples.

As mentioned previously, to maintain charge neutrality, either the praseodymium or cerium must reduce for an oxygen vacancy to be generated (i.e. oxygen loss from the crystal lattice). Assuming any additional reduction that occurs beyond the expected value is attributed to cerium cations, two interesting points arise. First, it appears that praseodymium in the doped ceria lowers the activation barrier for the vacancy formation because of the increased concentration at a given temperature. Because undoped ceria showed insignificant mass change through the temperature range, there is a relatively large change in reduction behavior with the praseodymium in the system. Second, having a larger concentration of reduced cerium cations appears to negatively affect the ORR performance. Remember that 50 PDC showed the lowest polarization resistance. Reviewing Table 6, it

Table 6 Comparison of oxygen loss normalized per mol of praseodymium for 30, 50 and 70 PDC.

Normalized Oxygen Loss (Mol O_2 Lost per Pr)										
	$PrO_{1.83}$	30PDC			50PDC			70PDC		
	Mols O_2 Lost	Mols of O_2 Lost			Mols of O_2 Lost			Mols of O_2 Lost		
	Actual	Expected	Actual	Ratio	Expected	Actual	Ratio	Expected	Actual	Ratio
750°C	0.306	0.092	0.245	2.66	0.153	0.314	2.05	0.215	0.476	2.22
700°C	0.295	0.089	0.234	2.63	0.148	0.301	2.04	0.207	0.469	2.26
650°C	0.283	0.085	0.213	2.51	0.142	0.282	1.99	0.198	0.451	2.27
600°C	0.270	0.081	0.191	2.35	0.135	0.256	1.90	0.189	0.435	2.30
550°C	0.259	0.078	0.170	2.19	0.129	0.228	1.76	0.181	0.416	2.29
				Lower Ce^{4+}			Higher Ce^{4+}			Lower Ce^{4+}

is seen that 50 PDC had a lower normalized ratio of oxygen loss relative to the 30 and 70 PDC. In other words, both 30 and 70 PDC had a higher concentration of Ce^{3+} and presumably oxygen ion vacancies. A priori, the expectation is that increasing the oxygen ion vacancy concentration should correlate to increased performance. However, the opposite is seen here. The 50PDC shows a relatively lower Ce^{3+} concentration or rather a higher Ce^{4+} concentration than the 30 and 70 PDC.

5.8 Discussion

Gathering the data from the XPS and TGA, a picture starts to develop of the important features of the ORR behavior in the praseodymium-doped ceria system. The highest performing composition was the 50 mol % praseodymium doped ceria, despite the fact that 70PDC exhibits higher ionic and electronic conductivity. The goal was to characterize the system to pull out the features to the 50PDC. While the ceria XPS revealed very little, literature describes rich redox behavior dependent on oxygen partial pressure and operating temperature. The praseodymium XPS revealed some important information about the oxidation state of the PDC compounds. There was a trend of increasing Pr^{3+} content with a maximum around 50PDC. Unfortunately, the difference between the Pr^{3+}/Pr^{4+} ratio was insignificantly different between the 30, 50 and 70 PDC, so that alone cannot describe the ORR activity.

Put in the context of the TGA data allows for better understanding of the role of cerium in the praseodymium doped ceria system. The TGA data demonstrated first that 30, 50 and 70 PDC all lost more oxygen than expected on a per mol praseodymium basis. Since the XPS data suggested 30, 50 and 70 PDC all had approximately the same 3+ content,

then the additional oxygen loss had to have been accompanied by reduction in ceria from 4+ to 3+. However, the 50 PDC broke from the trend and showed a lower than expected ratio meaning a relatively higher concentration of Ce^{4+}. Thus, the availability of a cerium that can reduce may be important to the ORR activity. Furthermore, the valence band analysis suggests that the 50PDC has the highest density of states and a relatively small band gap. Putting those pieces of information together suggests that praseodymium helps create a series of energy levels between the valence and conduction band of the host cerium oxide. Literature on the praseodymium doped ceria system supports this hypothesis. Tuller's group has worked on the PDC system previously and published extensively on the absorption properties and correlating absorption spectra to Pr^{3+} and Pr^{4+} content. Tuller et al described an impurity band of state between the valence and conduction band for praseodymium dopants from 0 to 20 mol%[101]. Thus there is a point of maximum polaron hopping when there are equal numbers of Pr^{3+} an Pr^{4+} for the polaron to hop to. This suggests there is an optimal doping balance whereby too much 3+ would prevent polaron hopping. This 3+ could be in the Ce or the Pr. Remember that at 50PDC there was relatively more Ce^{4+} available, which correlates well with this theory.

Another perspective comes from Chatzichristodoulou and Hendriksen[102]. The authors attempt to fit an ideal solution defect model to the oxygen nonstoichiometry but are unable to reproduce the experimental results until they add an excess enthalpy term. In other words, the enthalpy of formation of oxygen vacancy formation varies with the amount of nonstiochiometry. A plot of excess enthalpy versus nonstoichiometry is hown in Figure 65. Although they focus on the smaller doping concentrations, the idea can be extended to the 30, 50 and 70 PDC compounds. From the TGA, 70 PDC shows much larger

nonstiochiometry and thus has a larger concentration of Ce^{3+}. In other words the Ce^{3+} is more thermodynamically stable and thus there must be a larger driving force required to create additional Ce^{3+} that are required for additional oxygen vacancy formation.

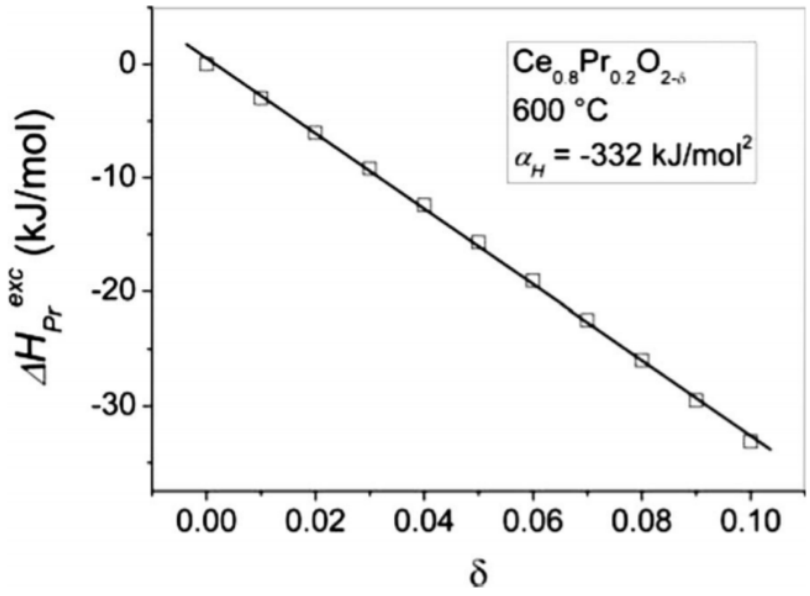

Figure 65. Excess enthalpy as a function of nonstiochiometry in the 20PDC system [102]

Ahn et al have provided further evidence to the claim that the praseodymium dopant lowers oxygen vacancy formation energy[103]. Using DFT, they demonstrated a lower oxygen vacancy formation energy with increasing doping content as shown in Figure 66. They went on to describe that as Pr^{4+} reduces, the larger Pr^{3+} distorts the lattice and creates opportunities for enhanced ionic conduction. This lattice expansion may also make it more difficult for the polaron hopping, which would explain the decrease in electronic conductivity for the 50 and 70 PDC with increasing temperature.

Through the experiments done in this work and in the context of the praseodymium-doped ceria literature, a better picture of the important government factors has been

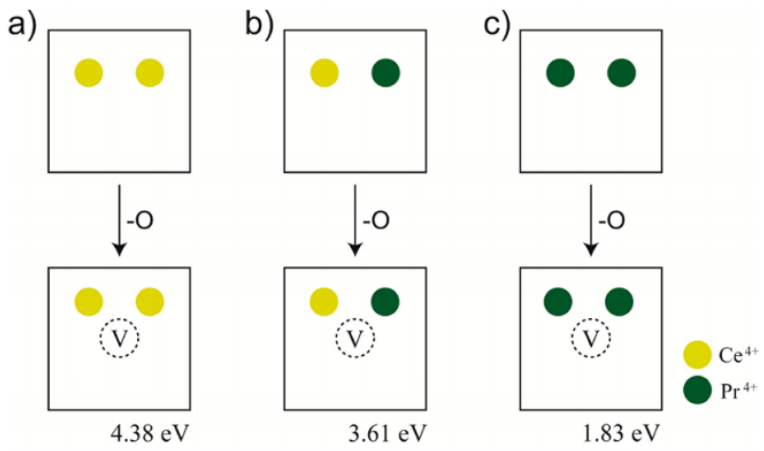

Figure 66. The calculated oxygen reduction energy based on nearest neighbor being Ce4+ or Ce3+.

established. The optimal performance occurs due to the balance of many competing factors: Pr^{3+} concentration, polaron hopping, oxygen vacancy concentration and Ce^{4+} content. The last part, regarding the importance of the Ce^{4+} content is a nuanced view that differs from the generalized statement that oxygen vacancy concentration is the best predictor for ORR activity. In summary, the praseodymium doped ceria system offers many interesting features to better understand the ORR and this current has provided some additional characteristics to be aware of when rationally designed future surface modification for SOFC cathodes.

CHAPTER 6. CONCLUSIONS AND RECOMMENDATIONS FOR FUTURE WORK

6.1 Summary and Conclusions

This work has helped develop the important factors governing the rationale design of solid oxide fuel cell cathodes. Chapter 1 offered a background on SOFC fundamentals and described the current state of the art in the cathode literature. Conventional wisdom suggests that ionic conductivity and vacancy concentration are important governing factors for ORR performance. Additionally, several thin film examples were given to describe the unique properties of conformal thin films. In order to better isolate the important factors in surface modification, Chapter 2 described the fabrication and characterization of an asymmetric cell testing set up. After sufficiently convince the asymmetric cell isolated the ORR , Chapter 3 described the surface modification with undoped and samarium doped ceria to investigate the important of oxygen ion vacancy concentration on ORR performance. The infiltration of undoped ceria suggested conformal thin films were a better morphology than the nanoparticles. Using the thin film testing set up with undoped ceria films, it was found that the 80 nm film decreased performance relative to the reference and the thicker undoped ceria films. This decrease was attributed towards a larger concentration of Ce^{3+} which limited the active sites for the ORR to occur. Moving on to the doped ceria, it was found that varying the oxygen ion conductivity (through varying samarium doped levels) enhanced performance to the same level. In other words, the polarization resistance was decreased, but there was no trend with ionic conductivity. It was postulated that the doped ceria infiltration relied on a surface diffusion mechanism rather than a bulk. This

was confirmed with conformal thin film test that showed an SDC film of any thickness would increase polarization resistance. Also in this chapter, the impedance response under bias was correlated to the oxygen vacancy concentration and used as a tool to differentiate the response of the 80 nm undoped ceria from the 160 and 320 nm undoped ceria films. The final chapter focused on the praseodymium doped ceria system, which shows nearly perfect solid solubility and a large change in ionic and electronic conductivity with composition. The 50PDC composition exhibited the lowest polarization resistance, which did not scale with ionic conductivity as expected prior to the experiment. Using XPS and TGA, the nuanced changes in cerium and praseodymium were correlated to the electrochemical performance.

6.2 Recommendations for Future Work

With the advances in thin film deposition and development of sophisticated characterization techniques, it is a great time to be involved in surface modification in electrochemical applications. The following are some suggested future work to further develop a rational guide to surface modification.

- Atomic Layer Deposition is a phenomenal tool that gives very fine control of film thickness. While there are challenges in the deposition conditions and available precursors, it offers conformal coating on a porous substrate. There has been some interesting literature that suggests extremely thin films can adopt unique crystal structures that influences performance. Comparing thin films of oxides of undoped and doped ceria, zirconia, and alumina can provide more insight into surface specific phenomena and possibly unlock new properties in conventionally inert

materials. More specifically, finding a praseodymium oxide precursor that does not leave residual silicon would allow for further study into the praseodymium doped ceria system in this work. Keep in mind that most of the ALD work in SOFCs have focused on the cathode symmetric cells because of the deposition conditions. Because ALD is a gas phase deposition technique, any film will cover entire surface exposed. It is very challenging to mask off sections to reduce exposure, especially in porous cathode supports. With that in mind, there are opportunities to deposit metals and oxides via ALD on the anode side of the fuel cell. An important characteristic to monitor for the thin film coatings is any change in degradation rate since high temperature operation may degrade the film itself. That degradation may manifest itself through segregation of specific ions into the thin film coatings so would be valuable to characterize the surface composition with XPS before and after testing and/or biasing.

- While nontrivial in fabrication and characterization, using patterned cathodes will allow more nuanced probing of the surface electrochemical reactions. It is also important to character these thin films under varying conditions including applied bias, which is less often performed in previous literature. Combining these patterned cathodes with advanced in situ or operando characterization environments like AP-XPS will provide the most information about the surface electrohcmeial and structural features. In order to even further understand the behavior, it may be helpful to include isotope exchange experiments both at open circuit and under bias to get a more visual picture of the electrochemical behavior after testing. With advancements in thin film XRD capabilities, it would also be

helpful to understand the chemical and mechanical strain in thin films as related to the cathodes or surface modification of the cathodes.

In the end, this work has demonstrated the that oxygen ion vacancy concentration is not the prime governing factor to consider when designing a surface modification strategy. There are avenues to explore in doped ceria systems that demonstrate high performance due to non-trivial changes in oxidation state of the host oxide. In a broader context, surface modification of solid oxide fuel cell cathodes provides a route to lower operating temperatures, which translates to lower costs and lower degradation rates. Both of these topic make the high efficiency, scalable SOFC technology more economically viable. Beyond SOFCs, the principles in this dissertation can be applied many electrochemical systems and catalytic applications that can be enhanced by controlling the oxidation states in thin films.

APPENDIX A. TRANSITION METAL CARBIDES FOR SOFC ANODES

Transition metal carbides are a form of interstitial alloys where the carbon sits on the octahedral sites. These compounds display high melting temperatures, the hardness and strength of a ceramic with the electrical conductivity of a metal. The crystal structure is formed based on geometric and electronic factors[104]. The Rule of Hagg states that if the ratio of nonmetal radius to metal radius is less than 0.59, then a simple structure is formed. Further, the Engel-Brewer Theory of metals states the structure is dependent on the s-p electron count per atom. As the s-p count per atom increases, the structure is transformed from bcc to fcc (metal to carbide to nitride)[105]. Many transition metals can be formed as carbides and nitrides. In general, decreasing the size of the metal atoms decreases the thermodynamic stability of the compound because the close-packed metal structure cannot accommodate interstitial atoms[104].

The electronic properties come from the interaction of the carbon 2s and 2p orbitals with the d orbitals of the metal. The heat capacity of the carbides and nitrides are systematically larger than the metal or compound, which (for a free electron gas) corresponds to the density of states at the Fermi level. This larger density of states at the Fermi level also correlates with the enhanced activity in catalytic reactions. The interstitial carbon also increases the distance between the metal atoms which causes a contraction in the d band. Therefore, even with less electrons, the d band is filled to a greater extent, which mimics the high density of states found in the Group 8 metals[106].

Levy and Boudart were the first to correlate the catalytic properties of transition carbides to a noble metal. They showed that WC catalyzes the formation of water from hydrogen and oxygen, the reduction of tungsten trioxide by hydrogen in the presence of water and the isomerization of 2,2-dimethylpropane to 2-methylbutane[107]. Each of these catalyzed reactions is typical of platinum, but not of the tungsten metal. Additionally, the decomposition of ethylene on the surfaces of Mo and W carbides to the ethylidyne intermediate on the close packed surfaces followed the same behavior as platinum, but differed in desorption temperature thus showing similar but not identical catalytic activity to the noble metal[108].

The catalytic properties are very surface sensitive. Density functional theory (DFT) calculations by Liu and Rodriguez identified the importance of the oxycarbide in catalyzing the water-gas shift reaction[109]. They found that Mo-terminated and C-terminated Mo_2C showed less activity relative to a conventional Cu catalyst toward the water gas shift reaction because of oxygen being too strongly bonded to the Mo or C on the terminating surface. The strong bond prevented the water dissociation and the CO adsorption. However, when the C-terminated Mo_2C was covered by an adsorbed oxygen on the surface, the WGS activity was greater than even the commercially used Cu catalyst. They hypothesized that the C atoms destabilize the covered O by forming CO species, which in turn shift away from the Mo. The Mo is then able to form a moderate bond to the reaction intermediates thus displaying higher activity.

Sullivan et al showed that co-feeding O_2 into a Mo_2C sample increased the Bronsted acid site density by a factor of 30 without transforming the 2-5 nm bulk Mo_2C into MoO_2, although the surface was passivated with a thin oxygen layer (although the oxide layer

couldn't be characterized with XPS, TEM, or XRD)[110]. The conjugate base is most likely the Mo-O species. This reinforces the importance of the surface layer and specifically the interactions of oxygen on the surface of an oxophillic transition metal carbide like Mo_2C. Bronsted acid sties play a key role in the beta scission of hydrocarbons (i.e. the breaking of the carbon-carbon bond), which is important when trying to use hydrocarbon fuel. Bronsted acids also play a key role in hydrogen spill over which is important in proton transport from the fuel to the proton conducting phase in the anode[111]. In general, transition metal carbides bind carbon more weakly than transition metal oxides, which may be helpful for oxidizing any adventitious carbon[112].

Transition metal carbides offer a unique possibility dealing with the hydrocarbon fuels with a Mars van Krevelen-type reaction. In heterogeneous catalytic chemistry, there are three main mechanisms involving the adsorption and desorption of gas molecules on an active surface, as show in Figure 67. Figure 67 a) shows a Langmuir-Hinshelwood mechanism where both molecules adsorb on the surface before the reaction takes place. Figure 3B shows an Eley-Rideal mechanism where only one of the reactants absorbs and interacts with a gas phase molecule followed by desorption of the reaction product. Figure

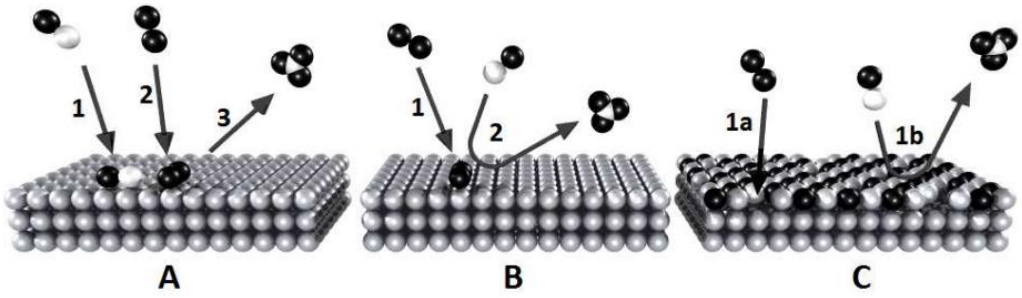

Figure 67. The (A) Langmuir-Hinshelwood mechanism, (B) Eley-Rideal mechanism, and the (C) Mars-Van Krevelen mechanism [126]

3 shows the Mars-Van Krevelen mechanism by which the adsorbed molecule interacts with the surface species of the catalyst as opposed to another gas phase reactant[113].

The Mars-van Krevelen mechanism has been shown to be active in oxides, sulfides, chlorides and hydrides[114]. In one example, manganese (IV) dioxide can be reduced to MnO by hydrogen or CO, and then oxidized in a stream of nitrobenzene into the steady state of Mn_3O_4. Using Mn oxide catalyst labelled with ^{18}O, it was found that the nitrobenzene and oxidized products contained oxygen from the catalyst[115], [116]. In two studies on hydrocarbon gases with YSZ and lanthanum transition metal perovskites, the partial oxidation of methane was determined to be aided by the Mars-van Krevelen mechanism. This same mechanism has been proposed in transition metal carbide systems with carbon containing reactants. Marin-Flores et al showed that nanoparticle molybdenum dioxide was a highly active catalyst for partial oxidation of large hydrocarbon fuels (dodecane)[117]. Through the carbo-thermal process, the MoO_2 was transformed into Mo_2C, but the surface was considered an oxycarbide. However, bulk Mo_2C was used as a reference and did not have the same activity towards the large hydrocarbon. Instead, they suggested a thin layer of oxide due to on the surface (that was not detectable by XRD but was identified in EDX) was responsible for the increased catalytic performance.

In order to leverage the molybdenum oxycarbide in an electrochemical system, the oxygen will be put come from the ionically conductive electrolyte instead of with the fuel. The concept of oxygen ion conduction in oxide supported catalysts is known as electrochemical promotion in the catalysis literature. Wang et al demonstrated the concept in a “self-sustained electrochemical promotion catalyst”, which is essentially a short circuited SOFC[118]. Using a Ni-Cu-Ce | YSZ | LSM structure, the authors found a 2-4

fold increase relative to Pt-Ceria catalysts in partial oxidation of heavy hydrocarbons when flowing n-pentadecane with air at slightly higher than atmospheric pressure. The purpose of this part of the research project is to identify role of carbide in any coking tolerance and catalytic enhancement of the oxidation of hydrocarbons without the use of externally supplied oxygen.

The positive effect of the substrate material for a catalyst is known as a promoter. In addition to providing coking tolerance, the molybdenum carbide may also act as a promoter for the reforming activity of nickel or other the performance of other metallic catalysts like platinum[119]. Rodriquez, et al showed through DFT that metal atoms like Ni, Cu, and Au interact strongly with the C in the TiC substrate and change the electronic structure immediately around the metal to carbon bond. This resulted in enhanced catalytic activity of the TiC supported than the individual metal specifically in the reverse water-gas shift reaction to create methanol from CO_2 and hydrogen[120]. Kelly and Chen combined DFT and experimental work to determine that metal modification of a Mo_2C substrate can lead to different reaction pathways[121]. Using ethanol as a probe molecule, they found that bare Mo_2C produced primarily ethylene, while Ni modified Mo_2C produced CO and copper produced acetaldehyde indicating that changing the metal modifier can allow for different reaction pathways.

6.3 Patterned Anode

Using a pattern anode allows for direct comparison of two catalysts without worrying about contributing variables like differences in particle size, phase distribution, and triple phase boundary length. When looking to deposit a patterned anode, there are several

techniques with varying length scale and processing complexities. For the patterned anodes in this dissertation, a shadow mask set-up was used because it provided the feature sizes needed without requiring extensive clear room fabrication procedures. The shadow masks were fabricated from tempered spring steel (AISI 1074) due to the high elastic modulus and toughness that is required for the cleaning and handling steps. The patterns were cut out using a computer controlled RF CO_2 laser mill (Mermes LS500XL) managed by the Georgia Tech Institute for Electronics and Nanotechnology. The masks were then cleaned via sonication in a 2% alkaline solution (Microsoap®) followed by an etch in 12% HCl solution. The patterns are deposited on a polished electrolyte support. These supports are fabricated by dry pressing 0.35g of 20 mol% samarium doped ceria (SDC) that had already been ball-milled in ethanol for 24 hours with 1 wt% polyvinylbutyral (PVB) to act as a binder. The pellets were then fired according to the following furnace schedule:

- 25°C to 500°C at 1°C/min with a 1-hour dwell
- 500°C to 800°C at 2°C/min
- 800°C to 1400°C at 3°C/min with a 5-hour dwell
- 1400°C to 25°C at 3°C/min

The electrolyte supports were greater than 95% dense according to Archimedes method using (find SDC ideal density) as the theoretical density of SDC. After firing, the pellets were polished using a MetPrep3 (Allied High Tech) with the protocol shown in **Table 2**. The pellets were mounted with Crystalbond to a metal puck heated to 240°C on a hot plate. After cooling, the samples were put in the polisher.

After polishing, the cathode was then attached to the non-polished side of the electrolyte pellet. The LSCF electrodes were tape cast according to the protocol in Table 3. After mixing, the slurries were degassed in a vacuum oven for 5-10 minutes and then cast with a blade height of 50 μm. The tape was then let dry overnight and 6.6 mm circles were punched out. The LSCF tape-cast electrodes are adhered using an SDC slurry. The buffer layer slurry is composed of SDC, V006 and acetone in a 1:4:20 ratio, respectively. It was found that adding an additional 2 wt% of Triton X-100 yielded more uniform buffer layers. Then, 30 μL of the buffer solution was dropped onto the SDC electrolyte pellet. After 20-30 minutes of drying at room temperature, the LSCF tape cast circle is pressed on with a cotton swab. The cells were then placed in a drying oven at 80°C for 2 hours. The cells were then fired to 1080°C for 2 hours with a one-hour burnout at 400°C. The electrolyte supports with attached cathodes were then placed on a sample holder that had a small magnet attached to the other side. The magnet (McMaster Carr) was used to reduce any metal deposition under the mask during sputtering. It was determined that the magnet was able to hold down the pattern without any bending of the mask, which happened when using the larger (size) magnets. The resulting patterns showed crisp edges that were attributed to the excellent contact between the mask and the polished electrolyte surface. The fabrication process is shown in Figure 68. As seen in the final cell, the cathode covers only the patterned anode so as to limit the electrochemical activity to the pattern and not the electrical contact pad. In order to test the completed cell, silver wire (get info) was flattened between two steel blocks and adhered using silver paste (Heraeus C8710). After approximately one hour in the drying oven at 80°C, another silver wire was coiled, flattened and adhered with silver paste. The cell was sealed on the alumina tube with three

coats of Ceramabond with one hour of drying time in between and 12+ hours of drying time at room temperature after the final coat.

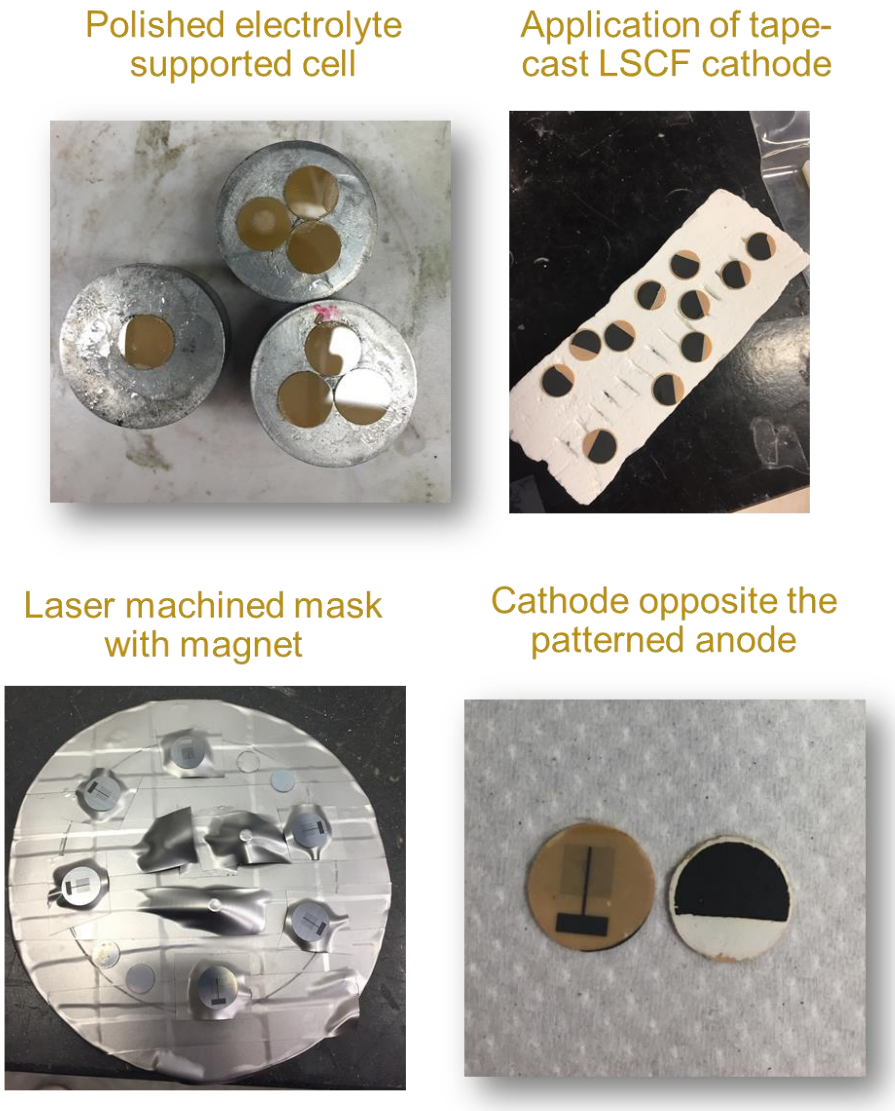

Figure 68. The processing flow of the electrolyte-supported patterned anode full cells from polishing to cathode attachment to sputtering to full cell ready for testing. The final cell shows the cathode aligned with the pattern but not overlapping the electrical contact pad.

6.4 Carburization of Mo_2C

There are many ways to fabricate molybdenum carbide. Some carburize from the oxide. Some fabricate with a carbon source. For this dissertation, sputtering was used to deposit thin films of molybdenum metal that were then carburized in an atmosphere of hydrogen and methane.

In order to identify that the molybdenum carbide had been formed, XPS was used. XPS is a surface sensitive technique that gives information about chemical state and relative composition. There are several phases of molybdenum carbide with varying ratios of Mo to C. Wan et al analyzed four phases of molybdenum carbide via the Mo 3d spectra as shown in Figure 69[122]. Each of the spectra show a peak at defined peak at 236 eV which is attributed to the variety of molybdenum oxide formation. The important take-away from that figure is the relative heights of peaks at Mo^{0+} peaks (~229eV and ~232eV) represented by the blue fit lines. Each different processing method or precursor choice shows can manifest different amount of oxide formation, but the ratio of the peaks at 232eV to 229eV is an indicator of the Mo_2C formation. Further evidence of the oxide peak is given by Vrubel and Hu where they showed a decrease to the oxide peak after an activation period during galvanostatic electrolysis[123]. The decrease in oxide observed via XPS correlated with increase in performance, which is supported by the poor performance of Mo, MoO_2 and MoO_3 as individual catalysts for the hydrogen evolution reaction being tested in that experiment. Oshikawa et al carburized MoO_3 powder in a stream of $20CH_4/80H_2$ at different temperatures to form different phases of molybdenum carbide and then tested the activity towards methane reforming.

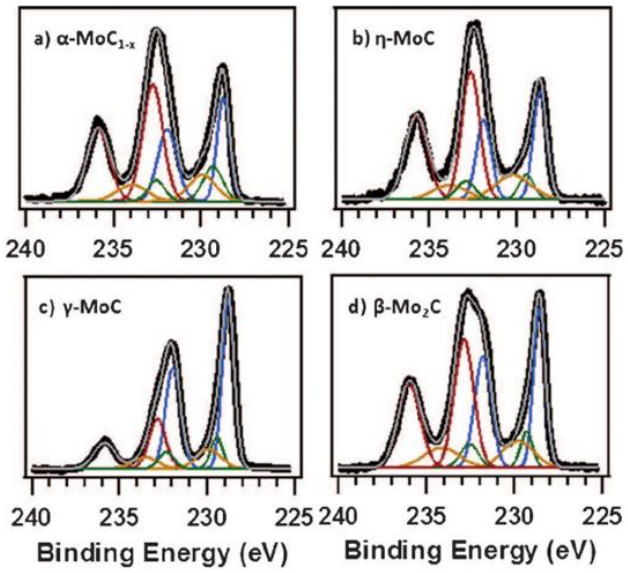

Figure 3. XPS Mo 3d spectra (without background, black) and the fitting peaks (gray) of a) α-MoC_{1-x}, b) η-MoC, c) γ-MoC, d) β-Mo_2C. Mo^0: blue, Mo^{3+}: green, Mo^{4+}: yellow, Mo^{6+}: red.

Phase	Structure	Stacking sequence	Space group	Crystal view
α-MoC_{1-x} (NaCl type)	Cubic	ABCABC	$Fm\bar{3}m$	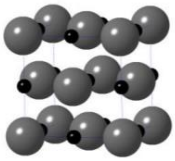
β-Mo_2C (Fe_2N type)	Hexagonal	ABAB	P63/mmc	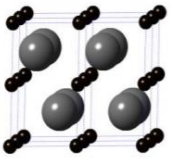
γ-MoC (WC type)	Hexagonal	AAAA	$P\bar{6}m2$	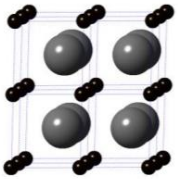
η-MoC (MoC type)	Hexagonal	ABCABC	P63/mmc	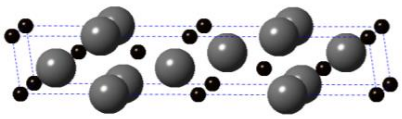

Figure 69. Reference XPS spectra for Mo 3d and the accompanying crystal structure of each phase [122]

With the Mo 3d spectra, they determined the 3:2 ratio of the doublet 3d5/2 to 3d3/2[124]. They also showed more specific binding energies for the Mo oxidation states and graphitic carbon if more details are needed.

The carburization of the molybdenum patterned anodes were fabricated under three different conditions as indicated in Table 7. There were several problems that arose with the carburization of the molybdenum pattern. First, the pellets would crack in half or into multiple pieces. The cause of the cracking was unclear. Since the carburization was first performed using an alumni plate as a substrate, it was thought that there may be some thermal stresses due to a heat sink located below the pellet. However, the cracking still occurred even with the SDC powder supporting the pellet. Another potential thermal stress could have been due to temperature of the carburization gases. These gases were flown in at ~80 sccm total flow rate into a tube that was approximately 10 inches long. This may have not allowed enough time for the gases to warm before flowing over the pellet. To mitigate this, the pellet was place in an alumni cup tipped on its side with SDC powder below the pellet. This little cave would prevent the gas from flowing directly over the pellet. Unfortunately, the pellet still cracked under the carburization conditions as shown in Figure 70.

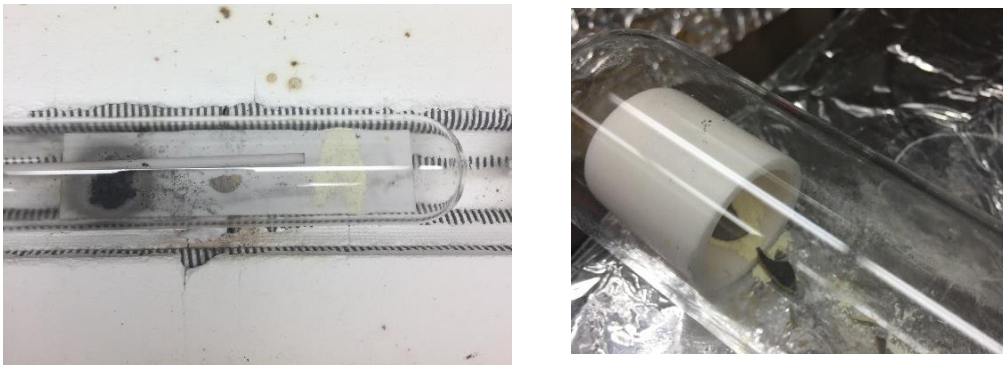

Figure 70. Pellets cracking after carburization process.

Table 7. Carburization conditions for Mo_2C

Gas Composition	**Annealing Temperature**	**Dwell Time**
20% CH_4 – 80% H_2	700°C	2 hours
20% CH_4 – 80% H_2	800°C	
50% CH_4 – 50% H_2	700°C	

In addition to cracking, the morphology of the pattern changes during carburization. Many catalytic studies indicate the increase in surface area when moving from molybdenum metal to molybdenum carbide. Dang et al carburized molybdenum oxide at different temperatures and found two different carburization mechanisms using TGA[125].

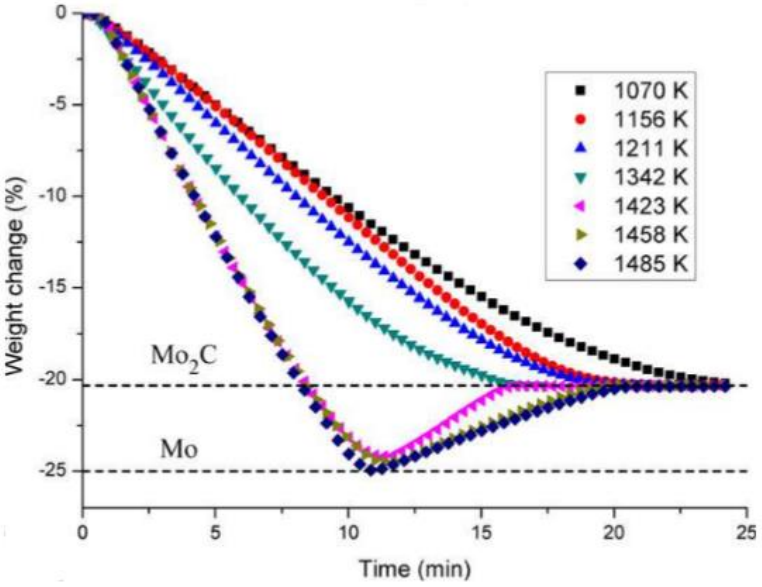

Figure 71. Weight change as measured by TGA of MoO_2 in a CO atmosphere at different temperatures. Taken from reference cited in text.

At lower temperatures, molybdenum oxide went directly to molybdenum carbide as shown in the Figure 72. At higher temperatures, the oxide reduced to molybdenum metal and then carburized. As seen in the SEM, the powder that was directly carburized maintains the dense morphology. On the other hand, the powder that first reduced to molybdenum metal took on a more porous, higher surface area morphology. The observation of a more porous molybdenum carbide was evident in my samples when carburizing from the metal pattern. As shown in the Figure 73, each of the carburization conditions led to cracking of the molybdenum carbide pattern. In the top left is the as deposited molybdenum film, which shows the dense, pin-hole free film. The top right image was carburized under $20CH_4/80H_2$

at 700°C for 10 hours and shows cracking in the film. The bottom left image was carburized under $20CH_4/80H_2$ at 800°C for 10 hours and displays a larger density of cracking. The bottom right image shows the carburization in $50CH_4/50H_2$ at 700°C for 10 hours. The pattern shows cracking as well as what appears to be deposited carbon on the surface of the film. These images were taken of a molybdenum film deposited on an SDC – not the patterned molybdenum film. When the pattern was carburized, the thin arms of the pattern were disconnected as shown in Figure 73.

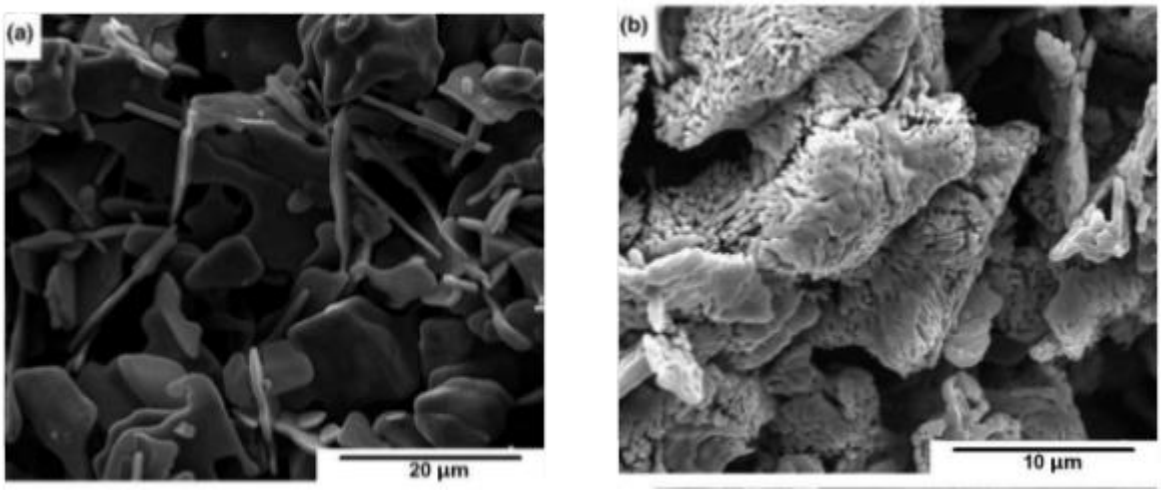

Figure 72. Different morphologies of Mo_2C derived from different carburization conditions [125]

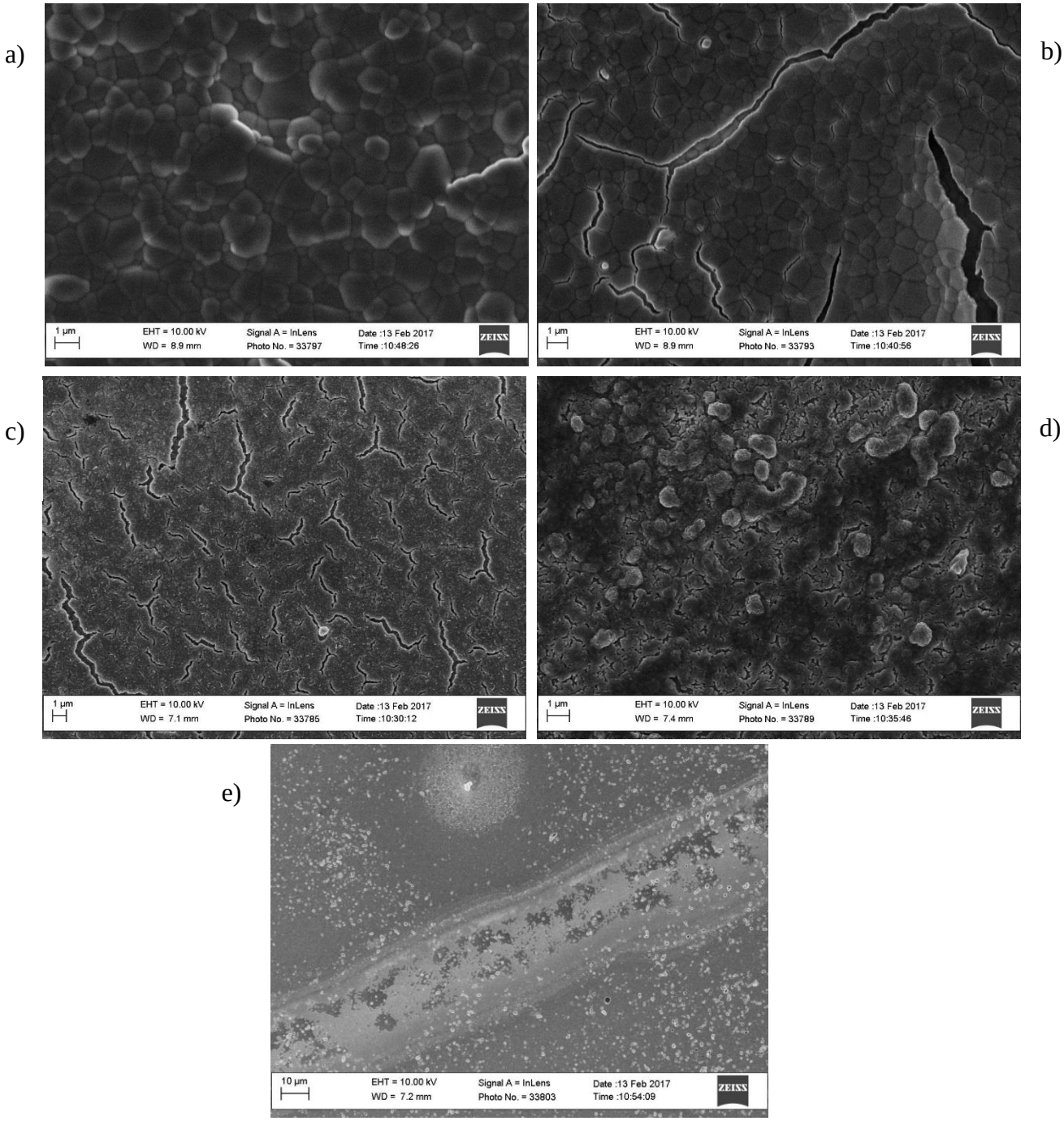

Figure 73. SEM micrograph of a) as deposited molybdenum b) carburized in $20CH_4/80H_2$ at 700°C for 10 hours c) carburized in $20CH_4/80H_2$ at 800°C for 10 hours, d) carburized at $50CH_4/50H_2$ at 700°C for 10 hours and e) the pattern after carburization.

6.5 Raman

Figure 74 shows the Raman spectra for Mo_2C and MoO_3 powders as a reference. The black data points for the molybdenum carbide showed almost no discernable Raman spectra as indicated by the lack of peaks and very low total counts. The MoO_3 was very Raman active and showed multiple peaks with very high intensities, as indicated by the second y-axis with two orders of magnitude larger peak count. This indicates that identifying molybdenum oxide if formed during the operando test would be identifiable in our current Raman set up. Note that for the molybdenum carbide, there is not a signal associated with the carbon prevalent in coking. Thus, it will be possible to identify any coking that occurs on the molybdenum carbide pattern.

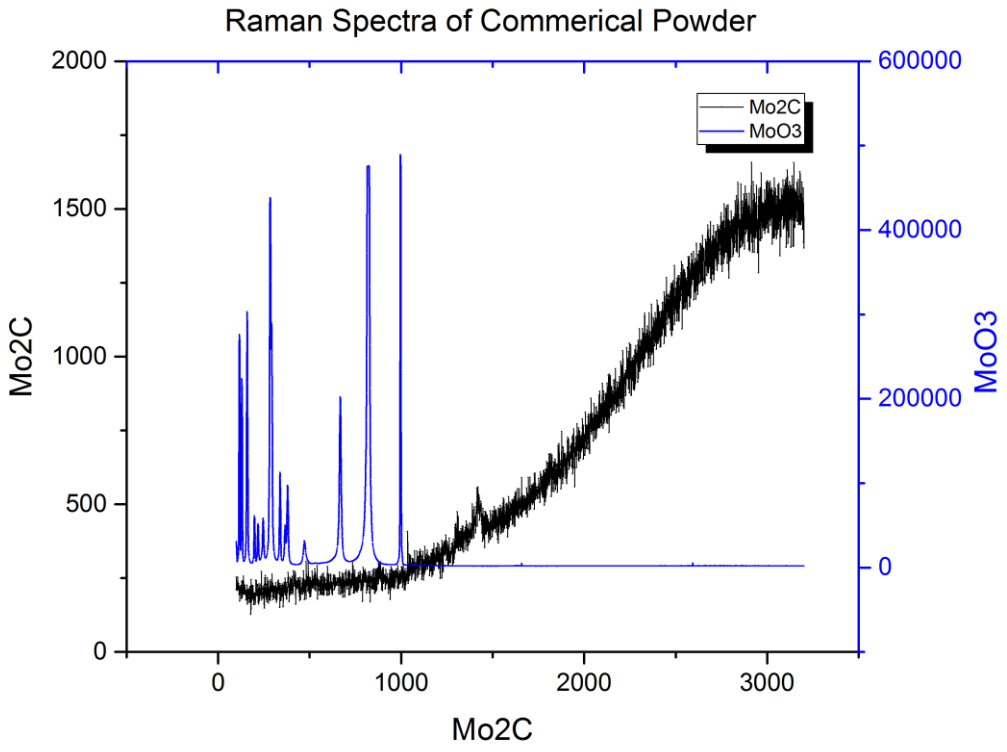

Figure 74. Raman spectra of commercial Mo_2C and MoO_3 powder.

REFERENCES

[1] U.S. Energy Information Administration, “International Energy Outlook 2016,” 2016.

[2] U.S. Energy Information Administration, “Annual Energy Outlook 2017,” 2017.

[3] H. Maru, S. Singhal, C. Stone, and D. Wheeler, “1–10 kW Stationary Combined Heat and Power Systems Status and Technical Potential,” 2010.

[4] B. Owens and J. McGuinness, “GE-Fuel Cells The Power of Tomorrow,” 2015.

[5] E. D. Wachsman, C. A. Marlowe, and K. T. Lee, “Role of solid oxidefuel cells in a balanced energy strategy,” *Energy Environ. Sci.*, vol. 5, no. 2, pp. 5498–5509, 2012.

[6] D. M. Bierschenk, J. R. Wilson, and S. A. Barnett, “High efficiency electrical energy storage using a methane–oxygen solid oxide cell,” *Energy Environ. Sci.*, vol. 4, no. 3, pp. 944–951, 2011.

[7] C. Graves, S. D. Ebbesen, S. H. Jensen, S. B. Simonsen, and M. B. Mogensen, “Eliminating degradation in solid oxide electrochemical cells by reversible operation,” *Nat. Mater.*, vol. 14, no. 2, pp. 239–244, 2014.

[8] S. Vora, “Office of Fossil Energy’s Solid Oxide Fuel Cell Program Overview,” in *15th Annual SECA Workshop*, 2014.

[9] H. Yokokawa, H. Tu, B. Iwanschitz, and A. Mai, “Fundamental mechanisms limiting solid oxide fuel cell durability,” *J. Power Sources*, vol. 182, no. 2, pp. 400–412, 2008.

[10] Y. Lin, Z. Zhan, J. Liu, and S. A. Barnett, “Direct operation of solid oxide fuel cells with methane fuel,” *Solid State Ionics*, vol. 176, no. 23–24, pp. 1827–1835, 2005.

[11] D. J. L. Brett, A. Atkinson, N. P. Brandon, and S. J. Skinner, “Intermediate temperature solid oxide fuel cells.,” *Chem. Soc. Rev.*, vol. 37, no. 8, pp. 1568–78, Aug. 2008.

[12] Z. Gao, L. V. Mogni, E. C. Miller, J. G. Railsback, and S. A. Barnett, “A perspective on low-temperature solid oxide fuel cells,” *Energy Environ. Sci.*, vol. 9, no. 5, pp. 1602–1644, 2016.

[13] A. H. Brian Steele, “Materials for fuel cell technologies,” *Nature*, vol. 414, pp. 345–352, 2001.

[14] I. Pilatowsky, R. J. Romero, C. A. Isaza, S. A. Gamboa, P. J. Sebastian, and W. Rivera, *Cogeneration Fuel Cell-Sorption Air Conditioning Systems*. 2011.

[15] R. O’Hayre, S.-W. Cha, W. Colella, and F. Prinz, *Fuel Cell Fundamentals*, 2nd Editio. John Wiley & Sons, 2009.

[16] H. Tuller and S. Bishop, “Point Defects in Oxides- Tailoring Materials Through Defect Engineering,” 2011.

[17] S. B. Adler, “Factors Governing Oxygen Reduction in Solid Oxide Fuel Cell Cathodes †,” *Chem. Rev.*, vol. 104, no. 10, pp. 4791–4844, Oct. 2004.

[18] Z. Gao, L. V. Mogni, E. C. Miller, J. G. Railsback, and S. A. Barnett, “A perspective on low-temperature solid oxide fuel cells,” *Energy Environ. Sci.*, vol. 9, no. 5, pp. 1602–1644, 2016.

[19] E. V Tsipis and V. V Kharton, “Electrode materials and reaction mechanisms in solid oxide fuel cells: a brief review,” *J. Solid State Electrochem.*, vol. 12, no. 11, pp. 1367–1391, 2008.

[20] M. L. Perry, “Mass Transport in Gas-Diffusion Electrodes: A Diagnostic Tool for Fuel-Cell Cathodes,” *J. Electrochem. Soc.*, vol. 145, no. 1, p. 5, 1998.

[21] M. Kleitz, L. Dessemond, T. Kloidt, and M. C. Steil, “Space Expansions of the Regular Oxygen Electrode Reaction on YSZ - II Silver Electrodes,” in *Proceedings of the Fourth International Symposium on Solid Oxide Fuel Cells*, p. 527.

[22] M. Verkerk and A. Bruggraaf, “Oxygen Transfer on Substituted ZrO2, Bi2O3, and CeO2 Electrolytes with Platinum Electrodes,” *J. Electrochem. Soc. Soc.*, vol. 354, no. January, pp. 78–84, 1983.

[23] J. R. MacDonald, *Impedance Spectroscopy: Emphasizing Solid Materials and Systems*. New York, NY: John Wiley and Sons, 1987.

[24] B. A. Boukamp and H. J. M. Bouwmeester, "Interpretation of the Gerischer impedance in solid state ionics," in *Solid State Ionics*, 2003, vol. 157, no. 1–4, pp. 29–33.

[25] Y. Li, K. Gerdes, and X. Liu, "Oxygen Transport Kinetics in Infiltrated SOFCs Cathode by Electrical Conductivity Relaxation Technique," *J. Electrochem. Soc.*, vol. 160, no. 6, pp. F554–F559, 2013.

[26] L. Nie, M. Liu, Y. Zhang, and M. Liu, "La0.6Sr0.4Co0.2Fe0.8O3−δ cathodes infiltrated with samarium-doped cerium oxide for solid oxide fuel cells," *J. Power Sources*, vol. 195, no. 15, pp. 4704–4708, Aug. 2010.

[27] T. Z. Sholklapper, H. Kurokawa, C. P. Jacobson, S. J. Visco, and L. C. De Jonghe, "Nanostructured solid oxide fuel cell electrodes," *Nano Lett.*, vol. 7, no. 7, pp. 2136–2141, 2007.

[28] W. Zhu, D. Ding, and C. Xia, "Enhancement in Three-Phase Boundary of SOFC Electrodes by an Ion Impregnation Method: A Modeling Comparison," *Electrochem. Solid-State Lett.*, vol. 11, no. 6, p. B83, 2008.

[29] Y. J. Leng, S. H. Chan, K. a. Khor, and S. P. Jiang, "(La0.8Sr0.2)0.9MnO3–Gd0.2Ce0.8O1.9 composite cathodes prepared from (Gd, Ce)(NO3) x -modified (La0.8Sr0.2)0.9MnO3 for intermediate-temperature solid oxide fuel cells," *J. Solid State Electrochem.*, vol. 10, pp. 339–347, 2006.

[30] D. Ding, X. Li, S. Y. Lai, K. Gerdes, and M. Liu, "Enhancing SOFC cathode performance by surface modification through infiltration," *Energy Environ. Sci.*, vol. 7, no. 2, p. 552, 2014.

[31] Z. Jiang, L. Zhang, L. Cai, and C. Xia, "Bismuth oxide-coated (La,Sr)MnO3 cathodes for intermediate temperature solid oxide fuel cells with yttria-stabilized zirconia electrolytes," *Electrochim. Acta*, vol. 54, no. 11, pp. 3059–3065, 2009.

[32] T. Hong, L. Zhang, F. L. Chen, and C. R. Xia, "Oxygen surface exchange properties of La0.6Sr0.4Co0.8Fe0.2O3-(delta) coated with SmxCe1-O-x(2)-(delta)," *J. Power Sources*, vol. 218, pp. 254–260, 2012.

[33] E. N. Armstrong, K. L. Duncan, D. J. Oh, J. F. Weaver, and E. D. Wachsman, "Determination of Surface Exchange Coefficients of LSM, LSCF, YSZ, GDC Constituent Materials in Composite SOFC Cathodes," *J. Electrochem. Soc.*, vol. 158, no. 5, p. B492, 2011.

[34] J. A. Lane and J. A. Kilner, "Oxygen surface exchange on gadolinia doped ceria," *Solid State Ionics*, vol. 136–137, pp. 927–932, 2000.

[35] M. Liu, M. Liu, D. Ding, K. Blinn, X. Li, and L. Nie, "Enhanced performance of LSCF cathode through surface modification," *Int. J. Hydrogen Energy*, vol. 37, no. 10, pp. 8613–8620, May 2012.

[36] N. Tsvetkov, Q. Lu, L. Sun, E. J. Crumlin, and B. Yildiz, "Improved chemical and electrochemical stability of perovskite oxides with less reducible cations at the surface," *Nat. Mater.*, vol. 15, no. 9, pp. 1010–1016, 2016.

[37] X. Lou, Z. Wang, L. Yang, and M. Liu, "Improving La0.6Sr0.4Co0.2Fe0.8O3 − δ cathode performance by infiltration of a Sm0.5Sr0.5CoO3 − δ coating," *Solid State Ionics*, vol. 180, no. 23–25, pp. 1285–1289, Oct. 2009.

[38] S. Carter, A. Selcuk, R. J. Chater, J. Kajda, J. A. Kilner, and B. C. H. Steele, "Oxygen transport in selected nonstoichiometric perovskite-structure oxides," *Solid State Ionics*, vol. 53–56, no. PART 1, pp. 597–605, 1992.

[39] M. E. Lynch, L. Yang, W. Qin, J.-J. Choi, M. Liu, K. Blinn, and M. Liu, "Enhancement of La0.6Sr0.4Co0.2Fe0.8O3-δ durability and surface electrocatalytic activity by La0.85Sr0.15MnO3±δ investigated using a new test electrode platform," *Energy Environ. Sci.*, vol. 4, no. 6, p. 2249, 2011.

[40] G. J. la O', R. F. Savinell, and Y. Shao-Horn, "Activity Enhancement of Dense Strontium-Doped Lanthanum Manganite Thin Films under Cathodic Polarization: A Combined AES and XPS Study," *J. Electrochem. Soc.*, vol. 156, no. 6, pp. B771–B781, 2009.

[41] A. Giuliano, M. P. Carpanese, D. Clematis, M. Boaro, A. Pappacena, F. Deganello, L. F. Liotta, and A. Barbucci, "Infiltration, Overpotential and Ageing Effects on Cathodes for Solid Oxide Fuel Cells: La0.6Sr0.4Co0.2Fe0.8O3-δ versus Ba0.5Sr0.5Co0.8Fe0.2O3-δ," *J. Electrochem. Soc.*, vol. 164, no. 10, pp. F3114–F3122, Aug. 2017.

[42] D. Lee, Y.-L. Lee, A. Grimaud, W. T. Hong, M. D. Biegalski, D. Morgan, and Y. Shao-Horn, "Enhanced Oxygen Surface Exchange Kinetics and Stability on Epitaxial La 0.8 Sr 0.2 CoO 3−δ Thin Films by La 0.8 Sr 0.2 MnO 3−δ Decoration," *J. Phys. Chem. C*, vol. 118, no. 26, pp. 14326–14334, 2014.

[43] H. Uchida, S. Arisaka, and M. Watanabe, "High performance electrodes for medium-temperature solid oxide fuel cells: Activation of La(Sr)CoO3 cathode with highly dispersed Pt metal electrocatalysts," *Solid State Ionics*, vol. 135, no. 1–4, pp. 347–351, Nov. 2000.

[44] S. Simner, J. Bonnett, N. Canfield, K. Meinhardt, J. Shelton, V. Sprenkle, and J. Stevenson, "Development of lanthanum ferrite SOFC cathodes," *J. Power Sources*, vol. 113, no. 1, pp. 1–10, Jan. 2003.

[45] J. Serra and H. P. Buchkremer, "On the nanostructuring and catalytic promotion of intermediate temperature solid oxide fuel cell (IT-SOFC) cathodes," *J. Power Sources*, vol. 172, no. 2, pp. 768–774, Oct. 2007.

[46] J. Li, U. G. Singh, J. W. Bennett, K. Page, J. C. Weaver, J. P. Zhang, T. Proffen, A. M. Rappe, S. Scott, and R. Seshadri, "BaCe1-xPdxO3-?? (0 ??? x ??? 0.1): Redox controlled ingress and egress of palladium in a perovskite," *Chem. Mater.*, vol. 19, no. 6, pp. 1418–1426, 2007.

[47] M. Cassir, A. Ringuedé, and L. Niinistö, "Input of atomic layer deposition for solid oxide fuel cell applications," *J. Mater. Chem.*, vol. 20, no. 41, p. 8987, Oct. 2010.

[48] J. H. Shim, C.-C. Chao, H. Huang, and F. B. Prinz, "Atomic Layer Deposition of Yttria-Stabilized Zirconia for Solid Oxide Fuel Cells," *Chem. Mater.*, vol. 19, no. 15, pp. 3850–3854, Jul. 2007.

[49] P.-C. Su, C.-C. Chao, J. H. Shim, R. Fasching, and F. B. Prinz, "Solid Oxide Fuel Cell with Corrugated Thin Film Electrolyte," *Nano Lett.*, vol. 8, no. 8, pp. 2289–2292, Aug. 2008.

[50] C.-C. Chao, C.-M. Hsu, Y. Cui, and F. B. Prinz, "Improved Solid Oxide Fuel Cell Performance with Nanostructured Electrolytes," *ACS Nano*, vol. 5, no. 7, pp. 5692–5696, Jul. 2011.

[51] A. Karthikeyan, C.-L. Chang, and S. Ramanathan, "High temperature conductivity studies on nanoscale yttria-doped zirconia thin films and size effects," *Appl. Phys.*

Lett., vol. 89, no. 18, p. 183116, 2006.

[52] H.-R. Kim, J.-C. Kim, K.-R. Lee, H.-I. Ji, H.-W. Lee, J.-H. Lee, and J.-W. Son, "'Illusional' nano-size effect due to artifacts of in-plane conductivity measurements of ultra-thin films," *Phys. Chem. Chem. Phys.*, vol. 13, no. 13, pp. 6133–6137, 2011.

[53] S. J. Litzelman, J. L. Hertz, W. Jung, and H. L. Tuller, "Opportunities and Challenges in Materials Development for Thin Film Solid Oxide Fuel Cells," *Fuel Cells*, vol. 8, no. 5, pp. 294–302, Oct. 2008.

[54] C. Brahim, F. Chauveau, A. Ringuedé, M. Cassir, M. Putkonen, and L. Niinistö, "ZrO 2 –In 2 O 3 thin layers with gradual ionic to electronic composition synthesized by atomic layer deposition for SOFC applications," *J. Mater. Chem.*, vol. 19, no. 6, pp. 760–766, Jan. 2009.

[55] J. W. Elam, N. Dasgupta, and F. B. Prinz, "ALD for clean energy conversion, utilization, and storage," *MRS Bulletin*, 2011. [Online]. Available: http://journals.cambridge.org/action/displayFulltext?type=1&fid=8438766&jid=MRS&volumeId=36&issueId=11&aid=8438764&bodyId=&membershipNumber=&societyETOCSession=. [Accessed: 09-Apr-2015].

[56] M. M. Biener, J. Biener, A. Wichmann, A. Wittstock, T. F. Baumann, M. Bäumer, and A. V Hamza, "ALD functionalized nanoporous gold: thermal stability, mechanical properties, and catalytic activity.," *Nano Lett.*, vol. 11, no. 8, pp. 3085–90, Aug. 2011.

[57] Y. Gong, D. Palacio, X. Song, R. L. Patel, X. Liang, X. Zhao, J. B. Goodenough, and K. Huang, "Stabilizing nanostructured solid oxide fuel cell cathode with atomic layer deposition.," *Nano Lett.*, vol. 13, no. 9, pp. 4340–5, Oct. 2013.

[58] R. Kungas, A. S. Yu, J. Levine, J. M. Vohs, and R. J. Gorte, "An Investigation of Oxygen Reduction Kinetics in LSF Electrodes," *J. Electrochem. Soc.*, vol. 160, no. 2, pp. F205–F211, Dec. 2012.

[59] A. S. Yu, R. Kungas, J. M. Vohs, and R. J. Gorte, "Modification of SOFC Cathodes by Atomic Layer Deposition," *J. Electrochem. Soc.*, vol. 160, no. 11, pp. F1225–F1231, Sep. 2013.

[60] S. B. Adler, "Factors governing oxygen reduction in solid oxide fuel cell cathodes," *Chem. Rev.*, vol. 104, no. 10, pp. 4791–4843, 2004.

[61] S. B. Adler, "Factors Governing Oxygen Reduction in Solid Oxide Fuel Cell Cathodes †," *Chem. Rev.*, vol. 104, no. 10, pp. 4791–4844, Oct. 2004.

[62] W. Lai and S. M. Haile, "Impedance spectroscopy as a tool for chemical and electrochemical analysis of mixed conductors: A case study of ceria," *J. Am. Ceram. Soc.*, vol. 88, no. 11, pp. 2979–2997, 2005.

[63] "Ultra High Vacuum Lab. Saarland University." [Online]. Available: ttp://jacobs.physik.uni-saarland.de/instrumentation/uhvl.htm%0A.

[64] J. W. Lee, Z. Liu, L. Yang, H. Abernathy, S. H. Choi, H. E. Kim, and M. Liu, "Preparation of dense and uniform La0.6Sr0.4Co0.2Fe0.8O3-δ (LSCF) films for fundamental studies of SOFC cathodes," *J. Power Sources*, vol. 190, no. 2, pp. 307–310, 2009.

[65] "Practical Process Tips," 2010.

[66] N. J. Simrick, A. Bieberle-Hütter, T. M. Ryll, J. A. Kilner, A. Atkinson, and J. L. M. Rupp, "An investigation of the oxygen reduction reaction mechanism of La0.6Sr0.4Co0.2Fe0.8O3 using patterned thin films," *Solid State Ionics*, vol. 206, pp. 7–16, 2012.

[67] J.-W. Lee, Z. Liu, L. Yang, H. Abernathy, S.-H. Choi, H.-E. Kim, and M. Liu, "Preparation of dense and uniform La0.6Sr0.4Co0.2Fe0.8O3?? (LSCF) films for fundamental studies of SOFC cathodes," *J. Power Sources*, vol. 190, no. 2, pp. 307–310, May 2009.

[68] S. B. Adler, "Reference Electrode Placement in Thin Solid Electrolytes," *J. Electrochem. Soc.*, vol. 149, no. 5, p. E166, 2002.

[69] S. B. Adler, "Electrode Kinetics of Porous Mixed-Conducting Oxygen Electrodes," *J. Electrochem. Soc.*, vol. 143, no. 11, p. 3554, 1996.

[70] M. E. Lynch, D. S. Mebane, Y. Liu, and M. Liu, "Triple-Phase Boundary and Surface Transport in Mixed Conducting Patterned Electrodes," *J. Electrochem. Soc.*, vol. 155, no. 6, pp. B635–B643, 2008.

[71] E. Koep, C. Jin, M. Haluska, R. Das, R. Narayan, K. Sandhage, R. Snyder, and M. Liu, "Microstructure and electrochemical properties of cathode materials for SOFCs

prepared via pulsed laser deposition," *J. Power Sources*, vol. 161, no. 1, pp. 250–255, 2006.

[72] A. Wedig, M. E. Lynch, R. Merkle, J. Maier, and M. Liu, "Sheet resistance in thin film solid oxide fuel cell model cathodes: A case study on circular Bi 1-xSr xFeO 3-δ microelectrodes," in *ECS Transactions*, 2012, vol. 45, no. 1.

[73] H.-R. Kim, J.-C. Kim, K.-R. Lee, H.-I. Ji, H.-W. Lee, J.-H. Lee, and J.-W. Son, "'Illusional' nano-size effect due to artifacts of in-plane conductivity measurements of ultra-thin films.," *Phys. Chem. Chem. Phys.*, vol. 13, no. 13, pp. 6133–6137, 2011.

[74] B. C. H. Steele, "Interfacial Reactions Associated with Ceramic Ion-Transport Membranes," *Solid State Ionics*, vol. 75, pp. 157–165, 1995.

[75] M. E. Lynch and M. Liu, "Investigation of sheet resistance in thin-film mixed-conducting solid oxide fuel cell cathode test cells," *J. Power Sources*, vol. 195, no. 16, pp. 5155–5166, 2010.

[76] H. Yahiro, Y. Eguchi, K. Eguchi, and H. Arai, "Oxygen ion conductivity of the ceria-samarium oxide system with fluorite structure," *J. Appl. Electrochem.*, vol. 18, no. 4, pp. 527–531, 1988.

[77] N. Yang, Y. Shi, S. Schweiger, E. Strelcov, A. Belianinov, V. Foglietti, P. Orgiani, G. Balestrino, S. V. Kalinin, J. L. M. Rupp, and C. Aruta, "Role of Associated Defects in Oxygen Ion Conduction and Surface Exchange Reaction for Epitaxial Samaria-Doped Ceria Thin Films as Catalytic Coatings," *ACS Appl. Mater. Interfaces*, vol. 8, no. 23, pp. 14613–14621, 2016.

[78] C. Zhang, M. E. Grass, A. H. McDaniel, S. C. DeCaluwe, F. El Gabaly, Z. Liu, K. F. McCarty, R. L. Farrow, M. A. Linne, Z. Hussain, G. S. Jackson, H. Bluhm, and B. W. Eichhorn, "Measuring fundamental properties in operating solid oxide electrochemical cells by using in situ X-ray photoelectron spectroscopy.," *Nat. Mater.*, vol. 9, no. 11, pp. 944–9, Nov. 2010.

[79] T. Suzuki, I. Kosacki, and H. U. Anderson, "Microstructure-electrical conductivity relationships in nanocrystalline ceria thin films," in *Solid State Ionics*, 2002, vol. 151, no. 1–4, pp. 111–121.

[80] W. C. Chueh, Y. Hao, W. Jung, and S. M. Haile, "High electrochemical activity of the oxide phase in model ceria–Pt and ceria–Ni composite anodes," *Nat. Mater.*, vol.

11, no. 2, pp. 155–161, 2011.

[81] Y. Chen, Y. Chen, D. Ding, Y. Ding, Y. Choi, L. Zhang, S. Yoo, D. Chen, B. deGlee, H. Xu, Q. Lu, B. Zhao, G. Vardar, J. Wang, H. Bluhm, E. J. Crumlin, C. Yang, J. Liu, B. Yildiz, and M. Liu, "A robust and active hybrid catalyst for facile oxygen reduction in solid oxide fuel cells," *Energy Environ. Sci.*, vol. 10, no. 4, pp. 964–971, Apr. 2017.

[82] Y. Takasu, T. Sugino, and Y. Matsuda, "Electrical conductivity of praseodymia doped ceria," *J. Appl. Electrochem.*, vol. 14, no. 1, pp. 79–81, 1984.

[83] M. Nauer, C. Ftikos, and B. C. H. Steele, "An evaluation of Ce-Pr oxides and Ce-Pr-Nb oxides mixed conductors for cathodes of solid oxide fuel cells: Structure, thermal expansion and electrical conductivity," *J. Eur. Ceram. Soc.*, vol. 14, no. 6, pp. 493–499, 1994.

[84] P. Shuk, "Hydrothermal synthesis and properties of mixed conductors based on Ce1−xPrxO2−δ solid solutions," *Solid State Ionics*, vol. 116, no. 3–4, pp. 217–223, 1999.

[85] T. Stefanik, "Electrical Properties and Defect Structure of Praseodymium-Cerium Oxide Solid Solutions," Massachusetts Institute of Technology, 2004.

[86] S. R. Bishop, T. S. Stefanik, and H. L. Tuller, "Electrical conductivity and defect equilibria of Pr0.1Ce0.9O(2-δ).," *Phys. Chem. Chem. Phys.*, vol. 13, no. 21, pp. 10165–10173, 2011.

[87] A. Rohatgi, "WebPlotDigitzer." Austin, TX, 2015.

[88] S. R. Jain, K. C. Adiga, and V. R. Pai Verneker, "A new approach to thermochemical calculations of condensed fuel-oxidizer mixtures," *Combust. Flame*, vol. 40, pp. 71–79, Jan. 1981.

[89] P. Burroughs, A. Hamnett, A. F. Orchard, and G. Thornton, "Satellite structure in the X-ray photoelectron spectra of some binary and mixed oxides of lanthanum and cerium," *J. Chem. Soc. Dalt. Trans.*, no. 17, p. 1686, 1976.

[90] M. Romeo, K. Bak, J. El Fallah, F. Le Normand, and L. Hilaire, "XPS Study of the reduction of cerium dioxide," *Surf. Interface Anal.*, vol. 20, no. 6, pp. 508–512, May

1993.

[91] A. Kotani, T. Jo, and J. C. Parlebas, “Many-body effects in core-level spectroscopy of rare-earth compounds,” *Adv. Phys.*, vol. 37, no. 1, pp. 37–85, 1988.

[92] A. Allahgholi, J. I. Flege, S. Thie??, W. Drube, and J. Falta, “Oxidation-state analysis of ceria by x-ray photoelectron spectroscopy,” *ChemPhysChem*, vol. 16, no. 5, pp. 1083–1091, 2015.

[93] F. Zhang, P. Wang, J. Koberstein, S. Khalid, and S. W. Chan, “Cerium oxidation state in ceria nanoparticles studied with X-ray photoelectron spectroscopy and absorption near edge spectroscopy,” *Surf. Sci.*, vol. 563, no. 1–3, pp. 74–82, 2004.

[94] A. Pfau and K. D. Schierbaum, “Electronic structure of stoichiometric and reduced CeO2 surfaces: An XPS, UPS and HREELS study,” *Surf. Sci.*, vol. 321, no. 1–2, pp. 71–80, 1994.

[95] S. C. Decaluwe, M. E. Grass, C. Zhang, F. El Gabaly, H. Bluhm, Z. Liu, G. S. Jackson, A. H. McDaniel, K. F. McCarty, R. L. Farrow, M. A. Linne, Z. Hussain, and B. W. Eichhorn, “In situ characterization of ceria oxidation states in high-temperature electrochemical cells with ambient pressure XPS,” *J. Phys. Chem. C*, vol. 114, no. 46, pp. 19853–19861, 2010.

[96] “Thermo Avantage.” ThermoFischer Scientific, 2016.

[97] E. Bêche, P. Charvin, D. Perarnau, S. Abanades, and G. Flamant, “Ce 3d XPS investigation of cerium oxides and mixed cerium oxide (Ce xTiyOz),” in *Surface and Interface Analysis*, 2008, vol. 40, no. 3–4, pp. 264–267.

[98] H. Borchert, Y. V. Frolova, V. V. Kaichev, I. P. Prosvirin, G. M. Alikina, A. I. Lukashevich, V. I. Zaikovskii, E. M. Moroz, S. N. Trukhan, V. P. Ivanov, E. A. Paukshtis, V. I. Bukhtiyarov, and V. A. Sadykov, “Electronic and chemical properties of nanostructured cerium dioxide doped with praseodymium,” *J. Phys. Chem. B*, vol. 109, no. 12, pp. 5728–5738, 2005.

[99] M. Yu. Sinev, G.W. Graham, L. P. Haack, and M. Shelef, “Kinetic and structural studies of oxygen availability of the mixed oxides Pr1-xMxOy (M = Ce, Zr),” *J. Mater. Res.*, vol. 11, no. 8, pp. 1960–1971, 1996.

[100] H. Ogasawara, A. Kotani, R. Potze, G. A. Sawatzky, and B. T. Thole, “Praseodymium 3d-Core and 4d-Core Photoemission Spectra of Pr2o3,” *Phys. Rev. B*, vol. 44, no. 11, pp. 5465–5469, 1991.

[101] H. L. Tuller, S. R. Bishop, D. Chen, Y. Kuru, J. J. Kim, and T. S. Stefanik, “Praseodymium doped ceria: Model mixed ionic electronic conductor with coupled electrical, optical, mechanical and chemical properties,” in *Solid State Ionics*, 2012, vol. 225, pp. 194–197.

[102] C. Chatzichristodoulou and P. V Hendriksen, “Oxygen Nonstoichiometry and Defect Chemistry Modeling of Ce0.8Pr0.2O2-delta,” *J. Electrochem. Soc.*, vol. 157, no. 4, pp. B481–B489, 2010.

[103] K. Ahn, D. S. Yoo, D. H. Prasad, H.-W. Lee, Y.-C. Chung, and J.-H. Lee, “Role of Multivalent Pr in the Formation and Migration of Oxygen Vacancy in Pr-Doped Ceria: Experimental and First-Principles Investigations,” *Chem. Mater.*, vol. 24, no. 21, pp. 4261–4267, Nov. 2012.

[104] S. Oyama, *The Chemistry of Transition Metal Carbides and Nitrides*. 1996.

[105] S. Ted Oyama, “Crystal structure and chemical reactivity of transition metal carbides and nitrides,” *J. Solid State Chem.*, vol. 96, no. 2, pp. 442–445, Feb. 1992.

[106] S. T. Oyama, “Preparation and catalytic properties of transition metal carbides and nitrides,” *Catal. Today*, vol. 15, no. 2, pp. 179–200, Jun. 1992.

[107] R. B. Levy and M. Boudart, “Platinum-like behavior of tungsten carbide in surface catalysis.,” *Science*, vol. 181, no. 4099, pp. 547–549, 1973.

[108] H. H. Hwu and J. G. Chen, “Surface Chemistry of Transition Metal Carbides,” *Chem. Rev.*, vol. 105, no. 1, pp. 185–212, Jan. 2005.

[109] P. Liu and J. A. Rodriguez, “Water-gas-shift reaction on molybdenum carbide surfaces: essential role of the oxycarbide.,” *J. Phys. Chem. B*, vol. 110, no. 39, pp. 19418–25, Oct. 2006.

[110] M. M. Sullivan, J. T. Held, and A. Bhan, “Structure and site evolution of molybdenum carbide catalysts upon exposure to oxygen,” *J. Catal.*, vol. 326, pp. 82–91, Jun. 2015.

[111] J. Im, H. Shin, H. Jang, H. Kim, and M. Choi, “Maximizing the catalytic function of hydrogen spillover in platinum-encapsulated aluminosilicates with controlled nanostructures.,” *Nat. Commun.*, vol. 5, p. 3370, Jan. 2014.

[112] R. Michalsky, Y.-J. Zhang, A. J. Medford, and A. A. Peterson, “Departures from the Adsorption Energy Scaling Relations for Metal Carbide Catalysts,” *J. Phys. Chem. C*, vol. 118, no. 24, pp. 13026–13034, Jun. 2014.

[113] P. Mars and D. W. van Krevelen, “Oxidations carried out by means of vanadium oxide catalysts,” *Chem. Eng. Sci.*, vol. 3, pp. 41–59, Jan. 1954.

[114] C. Doornkamp and V. Ponec, “The universal character of the Mars and Van Krevelen mechanism,” *J. Mol. Catal. A Chem.*, vol. 162, no. 1–2, pp. 19–32, Nov. 2000.

[115] E. J. Grootendorst, Y. Verbeek, and V. Ponec, “The Role of the Mars and Van Krevelen Mechanism in the Selective Oxidation of Nitrosobenzene and the Deoxygenation of Nitrobenzene on Oxidic Catalysts,” *J. Catal.*, vol. 157, no. 2, pp. 706–712, Dec. 1995.

[116] A. Maltha, “Manganese Oxides as Catalysts for the Selective Reduction of Nitrobenzene to Nitrosobenzene,” *J. Catal.*, vol. 149, no. 2, pp. 364–374, Oct. 1994.

[117] O. Marin-Flores, T. Turba, C. Ellefson, K. Wang, J. Breit, J. Ahn, M. G. Norton, and S. Ha, “Nanoparticle molybdenum dioxide: A highly active catalyst for partial oxidation of aviation fuels,” *Appl. Catal. B Environ.*, vol. 98, no. 3–4, pp. 186–192, Aug. 2010.

[118] Z. Wang, H. Huang, H. Liu, and X. Zhou, “Self-sustained electrochemical promotion catalysts for partial oxidation reforming of heavy hydrocarbons,” *Int. J. Hydrogen Energy*, vol. 37, no. 23, pp. 17928–17935, Dec. 2012.

[119] T. G. Kelly and J. G. Chen, “Metal overlayer on metal carbide substrate: unique bimetallic properties for catalysis and electrocatalysis.,” *Chem. Soc. Rev.*, vol. 41, no. 24, pp. 8021–34, Dec. 2012.

[120] J. A. Rodriguez, P. J. Ramírez, G. G. Asara, F. Viñes, J. Evans, P. Liu, J. M. Ricart, and F. Illas, “Charge polarization at a Au-TiC interface and the generation of highly active and selective catalysts for the low-temperature water-gas shift reaction.,” *Angew. Chem. Int. Ed. Engl.*, vol. 53, no. 42, pp. 11270–4, Oct. 2014.

[121] T. G. Kelly and J. G. Chen, “Controlling C–O, C–C and C–H bond scission for deoxygenation, reforming, and dehydrogenation of ethanol using metal-modified molybdenum carbide surfaces,” *Green Chem.*, vol. 16, no. 2, pp. 777–784, Jan. 2014.

[122] C. Wan, Y. N. Regmi, and B. M. Leonard, “Multiple Phases of Molybdenum Carbide as Electrocatalysts for the Hydrogen Evolution Reaction,” *Angew. Chemie*, vol. 126, no. 25, pp. 6525–6528, Jun. 2014.

[123] H. Vrubel and X. Hu, “Molybdenum Boride and Carbide Catalyze Hydrogen Evolution in both Acidic and Basic Solutions,” *Angew. Chemie Int. Ed.*, vol. 51, no. 51, pp. 12703–12706, Dec. 2012.

[124] Katsuhiko Oshikawa, * and Masatoshi Nagai, and S. Omi, “Characterization of Molybdenum Carbides for Methane Reforming by TPR, XRD, and XPS,” 2001.

[125] J. Dang, G. Zhang, L. Wang, K. Chou, and P. C. Pistorius, “Study on Reduction of MoO_2 Powders with CO to Produce Mo_2C,” *J. Am. Ceram. Soc.*, vol. 99, no. 3, pp. 819–824, Mar. 2016.

[126] C. T. Herbschleb, “ReactorSTM Imaging Catalysts under Realistic Conditions,” 2011.